NASA CONTRACTOR REPORT

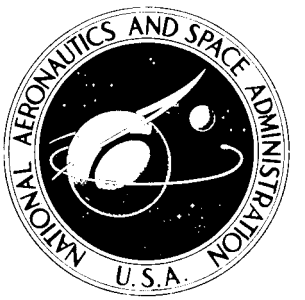

NASA CR-1789

NASA CR-1789

A STUDY TO DETERMINE THE FLIGHT CHARACTERISTICS AND HANDLING QUALITIES OF VARIABLE GEOMETRY SPACECRAFT

Volume II — Medium L/D Concept With Switch-Blade Wings

by B. J. Kuchta and G. R. Friedman

Prepared by
CONVAIR DIVISION OF GENERAL DYNAMICS
San Diego, Calif. 92112
for Langley Research Center

NATIONAL AERONAUTICS AND SPACE ADMINISTRATION • WASHINGTON, D. C. • MARCH 1972

1. Report No.	2. Government Accession No.	3. Recipient's Catalog No.
NASA CR-1890		

4. Title and Subtitle	5. Report Date
A STUDY TO DETERMINE THE FLIGHT CHARACTERISTICS AND HANDLING QUALITIES OF VARIABLE GEOMETRY SPACECRAFT VOLUME III - LOW L/D CONCEPT WITH FOLD-DOWN WINGS	January 1972
	6. Performing Organization Code
7. Author(s)	8. Performing Organization Report No.
G. R. Friedman and B. J. Kuchta	GDC-DDE68-003
	10. Work Unit No.
9. Performing Organization Name and Address	124-07-24-05
General Dynamics Corporation	11. Contract or Grant No.
Convair Division	NAS1-7971
San Diego, CA 92112	13. Type of Report and Period Covered
12. Sponsoring Agency Name and Address	Contractor Report
National Aeronautics and Space Administration	14. Sponsoring Agency Code
Washington, DC 20546	

15. Supplementary Notes

16. Abstract

A study was conducted to determine the flight characteristics and wing deployment transients for a variable geometry spacecraft concept having a hypersonic lift-to-drag ratio near 1.0, and employing fold-down wings for deployment at transonic speeds. Unpowered flight conditions were considered throughout the study. The body of the spacecraft uses a modified trapezoidal cross section. The variable geometry wings, stowed in the sides of the vehicle, are deployed at transonic speeds.

17. Key Words (Suggested by Author(s))	18. Distribution Statement
Variable Dihedral Wings Logistics Lifting Entry Vehicle Dynamics of Wing Deployment Handling Qualities	Unclassified – Unlimited

19. Security Classif. (of this report)	20. Security Classif. (of this page)	21. No. of Pages	22. Price*
Unclassified	Unclassified	89	$3.00

*For sale by the National Technical Information Service, Springfield, Virginia 22151

TABLE OF CONTENTS

LIST OF FIGURES

LIST OF FIGURES, Contd

LIST OF FIGURES, Contd

LIST OF SYMBOLS

b	Aerodynamic reference span, ft
C_D	Drag coefficient
C_L	Lift coefficient
C_{L_β}	Lateral stability parameter
C_M	Pitching moment coefficient
C_{N_β}	Directional stability parameter
C_{Y_β}	Side force parameter
c	Wing chord, ft
c.g.	Center of gravity percent of actual body length
g	Gravity, 32.2 ft/sec^2
h	Vertical tail roll moment arm, ft
H	Altitude, ft
I_{xx}	Moment of inertia about X body axis, slug-ft^2
I_{xz}	Cross product of inertia, slug-ft^2
I_{yy}	Moment of inertia about Y body axis, slug-ft^2
I_{zz}	Moment of inertia about Z body axis, slug-ft^2
K	Constant
L	Rolling moment, ft-lb
ℓ	Aerodynamic reference length, ft
ℓ_t	Horizontal tail pitch moment arm, ft

ℓ_v	Vertical tail yaw moment arm, ft
M	Pitching moment, ft-lb
m	Mass, slug
N	Yawing moment, ft-lb
n_z	Normal load factor, g
P, p	Rolling rate, rad/sec
P_s	Stability axis roll rate, rad/sec
$\bar{Q}$	Free stream dynamic pressure, psf
Q, q	Pitching rate, rad/sec
R, r	Yawing rate, rad/sec
R_s	Stability axis yaw rate, rad/sec
S	Aerodynamic reference area, ft^2
t	Time, sec
U_B	Body velocity along body X axis
V	Free stream velocity, ft/sec
V_B	Body velocity along body Y axis
W_B	Body velocity along body Z axis
X	Longitudinal distance along body, downrange, ft
X_s	Acceleration along the X stability axis, ft/sec^2
Y	Spanwise, ft

Y_s	Acceleration along the Y stability axis, ft/sec^2
Z_s	Acceleration along the Z stability axis, ft/sec^2
α	Angle of attack, deg
β	Angle of sideslip, deg
Γ	Wing dihedral angle, deg
Γ_{int}	Wing dihedral angle for completion of interconnect operation
γ	Flight path angle, deg
ϵ	Downwash at the horizontal tail due to the wing, deg
δ_a	Aileron deflection, deg
δ_e	Elevator or elevon deflection, deg
δ_r	Rudder deflection, deg
ζ	Relative damping factor
ρ	Air density, slug/ft^3
σ	Ratio of density to that at sea level (ρ_0)
ϕ	Euler roll angle, deg
ψ	Euler yaw angle, deg
θ	Euler pitch angle, deg
$\lvert\phi/\beta\rvert$	Ratio of the Dutch roll components in roll and sideslip angle
$\lvert\phi/V_e\rvert$	Ratio of the Dutch roll components in roll and equivalent sideslip angle

Σ	Summation
$\partial()/\partial()$	Partial derivative
$\dot{()}$	$\frac{d()}{dt}$

Subscripts

w	Component due to wing
x	Longitudinal distance
z	Vertical distance
0	Conditions at zero angle of attack
P	Pilot
V	Component due to vertical stabilizer
H	Component due to horizontal stabilizer

SUMMARY

A study was conducted to determine the flight characteristics and wing deployment transients of a variable geometry spacecraft concept having a hypersonic lift-to-drag ratio near 1.0, and employing fold-down wings for deployment at transonic speeds. Unpowered flight conditions were considered throughout the study. The body of the spacecraft uses a modified trapezoidal cross section. The variable geometry wings, stowed in the sides of the vehicle, are deployed at transonic speeds.

Static wind tunnel aerodynamic data were obtained at Mach 0.3 and utilized through out the subsonic speed regime. Damping derivative contributions from the wing, horizontal tail, and vertical tail were determined.

The spacecraft concept studied was dynamically stable throughout the subsonic flight envelope and possesses fairly good handling qualities, although augmentation was needed to meet the desired specifications. The pitch stability augmentation system consisted of a pitch rate feedback. The lateral control system employed a lateral accelerometer to decrease excessive roll due to sideslip, a roll rate feedback to shorten the roll mode time constant, and a yaw rate feedback to improve Dutch roll damping and neutralize the highly stable spiral mode.

A simple dihedral position-elevator interconnect provided the necessary input during wing deployment to keep flight path error to less than 1 degree, dynamic pressure constant to within 2%, and normal acceleration within $\pm$ 0.1g. Elevator needed to trim at the present center of gravity necessitates deployment below 45,000 ft.

The landing flare was initiated at an altitude of 500 ft and at a velocity of 235 knots. After a 0.25g constant load factor pullup (with velocity for a 10-sec float after completion available), the vehicle settled down with a minimum touchdown speed of 133 knots.

A STUDY TO DETERMINE THE FLIGHT CHARACTERISTICS AND HANDLING QUALITIES OF VARIABLE GEOMETRY SPACECRAFT

VOLUME III — LOW L/D CONCEPT WITH FOLD-DOWN WINGS

by G. R. Friedman and B. J. Kuchta

Convair Aerospace Division of General Dynamics
San Diego, California

SECTION 1

INTRODUCTION

Considerable effort is presently being devoted to the development of lifting entry spacecraft concepts for use as possible space logistics systems. Although the vehicle considered in this volume and the other vehicles considered in earlier volumes of this report (References 1 and 2) were sized to be launched by a disposable booster, namely the Saturn I-B, the concepts are inherently capable of being scaled up and used as components of a space shuttle system. In any case, these vehicle concepts permit examination of the same handling quality problems that will be found in the investigation of space shuttle concepts. These problems develop as we consider vehicles that generate significant forces and moments on the body in contrast to conventional airframes where the primary stability characteristics can be derived from the wing and tail geometry.

The purpose of this investigation is to utilize static wind tunnel data to determine overall stability and control, wing deployment, and landing characteristics of a spacecraft concept having a hypersonic lift-drag ratio of approximately 1. The spacecraft incorporates fold-down wings which can be conveniently used on any vehicle with large flat sides. These wings are deployed subsonically to improve subsonic handling characteristics.

The investigation incorporated both analysis and simulation. The analysis provided handling quality parameters and permitted design of a stability augmentation system. Simulation permitted the examination of wing deployment and landing. Lack of transonic and supersonic data limited the investigation to the subsonic portion of the entry trajectory.

The sign convention is presented in Figure 1-1.

SECTION 2

VEHICLE DESCRIPTION

The NASA 1-A vehicle is a blunt-nosed body having a modified trapezoidal cross section (20° side angle), flat bottom, and a slight boattail. The stowed wings are of the variable dihedral type and fold down from the sides at subsonic speeds. The wing section is the Göttingen 711, which has a flat bottom that can fold smoothly into the body side. The horizontal tail is only one wing chord back from the wing and consequently has 80 percent of the area of the wing. Forty-five percent of the horizontal is movable and is used for both pitch and roll control. Directional control is provided by a conventional rudder mounted on a vertical stabilizer. A drawing of the vehicle is contained in Figure 2-1.

The sizing of this spacecraft was considered at Convair under contract NAS 1-7675, Weight and Performance Characteristics of Variable-Geometry Spacecraft (Reference 3). The results of the study indicate the inertial characteristics as follows:

	Wing Deployed	Wing Stowed
Weight, lb	14,160	14,160
c.g., %	59	59
I_{xx}, slug-ft^2	5,200	4,600
I_{yy}, slug-ft^2	30,135	30,230
I_{zz}, slug-ft^2	31,500	31,100

Reference dimensional data for reducing the aerodynamic characteristics to coefficient form are:

Length (ℓ), ft	29.9
Span (b), ft	11.72
Area (S), ft^2	205

SECTION 3

AERODYNAMIC DATA

3.1 STATIC AERODYNAMIC DATA

The NASA 1-A vehicle was examined only at subsonic speeds. Although wind tunnel results were obtained at only Mach 0.3, the data was used up to Mach 0.95 in this report. The inaccuracy of using the data for the full range is recognized, but the results can still be considered typical of a configuration of this type.

The wind tunnel measured data consisted of static aerodynamic coefficients at a center of gravity of 59 percent of the body length for the complete configuration with the wing dihedral set at 0°, 30°, 60°, 90°, and 110° (wing off); body alone data; vertical tail off data; and horizontal tail off data. The data were available at angles of attack from -4° to 21° and at elevator deflections of -20°, -10°, 0°, 10°, and 20°.

The large elevons (necessitated by the short tail moment arm) result in drag coefficients that are highly non-linear with respect to elevon deflection. For this reason it was decided to use tables of lift, drag, and pitch moment coefficients as functions of 10 values of angle of attack, 5 values of elevon deflection, and 5 values of wing dihedral angle. Plots of the lift, drag, and moment coefficients are contained in Figures 3-1 through 3-15.

Trim lift coefficient, drag coefficient, lift-to-drag ratio, and trim elevator were determined as a function of angle of attack for the center of gravity at 59 percent of body length. The curves are plotted as Figures 3-16 through 3-19.

Sideslip derivatives were obtained from wind tunnel data. The data were used directly for analysis as a two-dimensional table at 10 values of angle of attack and 5 values of wing dihedral. The sideslip derivatives are plotted in Figures 3-20, 3-21, and 3-22.

Differential elevon effectiveness was determined from wind tunnel data at two positions of the wing. The effectiveness derivatives were determined by ±10° deflections about a trim deflection of -10° which corresponds to a trimmed angle of attack at maximum L/D. The effectiveness data are plotted in Figures 3-23, 3-24, and 3-25.

Rudder effectiveness was not available. For stability augmentation design, rudder effectiveness derivatives were assumed to be fixed fractions of the vertical sideslip derivative values, i.e.

$$C_{N_{\delta_r}} = K(C_{N_\beta})_V$$

$$C_{L_{\delta_r}} = K(C_{L_\beta})_V$$

$$C_{Y_{\delta_r}} = K(C_{Y_\beta})_V$$

3.2 LONGITUDINAL DYNAMIC DERIVATIVES

The lift and pitch moment contributions of the horizontal tail were determined using tail-off wind tunnel data. The tail contributions at a wing dihedral position of 0° were found by differencing two wind tunnel runs: one in the BWVH* configuration and the other in the BWV configuration. The tail contributions with the wing stowed at 110° of dihedral angle were determined from two runs at -5° of sideslip: one in the BVH configuration and the other in the B configuration. It was assumed that the pitch moment due to drag of the vertical tail, which was missing from the second configuration, would be low. The lift and pitch moment coefficients for the above four configurations are plotted in Figures 3-26 and 3-27. The tail-alone contributions are plotted in Figures 3-28 and 3-29. The following linear approximations to the horizontal tail contributions are made:

For $\Gamma = 0°$

$$(C_L)_H = -0.152 + 0.0163\alpha \qquad (\alpha \text{ in deg})$$

$$(C_M)_H = 0.045 - 0.00552\alpha$$

For $\Gamma = 110°$

$$(C_L)_H = -0.088 + 0.0351\alpha$$

$$(C_M)_H = 0.031 - 0.01320\alpha$$

The change in the slopes with wing dihedral position is due to downwash effects. From the above slopes:

$$(C_{L_\alpha})_H = 0.0351/\text{deg}$$

$$(C_{M_\alpha})_H = -0.01320/\text{deg}$$

---

*B = body, W = wing, V = vertical tail, H = horizontal tail.

$$\left(1 - \frac{\partial \epsilon}{\partial \alpha}\right) (C_{L_\alpha})_H = 0.0163/\text{deg}$$

$$\left(1 - \frac{\partial \epsilon}{\partial \alpha}\right) (C_{M_\alpha})_H = -0.00552/\text{deg}$$

where $\partial\epsilon/\partial\alpha$ is the slope of downwash at the horizontal tail with wing angle of attack.

From the above, an average value of $\partial\epsilon/\partial\alpha$ is 0.56. Using the above horizontal tail slopes, the pitch damping and angle of attack rate derivatives were estimated.

The pitch damping derivatives are determined by assuming that a pitch rate about the center of gravity appears at the horizontal tail as an incremental change in angle of attack as follows:

$$\Delta\alpha = \frac{\ell_t \dot{\theta}}{V}$$

Consequently,

$$C_{L_q} = 2\left(\frac{\ell_t}{\ell}\right)(C_{L_\alpha})_H$$

$$C_{M_q} = 2\left(\frac{\ell_t}{\ell}\right)(C_{M_\alpha})_H$$

For the 1-A vehicle,

$$C_{L_q} = 1.51/(\text{rad/sec})$$

$$C_{M_q} = -0.569/(\text{rad/sec}) \qquad \text{for all } \Gamma$$

The angle of attack rate derivatives are estimated by assuming that the downwash is delayed in getting from the wing to the tail and that this time delay is ℓ_t/V. The difference in downwash is then

$$\Delta\epsilon = -\left(\frac{\ell_t}{c}\right)\frac{\partial \epsilon}{\partial \alpha}\dot{\alpha}$$

Consequently,

$$C_{L_{\dot{\alpha}}} = 2\left(\frac{\ell_t}{c}\right)\frac{\partial \epsilon}{\partial \alpha}\,(C_{L_\alpha})_H$$

$$C_{M_{\dot{\alpha}}} = 2\left(\frac{\ell_t}{c}\right)\frac{\partial \epsilon}{\partial \alpha}\,(C_{M_\alpha})_H$$

Now for the wing stowed configuration downwash is zero, so for the NASA 1-A vehicle

$$C_{L_{\dot{\alpha}}} = 0.881/(\text{rad/sec}) \qquad \Gamma = 0°$$

$$C_{M_{\dot{\alpha}}} = -0.3601/(\text{rad/sec})$$

$$C_{L_{\dot{\alpha}}} = C_{M_{\dot{\alpha}}} = 0 \qquad \Gamma = 90° \text{ and } 110°$$

It was decided to approximate the angle of attack rate derivatives at intermediate wing dihedral positions as follows:

$$(C_{L_{\dot{\alpha}}})_\Gamma = (C_{L_{\dot{\alpha}}})_{\Gamma=0} \cos\Gamma$$

$$(C_{M_{\dot{\alpha}}})_\Gamma = (C_{M_{\dot{\alpha}}})_{\Gamma=0} \cos\Gamma$$

The elevator position does not affect the pitch damping or angle of attack rate derivatives because these derivatives are proportional to angle of attack slopes only and the elevator effectiveness of this vehicle is essentially independent of angle of attack.

3.3 LATERAL DYNAMIC DERIVATIVES

The vertical tail contributions to the sideslip derivatives were determined from the wind tunnel vertical tail-off data. These data are plotted in Figure 3-30. The body-alone derivatives were also calculated, although they were not used for estimating dynamic derivatives. These data are plotted in Figure 3-31. It was recognized that linear approximations of the vertical tail derivative contributions provide sufficient accuracy for estimation of dynamic derivatives, and the following approximations were used.

$$(C_{Y_\beta})_V = -0.0285 + 0.0010\,\alpha \qquad (1/\text{deg})$$

$$(C_{N_\beta})_V = 0.025 - 0.0005\,\alpha \qquad (1/\text{deg})$$

$$(C_{L_\beta})_V = -0.009 - 0.0002\alpha \qquad (1/\text{deg})$$

The vertical tail contributions to the dynamic derivatives were determined by recognizing that for body axes derivatives, the vertical tail sees velocity components different than those at the center of gravity because of yaw and roll rates. This increment in sideslip is:

$$\Delta\beta = \frac{h\,P + \ell_v\,R}{V}$$

where

h is the distance of the vertical tail aerodynamic center above the center of gravity (75 in.)

ℓ_v is the distance of the vertical tail aerodynamic center behind the center of gravity (87 in.)

Because the moment arms for roll and yaw are comparable, large cross coupling derivatives are expected to exist.

The following vertical tail contributions to the dynamic derivatives were determined.

$$(C_{N_R})_V = -1.77 + 0.0354\alpha \qquad \left(\frac{1}{\text{rad/sec}}\right)$$

$$(C_{L_R})_V = 0.638 + 0.0142\alpha \qquad \left(\frac{1}{\text{rad/sec}}\right)$$

$$(C_{Y_R})_V = 2.02 - 0.0709\alpha \qquad \left(\frac{1}{\text{rad/sec}}\right)$$

$$(C_{N_P})_V = 1.53 - 0.0306\alpha \qquad \left(\frac{1}{\text{rad/sec}}\right)$$

$$(C_{L_P})_V = -0.550 - 0.0122\alpha \qquad \left(\frac{1}{\text{rad/sec}}\right)$$

$$(C_{Y_P})_V = -1.74 + 0.0611\alpha \qquad \left(\frac{1}{\text{rad/sec}}\right)$$

Using standard techniques (Reference 4) the wing contributions to dynamic derivatives were determined to be:

$$(C_{N_R})_W = -0.126 - 0.0036\alpha \qquad \left(\frac{1}{\text{rad/sec}}\right) \qquad \Gamma = 0°$$

$$-0.10 - 0.0036\alpha \qquad \left(\frac{1}{\text{rad/sec}}\right) \qquad \Gamma = 30°$$

$$-0.10 - 0.0014\alpha \qquad \left(\frac{1}{\text{rad/sec}}\right) \qquad \Gamma = 60°$$

$(C_{N_R})_w$ =	0.	$\left(\frac{1}{\text{rad/sec}}\right)$	$\Gamma = 90°$ and $110°$
$(C_{L_R})_w$ =	$0.245 + 0.0584\alpha$	$\left(\frac{1}{\text{rad/sec}}\right)$	$\Gamma = 0°$
	$0.346 + 0.556\alpha$	$\left(\frac{1}{\text{rad/sec}}\right)$	$\Gamma = 30°$
	$0.394 + 0.0264\alpha$	$\left(\frac{1}{\text{rad/sec}}\right)$	$\Gamma = 60°$
	0.	$\left(\frac{1}{\text{rad/sec}}\right)$	$\Gamma = 90°$ and $100°$
$(C_{N_P})_w$ =	$-0.035 - 0.0083\alpha$	$\left(\frac{1}{\text{rad/sec}}\right)$	$\Gamma = 0°$
	$-0.037 + 0.0079\alpha$	$\left(\frac{1}{\text{rad/sec}}\right)$	$\Gamma = 30°$
	$-0.031 - 0.0037\alpha$	$\left(\frac{1}{\text{rad/sec}}\right)$	$\Gamma = 60°$
	0.	$\left(\frac{1}{\text{rad/sec}}\right)$	$\Gamma = 90°$ and $110°$
$(C_{L_P})_w$ =	-1.370	$\left(\frac{1}{\text{rad/sec}}\right)$	$\Gamma = 0°$
	-0.750	$\left(\frac{1}{\text{rad/sec}}\right)$	$\Gamma = 30°$
	-0.420	$\left(\frac{1}{\text{rad/sec}}\right)$	$\Gamma = 60°$
	0.	$\left(\frac{1}{\text{rad/sec}}\right)$	$\Gamma = 90°$ and $110°$
$(C_{Y_P})_w$ =	$0.094 + 0.0225\alpha$	$\left(\frac{1}{\text{rad/sec}}\right)$	$\Gamma = 0°$
	$-1.267 + 0.0213\alpha$	$\left(\frac{1}{\text{rad/sec}}\right)$	$\Gamma = 30°$
	$-1.188 + 0.0101\alpha$	$\left(\frac{1}{\text{rad/sec}}\right)$	$\Gamma = 60°$
	0.	$\left(\frac{1}{\text{rad/sec}}\right)$	$\Gamma = 90°$ and $110°$

Horizontal tail contributions were considered significant because of the large span and area. Trim elevator position was used when the contribution depended on tail lift rather than tail lift slope.

$(C_{L_R})_h$	$= -0.077 + 0.0007\alpha$	$\left(\frac{1}{\text{rad/sec}}\right)$	$\Gamma = 0°$
	$0.019 + 0.0105\alpha$	$\left(\frac{1}{\text{rad/sec}}\right)$	$\Gamma = 90°$ and $110°$
$(C_{N_P})_h$	$= 0.095 - 0.0006\alpha$	$\left(\frac{1}{\text{rad/sec}}\right)$	$\Gamma = 0°$
	$0.020 - 0.0077\alpha$	$\left(\frac{1}{\text{rad/sec}}\right)$	$\Gamma = 90°$ and $110°$
$(C_{L_P})_h$	$= -0.24$	$\left(\frac{1}{\text{rad/sec}}\right)$	All Γ
$(C_{Y_P})_h$	$= -0.533 + 0.0019\alpha$	$\left(\frac{1}{\text{rad/sec}}\right)$	$\Gamma = 0°$
	$-0.287 + 0.0270\alpha$	$\left(\frac{1}{\text{rad/sec}}\right)$	$\Gamma = 90°$ and $110°$

The wing, horizontal tail, and vertical tail contributions are combined to the total derivatives below:

C_{N_R}	$= -1.90 + 0.0318\alpha$	$\left(\frac{1}{\text{rad/sec}}\right)$	$\Gamma = 0°$
	$-1.87 + 0.0318\alpha$	$\left(\frac{1}{\text{rad/sec}}\right)$	$\Gamma = 30°$
	$-1.87 + 0.0340\alpha$	$\left(\frac{1}{\text{rad/sec}}\right)$	$\Gamma = 60°$
	$-1.77 + 0.0354\alpha$	$\left(\frac{1}{\text{rad/sec}}\right)$	$\Gamma = 90°$ and $100°$
C_{L_R}	$= 0.806 + 0.0733\alpha$	$\left(\frac{1}{\text{rad/sec}}\right)$	$\Gamma = 0°$
	$0.920 + 0.0718\alpha$	$\left(\frac{1}{\text{rad/sec}}\right)$	$\Gamma = 30°$
	$1.003 + 0.0462\alpha$	$\left(\frac{1}{\text{rad/sec}}\right)$	$\Gamma = 60°$
	$0.657 + 0.0247\alpha$	$\left(\frac{1}{\text{rad/sec}}\right)$	$\Gamma = 90°$ and $100°$

C_{Y_R}	=	$2.02 + 0.0709\alpha$	$\left(\frac{1}{\text{rad/sec}}\right)$	All Γ
C_{N_P}	=	$1.59 - 0.0395\alpha$	$\left(\frac{1}{\text{rad/sec}}\right)$	$\Gamma = 0°$
		$1.58 - 0.0400\alpha$	$\left(\frac{1}{\text{rad/sec}}\right)$	$\Gamma = 30°$
		$1.56 - 0.0384\alpha$	$\left(\frac{1}{\text{rad/sec}}\right)$	$\Gamma = 60°$
		$1.55 - 0.0383\alpha$	$\left(\frac{1}{\text{rad/sec}}\right)$	$\Gamma = 90°$ and $110°$
C_{L_P}	=	$-2.160 - 0.0120\alpha$	$\left(\frac{1}{\text{rad/sec}}\right)$	$\Gamma = 0°$
		$-1.540 - 0.0122\alpha$	$\left(\frac{1}{\text{rad/sec}}\right)$	$\Gamma = 30°$
		$-1.21 - 0.0122\alpha$	$\left(\frac{1}{\text{rad/sec}}\right)$	$\Gamma = 60°$
		$-0.79 - 0.0122\alpha$	$\left(\frac{1}{\text{rad/sec}}\right)$	$\Gamma = 90°$ and $110°$
C_{Y_P}	=	$-2.18 + 0.0885\alpha$	$\left(\frac{1}{\text{rad/sec}}\right)$	$\Gamma = 0°$
		$-3.51 + 0.0877\alpha$	$\left(\frac{1}{\text{rad/sec}}\right)$	$\Gamma = 30°$
		$-3.34 + 0.0857\alpha$	$\left(\frac{1}{\text{rad/sec}}\right)$	$\Gamma = 60°$
		$-2.03 + 0.0881\alpha$	$\left(\frac{1}{\text{rad/sec}}\right)$	$\Gamma = 90°$ and $110°$

3.4 AERODYNAMIC FORCE AND MOMENT EQUATIONS

The aerodynamic force and moment terms are combined in the following non-dimensional force and moment equations.

$$C_D = C_D(\alpha, \delta_e) \tag{1}$$

$$C_L = C_L(\alpha, \delta_e) + C_{L_q}\left(\frac{\ell}{2V}\right) q + C_{L_{\dot{\alpha}}}\left(\frac{\ell}{2V}\right) \dot{\alpha} \tag{2}$$

$$C_M = C_M(\alpha, \delta_e) + C_{M_q}\left(\frac{\ell}{2V}\right) q + C_{M_{\dot{\alpha}}}\left(\frac{\ell}{2V}\right) \dot{\alpha} \tag{3}$$

$$C_Y = C_{Y_\beta}\beta + C_{Y_r}\left(\frac{b}{2V}\right) R + C_{Y_P}\left(\frac{b}{2V}\right) P + C_{Y_{\delta_r}}\delta_r + C_{Y_{\delta_a}}\delta_a \tag{4}$$

$$C_N = C_{N_\beta}\beta + C_{N_R}\left(\frac{b}{2V}\right) R + C_{N_P}\left(\frac{b}{2V}\right) P + C_{N_{\delta_r}}\delta_r + C_{N_{\delta_a}}\delta_a \tag{5}$$

$$C_\ell = C_{L_\beta}\beta + C_{L_R}\left(\frac{b}{2V}\right) R + C_{L_P}\left(\frac{b}{2V}\right) P + C_{L_{\delta_r}}\delta_r + C_{N_{\delta_a}}\delta_a \tag{6}$$

SECTION 4

SIMULATION

4.1 EQUATIONS OF MOTION

The following equations represent six-degree-of-freedom equations of motion about a system of body-oriented axes. The aerodynamic coefficients used in the equations are described in Section 3 of this report. The force equations are wind-axis oriented and the moment equations are body-axis oriented.

The velocity equation is

$$\dot{V} = X_s \cos \beta + Y_s \sin \beta \tag{7}$$

The angle of attack equation is

$$\dot{\alpha} = Q + \frac{\left(\frac{Z_S}{V} - P_s \sin \beta\right)}{\cos \beta} \tag{8}$$

where

$$P_s = P \cos \alpha + R \sin \alpha \tag{9}$$

The sideslip angle equation is

$$\dot{\beta} = \frac{(Y_s \cos \beta - X_s \sin \beta)}{V} - R_s \tag{10}$$

where

$$R_s = R \cos \alpha - P \sin \alpha \tag{11}$$

The force equations are

$$X_s = g_{x_B} \cos \alpha + g_{z_B} \sin \alpha - C_D \bar{Q} \left(\frac{S}{m}\right) \tag{12}$$

$$Y_s = g_{y_B} + C_Y \bar{Q} \frac{S}{m} \tag{13}$$

$$Z_s = g_{z_B} \cos \alpha - g_{x_B} \sin \alpha - C_L \bar{Q} \left(\frac{S}{m}\right) \tag{14}$$

The expansions for C_D, C_L, and C_Y are contained in Equations 1, 2, and 4.

The body gravity components are

$$g_{x_B} = -g \sin \theta \tag{15}$$

$$g_{y_B} = g \cos \theta \sin \phi \tag{16}$$

$$g_{z_B} = g \cos \theta \cos \phi \tag{17}$$

Altitude and ground track computations are made by resolving the total velocity V into body-axis components by the equations

$$U_B = V \cos \alpha \cos \beta \tag{18}$$

$$W_B = V \cos \beta \sin \alpha \tag{19}$$

$$V_B = V \sin \beta \tag{20}$$

Then the body-axis velocities are resolved to the inertial axes by the Euler angles as

$$\dot{H} = U_B \sin \theta - V_B \sin \phi \cos \theta - W_B \cos \phi \cos \theta \tag{21}$$

$$\dot{X} = U_B \cos \theta \cos \psi + V_B (\sin \phi \sin \theta \cos \psi - \cos \phi \sin \psi) + W_B (\cos \phi \sin \theta \cos \psi + \sin \phi \sin \psi) \tag{22}$$

$$\dot{Y} = U_B \cos \theta \sin \psi + V_B (\sin \phi \sin \theta \sin \psi + \cos \phi \cos \psi) + W_B (\cos \phi \sin \theta \sin \psi - \sin \phi \cos \psi) \tag{23}$$

The dynamic pressure equation is

$$\bar{Q} = \frac{1}{2} \rho V^2 \tag{24}$$

where the density (ρ) is determined by the formula of the ARDC 1962 standard atmosphere.

The rotational equations of motion are written in the body axis system.

The pitch equation is

$$\dot{Q} = \frac{\Sigma M}{I_{yy}} + \frac{I_{xz}}{I_{yy}} (R^2 - P^2) - \frac{(I_{zz} - I_{xx})}{I_{yy}} PR \tag{25}$$

The roll equation is

$$\dot{P} = \frac{\Sigma L}{I_{xx}} + \frac{I_{xz}}{I_{xx}} \dot{R} \quad \frac{(I_{zz} - I_{yy})}{I_{xx}} QR + \frac{I_{xz}}{I_{xx}} PQ \tag{26}$$

The yaw equation is

$$\dot{R} = \frac{\Sigma N}{I_{zz}} + \frac{I_{xz}}{I_{zz}} \dot{P} - \frac{(I_{yy} - I_{xx})}{I_{zz}} PQ - \frac{I_{xz}}{I_{zz}} QR \tag{27}$$

The body rates are used to compute the Euler angles by the equations

$$\dot{\theta} = Q \cos\phi - R \sin\phi \tag{28}$$

$$\dot{\phi} = P + \dot{\psi} \sin\theta \tag{29}$$

$$\dot{\psi} = \frac{(R \cos\phi + Q \sin\phi)}{\cos\theta} \tag{30}$$

Control of the spacecraft is accomplished by the deflection of elevons and rudder. Roll control is achieved by differentially deflecting the elevons. The roll controller (ailerons) is computed by

$$\delta_a = (\delta_{e_{left}} - \delta_{e_{right}})/2 \tag{31}$$

The limits placed on the surface deflections are

$$|\delta_e| \leq 20° \tag{32}$$

$$|\delta_a| \leq 10° \tag{33}$$

$$|\delta_r| \leq 25° \tag{34}$$

The moment equations are

$$\Sigma L = C_\ell \bar{Q} S b \tag{35}$$

$$\Sigma M = C_M \bar{Q} S \ell \tag{36}$$

$$\Sigma N = C_N \bar{Q} S b \tag{37}$$

The expansions for C_ℓ, C_M, and C_N are in Equations 3, 5, and 6.

4.2 SIMULATION PROGRAMS

Three digital simulation programs were used extensively in analyzing the NASA 1-A vehicle. They were:

a. Six-Degree-of-Freedom Simulation

b. Steady State Trajectory Program

c. Dynamic Analysis Transfer Function Program

4.2.1 SIX-DEGREE-OF-FREEDOM SIMULATION. This program was used to examine wing deployment and the landing flare, and to obtain dynamic responses to control motion. The stability augmentation systems discussed in Section 4.4 and the automatic landing system discussed in Section 4.3 were simulated. Program output consisted of time responses and rough plots on the line printer.

4.2.2 STEADY STATE TRAJECTORY SIMULATION. This program was used to examine ideal constant load factor landing flares and ideal wing deployment. The short period dynamics were not simulated and the vehicle was assumed to respond instantly in angle of attack, pitch angle, and flight path angle. The program had the capability of flying constant dynamic pressure trajectories or constant flight path angle trajectories. Flight conditions for the dynamic analysis transfer function program were determined by this program.

4.2.3 DYNAMIC ANALYSIS TRANSFER FUNCTION PROGRAM. This program generated transfer functions with and without stability augmentation for inputed flight conditions. It was utilized for determining handling qualities and designing stability augmentation.

SECTION 5

ANALYSIS AND RESULTS

5.1 OVERALL TRAJECTORIES

Because of aerodynamic data limitations, the NASA 1-A vehicle was examined only subsonically. Initial analysis indicated that the vehicle required over 20° of up elevon to trim with wing stowed at Mach 0.95 if the altitude exceeded 45,000 ft. Since this condition corresponded to an angle of attack of 13.6° and L/D was reasonably level (see Figure 3-16) at this point, there was no reason to consider a change in center of gravity or increased elevon deflections to permit trimming at the higher angles of attack corresponding to higher altitudes. For practical purposes, the trajectories considered start at 40,000 ft and lower to leave about 4.5° of elevon authority available for artificial pitch damping and roll control.

Initially, constant flight path trajectories were examined. Figure 5-1 illustrates the results of integrating backwards in time from a landing flare initiation condition of 390 ft/sec (230 knots) at 195 ft. This condition is typical. (A complete discussion is contained in Section 5.4.)

Figure 5-1 illustrates that flight path angles of less than 16° result in an unacceptable rise in dynamic pressure. In any case, Mach 0.95 is reached at altitudes below 15,000 ft. To make best use of our variable geometry wing, we want to deploy the wing subsonically at as high an altitude as possible. A flight path angle of -16°, on the other hand, results in a low dynamic pressure trajectory that remains below Mach 0.5 all the way up to 40,000 ft. The two different results indicate a branch point somewhere between -15° and -16°.* The reason for this anomalous behavior is that we are unable to fly a maximum L/D trajectory. For this vehicle the speed for a maximum L/D approach is 275 ft/sec, while elevon limiting prevents flying below 226 ft/sec. The difference (as shown in Section 5.4) is insufficient for landing flare and float. A possible trajectory could be flown in two constant flight path segments. The terminal segment would be flown at a flight path angle of -16°. The initial segment would be flown shallower with transition from one to the other at about 20,000 ft. An alternate approach is to fly a constant dynamic pressure trajectory from wing deployment at high altitude until the landing site is reachable by a constant flight path segment. This approach is discussed next.

*Branch points often appear in trajectory optimization. The simplest example is that of the great circle route on the earth. From any point on the earth, the shortest distance is the great circle route. As the destination gets further away we suddenly arrive directly opposite the destination and the direction of shortest travel suddenly changes by 180 degrees.

Constant dynamic pressure trajectories can be flown with the result that angle of attack is nearly constant but changes slowly to compensate for flight path angle changes. A guidance scheme can be derived as follows:

$$\bar{Q} = 1/2\, \rho_o\, \sigma\, V^2 \tag{38}$$

$$\dot{\bar{Q}} = \left(\frac{\dot{\sigma}}{\sigma} + 2\,\frac{\dot{V}}{V}\right)\bar{Q} = 0 \tag{39}$$

so

$$\dot{V} = -1/2\left(\frac{\dot{\sigma}}{\sigma}\right) V = -1/2\,\frac{\left(\frac{\partial\sigma}{\partial h}\right)}{\sigma}\,V\dot{h} = -1/2\,\frac{\left(\frac{\partial\sigma}{\partial h}\right)}{\sigma}\,V^2 \sin\gamma \tag{40}$$

but

$$\dot{V} = -C_D \bar{Q}\, S/m - g \sin\gamma \tag{41}$$

so

$$C_D\left(\frac{\bar{Q}S}{m}\right) = \left[\frac{\frac{\partial\sigma}{\partial h}}{\sigma^2}\,\frac{\bar{Q}}{\rho_o} - g\right] \sin\gamma \tag{42}$$

but

$$C_L\, \bar{Q}S = mg\cos\gamma \tag{43}$$

so finally determine angle of attack to satisfy

$$C_L^2 = \left(\frac{mg}{\bar{Q}S}\right)^2 - \left[\frac{C_D}{1 - \frac{\partial\sigma}{\partial h}\,\bar{Q}_o/\rho_o\, g\,\sigma^2}\right]^2 \tag{44}$$

Equation 44 was implemented and the resulting constant dynamic pressure trajectories from Mach 0.95 at 30,000 ft, 35,000 ft, and 40,000 ft are shown in Figure 5-2. This type of trajectory would be flown until a constant flight path could be flown to flare initiation. Note that constant dynamic pressure flight implies a constantly steepening flight path.

The elevation plots for the trajectories are given in Figure 5-3.

5.2 WING DEPLOYMENT

Wing deployment doubles the subsonic lift-to-drag ratio and has a corresponding effect at supersonic speeds. To maximize range it is desirable to deploy the wing at high

altitude and as early as possible. Because of aerodynamic heating and resultant weight penalties associated with thermal protection, the wing would not be deployed above Mach 1.5. Deployment supersonically would require a stronger structure. The wind tunnel data show that early partial deployment is not advantageous. Figure 3-20 indicates that directional stability is severely reduced above an angle of attack of 12° when the wing is deployed to a dihedral angle of 90°. This interference effect is further indicated in the trimmed L/D curve of Figure 3-16 and in the increased trim drag of Figure 3-19.

From the above considerations it was decided to examine deployment at Mach 0.95 and at altitudes from 30,000 ft to 40,000 ft. A practical deployment rate of 10 deg/sec was used.

Figure 5-4 illustrates steady state wing deployment assuming instantaneous pitch response. From these ideal responses the necessary change in elevator deflection can be determined. This change in trim elevator was programmed as being linear with wing deployment for the dynamic responses as follows:

$$(\delta_e)_{\text{interconnect}} = \begin{cases} \Delta\delta_e \dfrac{110° - \Gamma}{110° - \Gamma_{int}} & \text{for } \Gamma > \Gamma_{int} \\ \Delta\delta_e & \text{for } \Gamma \leq \Gamma_{int} \end{cases} \tag{45}$$

Figures 5-5, 5-6, and 5-7 illustrate the three-degree-of-freedom wing deployment responses for 40,000 ft, 35,000 ft, and 30,000 ft, respectively. Each figure illustrates responses to two different interconnect rates. One rate completes the trim elevator change during the first 20° of deployment. The other completes the trim change during the first 60° of deployment. The 60° deployment, based on the ideal response wing deployments of Figure 5-4, works quite well for deployment at 40,000 ft. At lower altitudes a faster interconnect is desirable to maintain dynamic pressure, although the faster interconnects result in larger normal acceleration transients. It should also be mentioned, that closed loop guidance during wing deployment would reduce the transient even further than this open-loop interconnect operation.

On the basis of the wing deployment responses, wing deployment should occur at 40,000 ft. The transient at that condition is well controlled. The normal acceleration transient is less than 0.25g, the pitch rate is less than 1 deg/sec, and the loss in dynamic pressure is about 2.5 percent.

5.3 LANDING CHARACTERISTICS

An unpowered vehicle is constrained to touchdown when it is unable to generate sufficient lift for level flight. The maximum usable lift coefficient is determined by such conditions as:

a. Pre-stall buffet.

b. Full-up elevator.

c. Maximum pitch attitude for landing gear design.

With the 1-A vehicle, the constraint was considered to be trim elevator. Twenty degrees of up elevator results in a maximum trim angle of attack of 18.2°. This resulted in a minimum touchdown speed of 225 ft/sec or 133 knots.

The pilot, of course, cannot count on landing at the minimum touchdown speed. He must provide some speed margin to take into account slight variations in flare, time to deploy landing gear, and time to come out of the flare and settle to the runway. For this study the drag and pitch moment due to the landing gear have been neglected. Since the gear would not be deployed until the flare was almost complete its main effects are a pitch down kick and increased deceleration to touchdown. Figure 5-8 illustrates level flight deceleration to touchdown. From this figure the flare completion speed can be determined for a desired float time or speed margin. For this study, 15 seconds was considered adequate. Analysis was also performed for a 5-sec float. Float times up to 30 sec were also examined, but the 10 ft/sec^2 deceleration makes them prohibitive since a 30-sec float requires a flare completion velocity of 300 knots.

Constant load factor flare trajectories were determined using the trajectory program. Figures 5-9 and 5-10 illustrate flares associated with 5 sec of float time. Figures 5-11 and 5-12 illustrate flares associated with 15 sec of float time. Figures 5-13 and 5-14 plot altitude loss versus normal load factor for various initial flight path angles. Figures 5-15 and 5-16 cross plot altitude and sink rate for various load factors and initial flight path angles. The altitude versus sink rate plots form the basis of the automatic landing system described below.

Existing landing flare computers utilized in transport and commercial aircraft normally program sink rate as an exponential decay. This works fine for transition from a flat 2-1/2° or 3° glide path. For low L/D vehicles such as the 1-A vehicle, a true normal acceleration command was considered appropriate since normal approach would be at 12° to 15° of sink angle. The altitude versus sink rate plots of Figures 5-15 and 5-16 indicate that a constant load factor flare is almost equivalent to a constant rate of change of sink rate flare. Consequently

$$(n_z)_{\text{command}} \ (\text{ft/sec}^2) \approx \ddot{h}_{\text{command}} \tag{46}$$

but

$$2h\ddot{h} = (\dot{h})^2 \qquad \text{from elementary mechanics} \tag{47}$$

A flare computer utilizing the above technique was programmed and the gains optimized for a wide range of initial flare altitudes (and consequently different load factors). The flare computer is diagrammed in Figure 5-17.

For the simulated flares, it was decided to approach on a -12° flight path and execute the flares at the velocities and altitudes specified in Figure 5-12, so as to obtain float time up to 15 sec. This goal is consistent with published data on the X-15 aircraft (Reference 5). The X-15 has a minimum touchdown speed of 250 ft/sec at an angle of attack of 13°. However, most landings are made between 290 ft/sec and 320 ft/sec. This speed range is equivalent, for that airplane, to float time capability remaining of 4 to 7 sec.

Figure 5-18 illustrates a flare started at 300 ft. The average load factor is about 1.4g. Figure 5-19 illustrates a flare started at 500 ft. The average load factor is about 1.25. The short tail arm effect is quite noticeable in Figure 5-18. As the elevator deflects to start pitching the aircraft, the initial response is a large normal acceleration pulse in the wrong direction. This results in excessive overshoot. The effect actually smoothes touchdown since as the airplane stops flaring at 5 ft of altitude the elevator provides a vertical force that decreases sink speed. In any case, the large normal force due to elevon is confusing to the pilot but unavoidable in this vehicle.

5.4 HANDLING QUALITIES AND STABILITY AUGMENTATION SYSTEM

5.4.1 LONGITUDINAL. The NASA 1-A vehicle was examined to determine how well it compared with the requirements of MIL-F-8785B, Military Specification-Flying Qualities of Piloted Airplanes (References 6 and 7). In the process, a stability augmentation system was designed to improve the minor deficiencies. All airplanes are deficient in pitch damping at high altitudes, as is the NASA 1-A vehicle. A simple pitch damper is adequate. The gain is scheduled with dynamic pressure. This system is illustrated in Figure 5-20.

The major longitudinal requirements are on the short period oscillation that results from elevator deflection. It is basically an angle-of-attack response at constant speed. The range of acceptable frequency is determined by bounds on the quantity

$$\frac{\omega_{n_{sp}}^2}{n_z/\alpha} \left[\frac{(\text{rad/sec})^2}{(g/\text{rad})} \right]$$

where $\omega_{n_{sp}}$ is the short period natural frequency and n_z/α is the steady state normal acceleration per radian of angle of attack. When this ratio is too large, there is a tendency towards pilot-induced oscillations. When it is too low, the aircraft is sluggish and it is difficult to control flight path. Figure 5-21 illustrates the short-period frequency with wing deployed and augmentation off. Figure 5-22 illustrates the minor effect of the augmentation.

Figures 5-23 and 5-24 illustrate the change in short period frequency during wing deployment with the augmentation off and on, respectively. Figures 5-25 and 5-26 illustrate the $\omega_{n_{sp}}^2/(n_z/\alpha)$ requirement with wing deployed and augmentation off and on, respectively. Note that the vehicle is comfortably within the limits. Figure 5-27 and 5-28 illustrate the frequency requirement during deployment. Note that the vehicle exceeds the boundary for wing stowed. This is not surprising considering the short tail arm. It should not pose a practical problem since an autopilot would be active down through wing deployment.

Figures 5-29 and 5-30 show how well the 1-A vehicle meets the short-period damping ratio requirement with wing deployed. Figure 5-31 illustrates that the vehicle without augmentation is substandard with wing stowed. This reduction in damping results from loss of the angle of attack rate damping due to downwash delay. Figure 5-32 illustrates that the stability augmentation system maintains adequate damping during wing deployment.

The airplane response to elevator also contains the phugoid mode which is a heaving motion during which potential energy (altitude) is exchanged for kinetic energy (velocity). As illustrated in Figures 5-33 and 5-34, our vehicle is adequately damped. This should be expected since the phugoid damping ratio is inversely proportional to L/D. The phugoid period for this vehicle ranges from about 60 sec to 140 sec.

5.4.2 LATERAL. The lateral handling qualities of the NASA 1-A vehicle were examined and a lateral control system designed to improve the characteristics. Basically, the vehicle exhibited excessive roll due to sideslip and yaw rate due to the short vertical tail moment arm and high location on the body. In addition, since the major component of roll damping is provided by the wing and is proportional to the wing lift slope, the fact that the wing generates only about a third of the total lift results in low roll damping. The large yaw due to roll rate would result in large sideslip during rolling. Figure 5-35 illustrates the lateral stability augmentation system. The lateral accelerometer is fed back to the aileron to decrease roll due to sideslip. The roll damping and yaw damping gains improve the roll time constant and increases the Dutch roll damping. The yaw rate to aileron cross gain minimizes the spiral mode.

Figures 5-36 and 5-37 illustrate roll responses at two flight conditions. Figure 5-38 illustrates the Dutch roll characteristics. Without augmentation, the vehicle almost meets the requirement. The Dutch roll frequency is about double the minimum requirement. This suggests that it might be practical to consider a smaller vertical stabilizer, which would also result in decreased roll due to sideslip. Figure 5-39 illustrates the roll oscillation requirement. The complete roll response transfer function of this vehicle contains a denominator containing the roll mode, spiral mode, and Dutch roll mode. The numerator contains a root that partially cancels the spiral mode and a pair of complex roots that partially cancel the Dutch roll mode. The ratio of the numerator

zero to the Dutch roll frequency is usually a good indication of the amount of oscillation in the roll response. The performance during wing deployment could be improved by rescheduling the stability augmentation system gains. Figure 5-40 compares the 1-A vehicle with the criterion of MIL-F-8775A. The Dutch roll damping parameter gives the cycles to half amplitude. The $|\phi/V_e|$ parameter is the $|\phi/\beta|$ ratio divided by equivalent velocity. Figures 5-41 and 5-42 illustrate the roll mode time constant. The roll mode couples with the spiral mode with the augmentation off, which is considered unacceptable by the military specification. A coupled roll-spiral mode results in a zero steady-state roll rate and a low frequency roll rate oscillation that often exhibits roll reversal. Figures 5-43 and 5-44 present the time for the spiral mode to half amplitude. The excessive stability results in the roll rate washing out to a step aileron command. Generally a time to half amplitude of at least 10 sec is satisfactory, with degraded performance when the time drops below 5 sec. The excessive spiral stability with wing stowed could be corrected by modifying the stability augmentation gains.

As indicated, the vehicle has fairly good lateral characteristics even without augmentation. The subsonic characteristics would probably be improved by a vertical tail of smaller size and lower profile. The elevons are excessively sensitive as indicated by the roll rates in Figures 5-36 and 5-37 resulting from a single degree of differential elevon. It would be well to consider splitting the elevons or employing a separately controlled tab on the elevon for roll control.

SECTION 6

CONCLUSIONS

This study determined the flight characteristics of a variable geometry spacecraft with a hypersonic lift-to-drag ratio of about 1. The fold-down wings provide improved subsonic performance. The results of the analysis are presented in terms of time histories, landing characteristics, and handling quality parameters. The following conclusions are drawn:

a. Wing deployment should occur at Mach 0.95 at 40,000 ft to maximize range while minimizing buffet loads on the wing. Partial deployment does not appear to be advantageous. Deployment transients are not critical and can be controlled by an elevator interconnect and pitch damper.

b. Minimum touchdown speed is 133 knots. The velocity for flying a maximum L/D trajectory is too low for flare initiation; consequently the appropriate trajectory from wing deployment to landing approach is a constant dynamic pressure trajectory transitioning into a -12° flight path angle trajectory. The vehicle can execute a 0.25g flare from 500 ft altitude and a velocity of 400 ft/sec.

c. The longitudinal handling qualities are satisfactory. Augmentation improves pitch damping. The short period frequency is higher than desired with wing stowed, but this is of little consequence since the primary control during this period is by autopilot.

d. The lateral handling qualities are marginal without augmentation due to a coupled roll-spiral mode and excessive roll due to sideslip. With augmentation the vehicle can be made to meet all requirements. A smaller vertical stabilizer with a lower profile might improve unaugmented characteristics by decreasing roll due to sideslip. Differential elevon for roll control is extremely sensitive. Splitting the elevons is suggested to decrease sensitivity.

SECTION 7

REFERENCES

1. B. J. Kuchta, Flight Characteristics and Handling Qualities of Variable Geometry Spacecraft - Vol. 1 High L/D Concept with Single Pivot Two-Position Skewed Wing, GDC-DDE68-003, Convair division of General Dynamics, 1969.

2. B. J. Kuchta and G. R. Friedman, Flight Characteristics and Handling Qualities of Variable Geometry Spacecraft - Vol. 2 Medium L/D Concept with Switch-Blade Wings, GDC-DDE68-003, Convair division of General Dynamics, 1970.

3. K. S. Coward, A Study to Determine the Weight and Performance Characteristics of Variable Geometry Spacecraft, GDC-DCB68-012, Convair division of General Dynamics, 1968.

4. D. E. Hoak, USAF Stability and Control Datcom, Flight Control Division, Air Force Flight Dynamics Laboratory, Wright-Patterson Air Force Base, Ohio, 1965.

5. L. M. Gaines and T. E. Surber, Prediction of Optimum Approach and Landing Techniques for Manned Re-entry Gliders, Paper No. 61-115-1809, National IAS-ARS Joint Meeting, 1961.

6. Flying Qualities of Piloted Airplanes, Military Specification MIL-F-8785B(ASG), 1969.

7. C. R. Chalk, et. al., Background Information and User Guide for MIL-F-8785B(ASG), "Military Specification - Flying Qualities of Piloted Airplanes." AFFDL-TR-69-72, 1969.

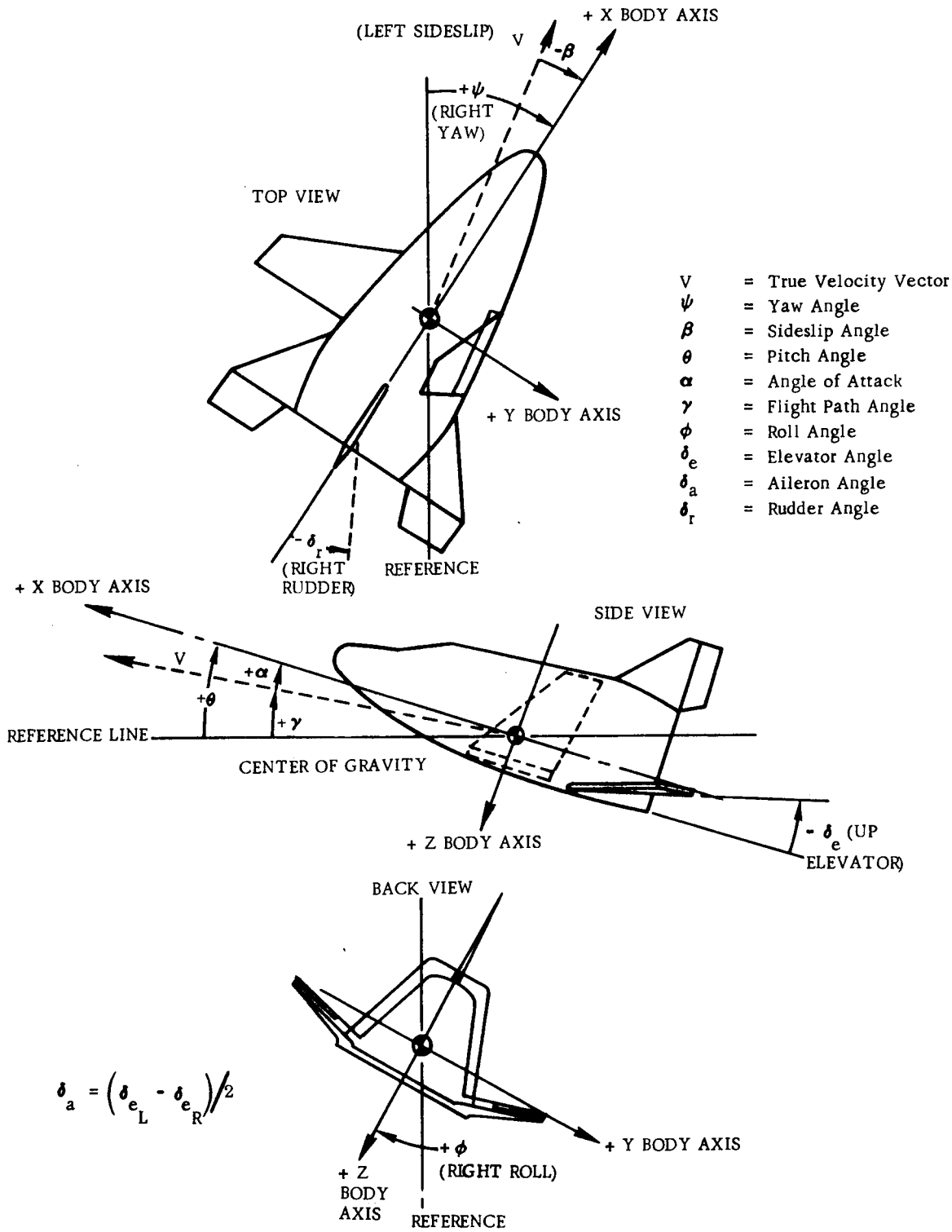

Figure 1-1. Sign Convention

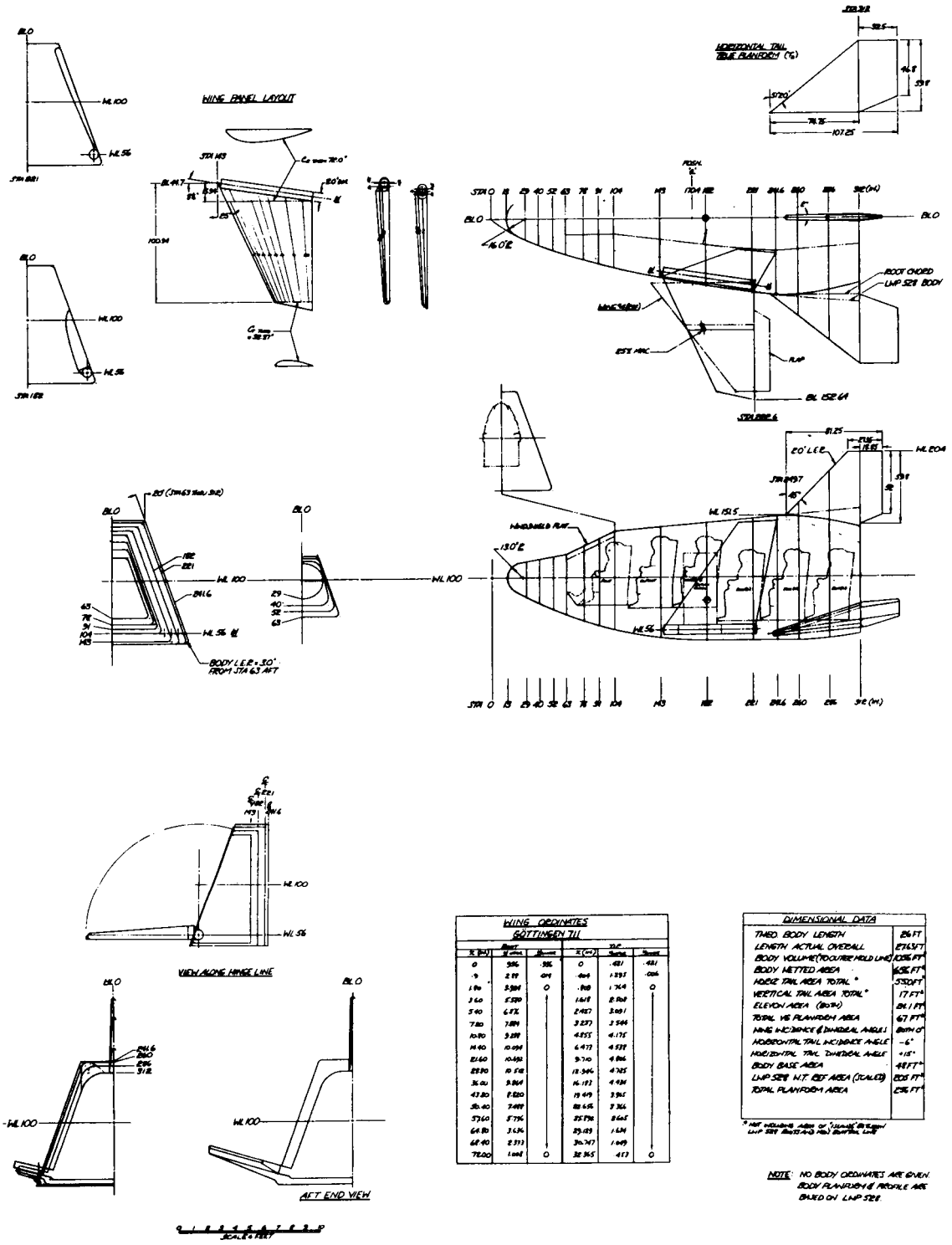

Figure 2-1. Drawing of the Hypersonic L/D ≈1 Vehicle

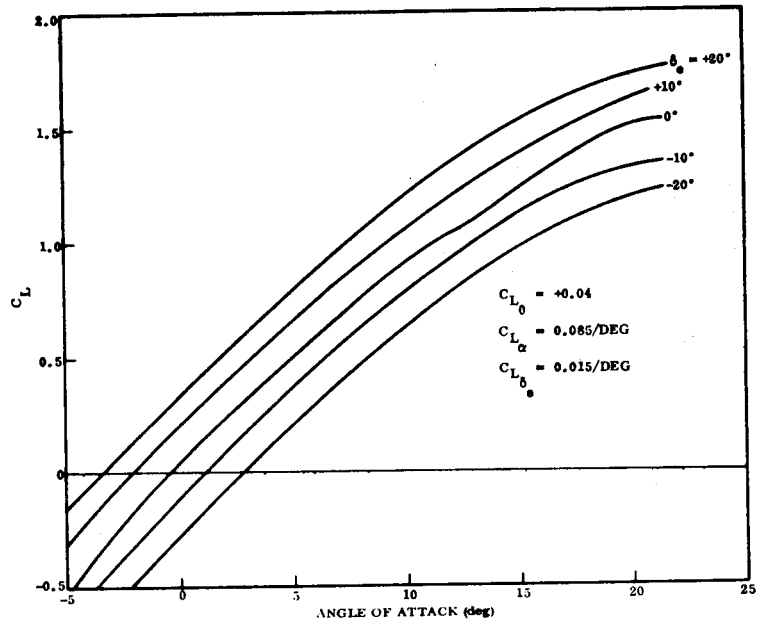

Figure 3-1. Subsonic Lift Coefficient ($\Gamma = 0°$)

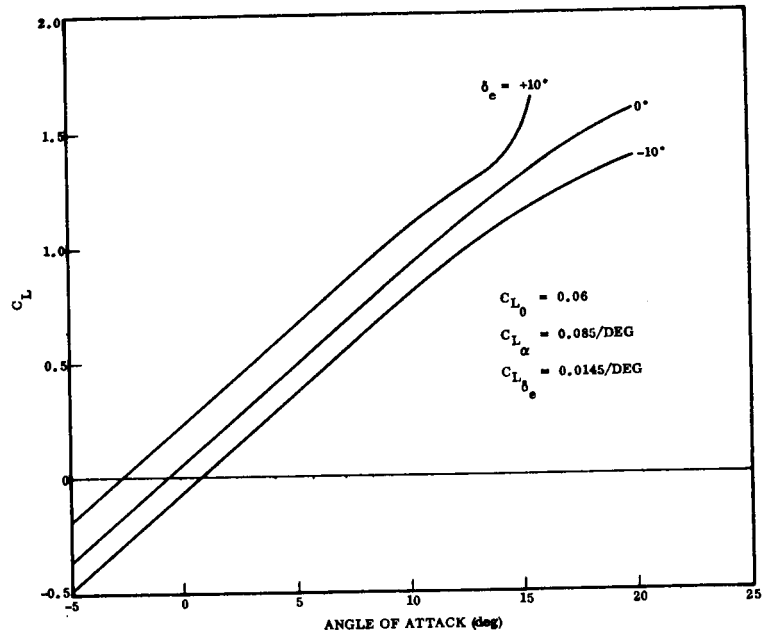

Figure 3-2. Subsonic Lift Coefficient ($\Gamma = 30°$)

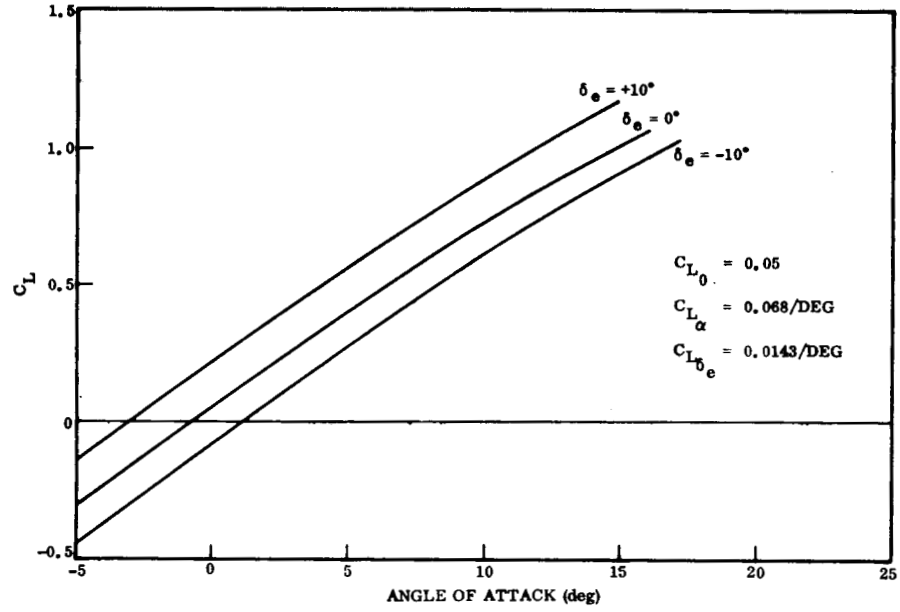

Figure 3-3. Subsonic Lift Coefficient ($\Gamma = 60°$)

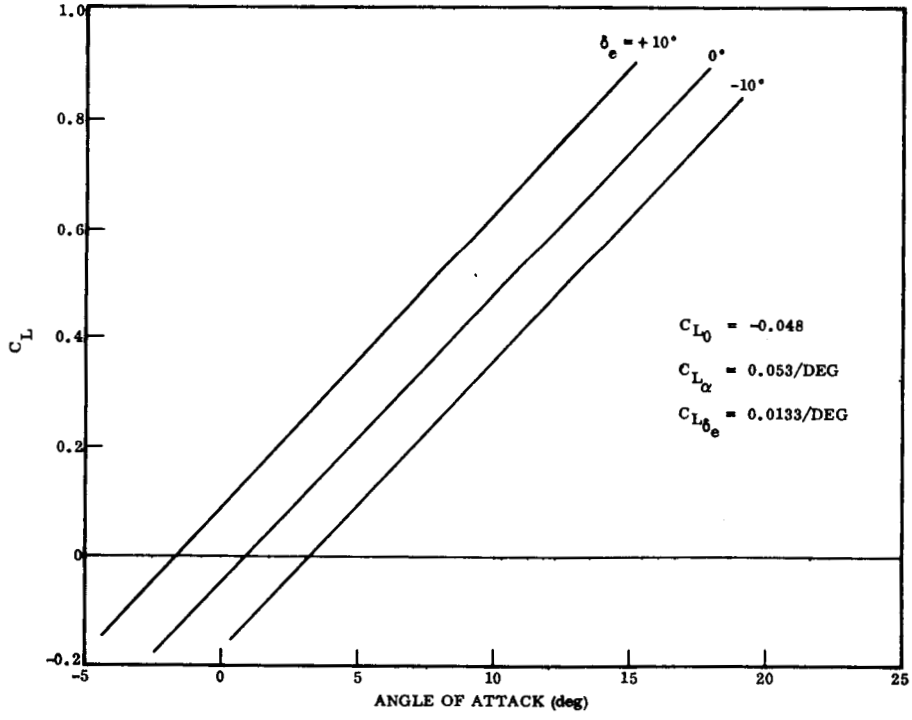

Figure 3-4. Subsonic Lift Coefficient ($\Gamma = 90°$)

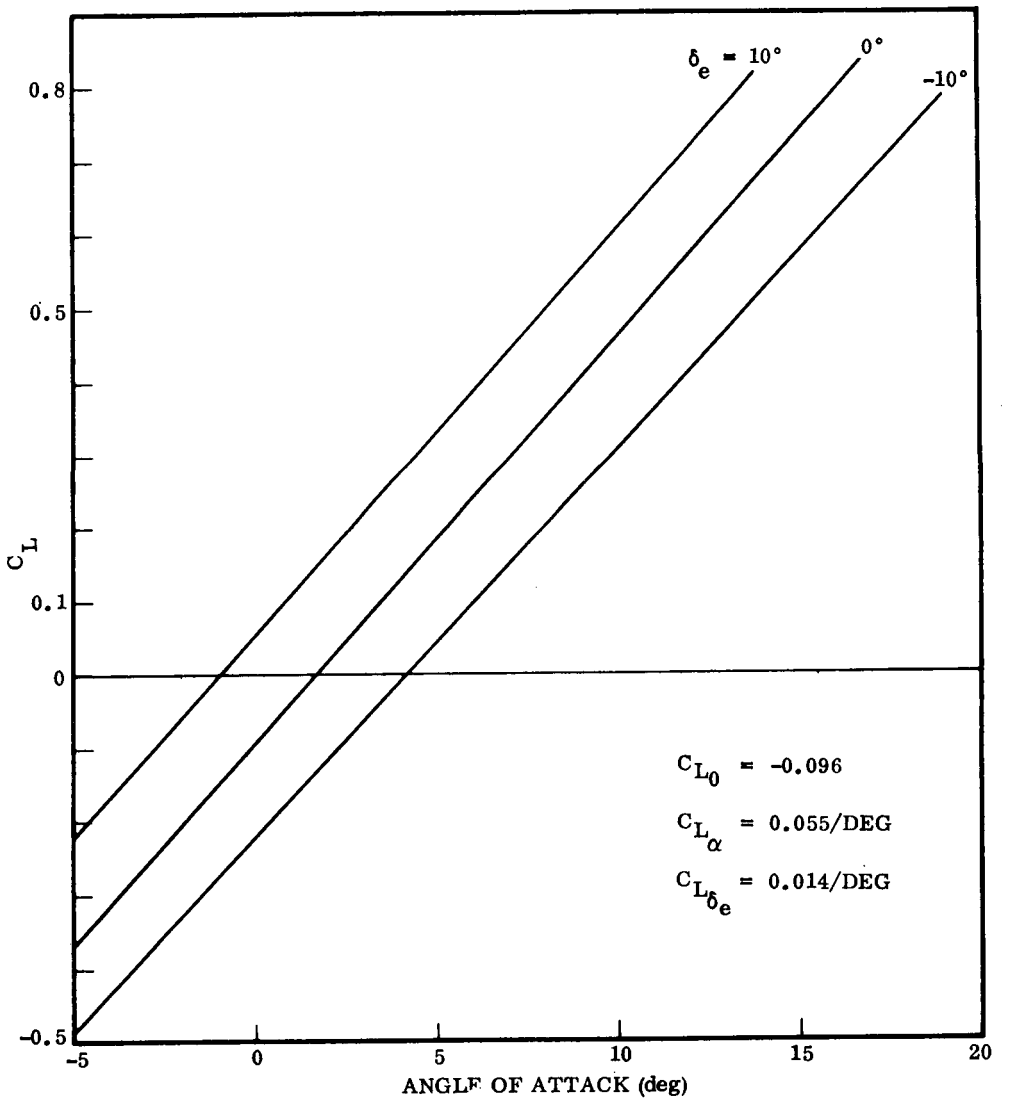

Figure 3-5. Subsonic Lift Coefficient (Γ= 110°)

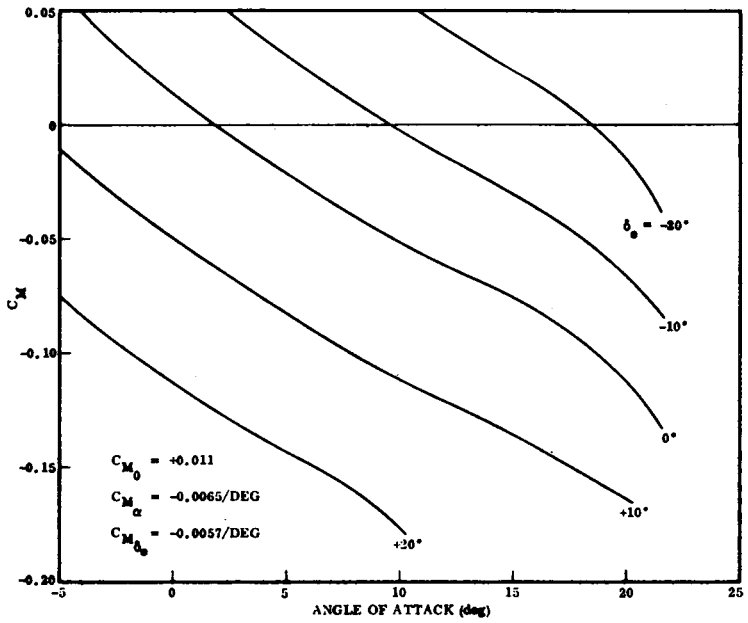

Figure 3-6. Subsonic Pitch Moment Coefficient ($\Gamma = 0°$)

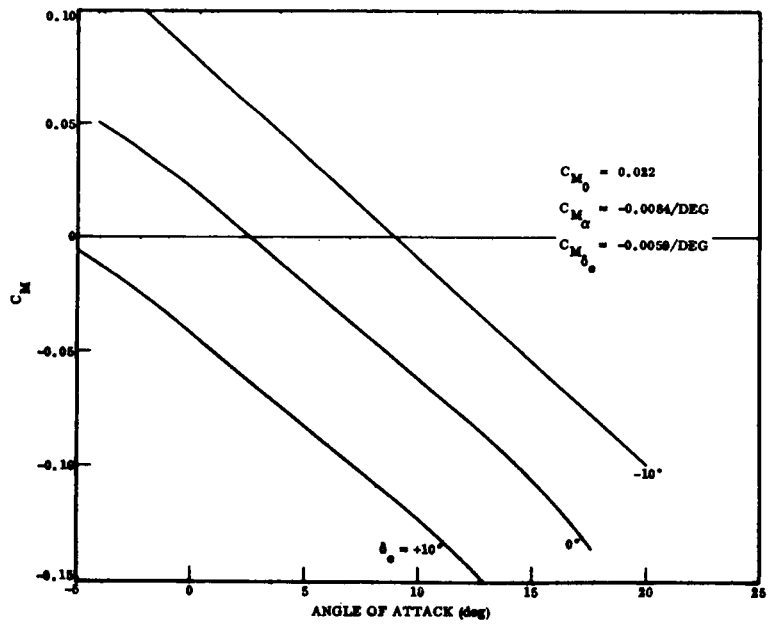

Figure 3-7. Subsonic Pitch Moment Coefficient ($\Gamma = 30°$)

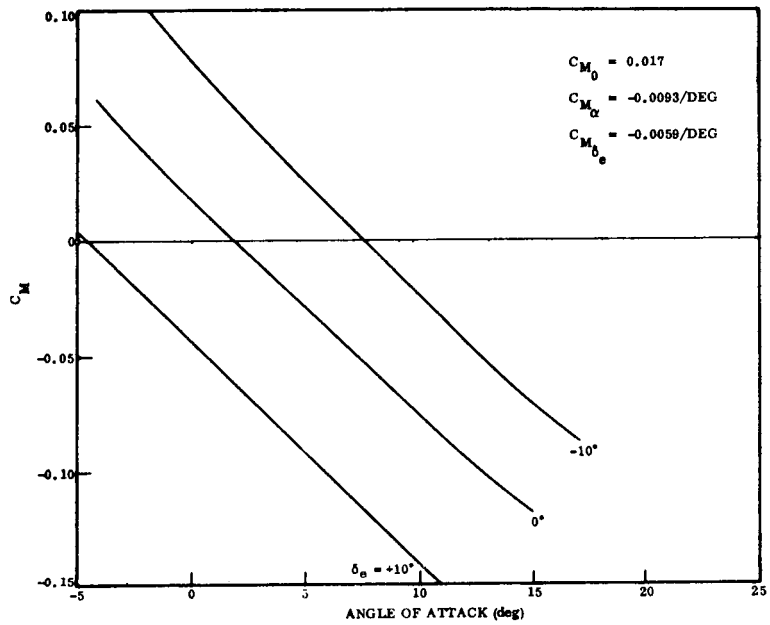

Figure 3-8. Subsonic Pitch Moment Coefficient (Γ= 60°)

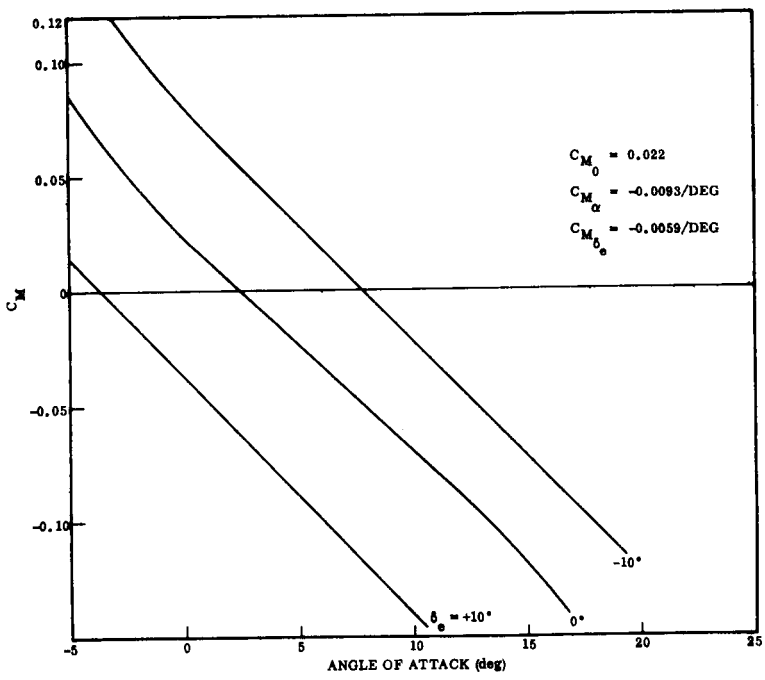

Figure 3-9. Subsonic Pitch Moment Coefficient (Γ= 90°)

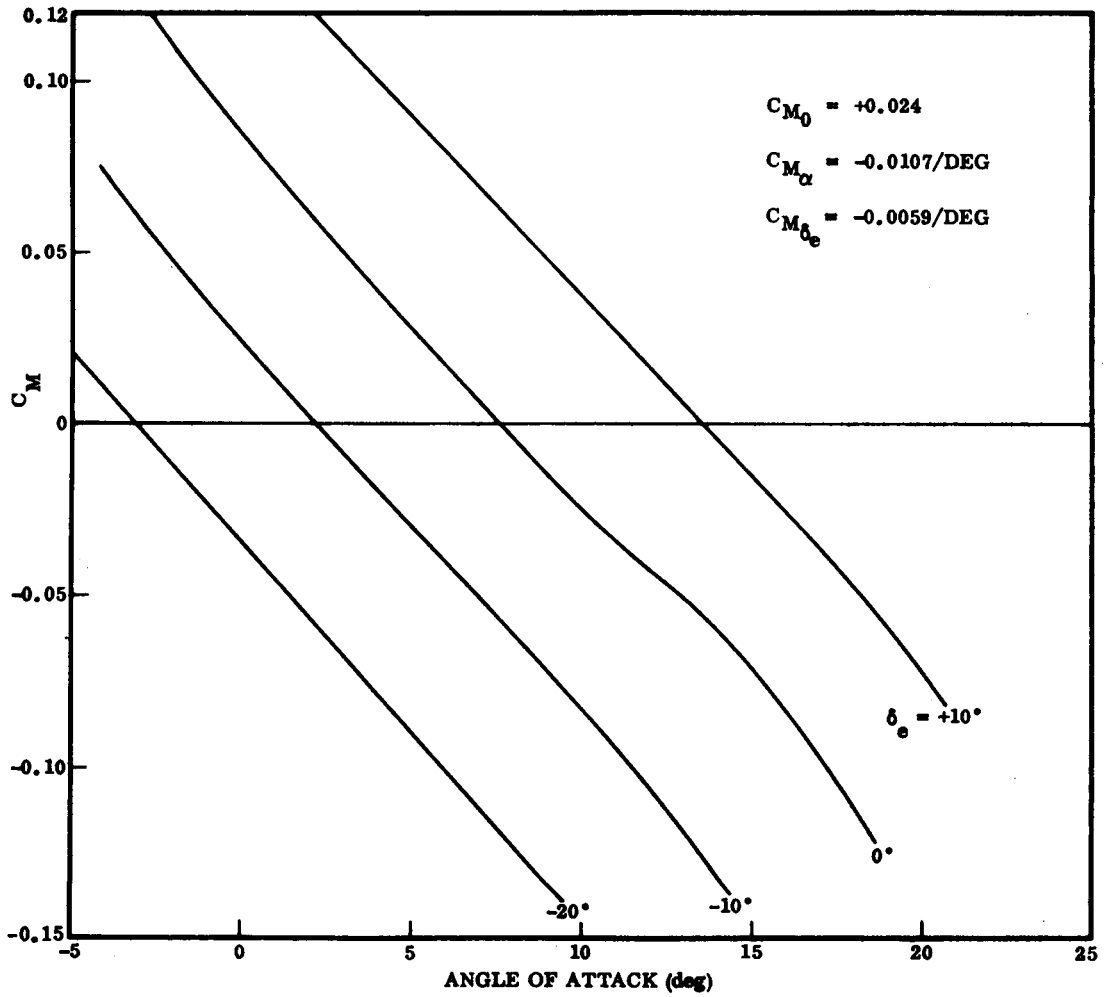

Figure 3-10. Subsonic Pitch Moment Coefficient (Γ = 110°)

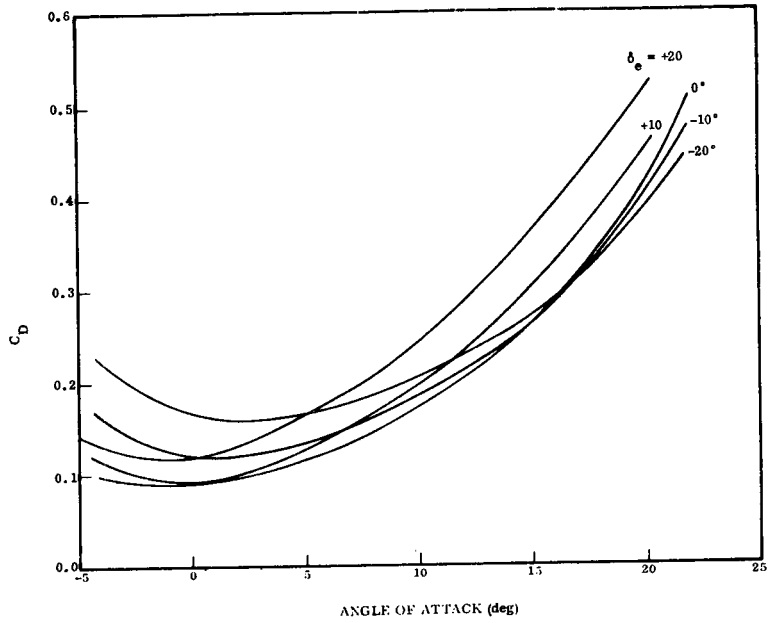

Figure 3-11. Subsonic Drag Coefficient ($\Gamma = 0°$)

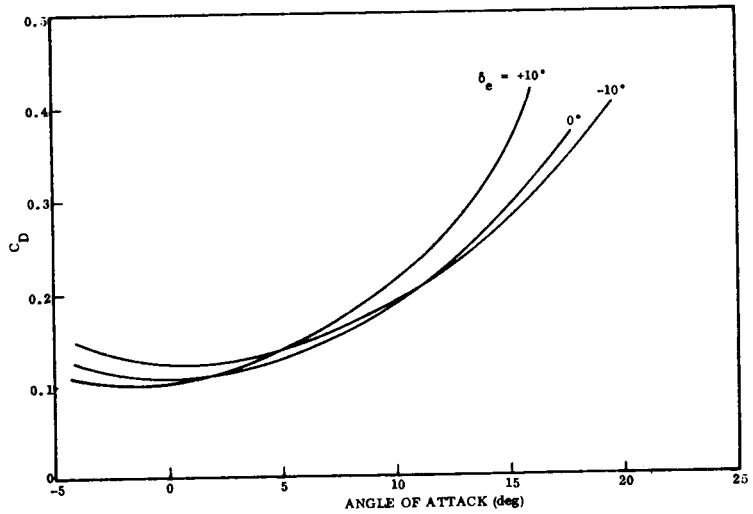

Figure 3-12. Subsonic Drag Coefficient ($\Gamma = 30°$)

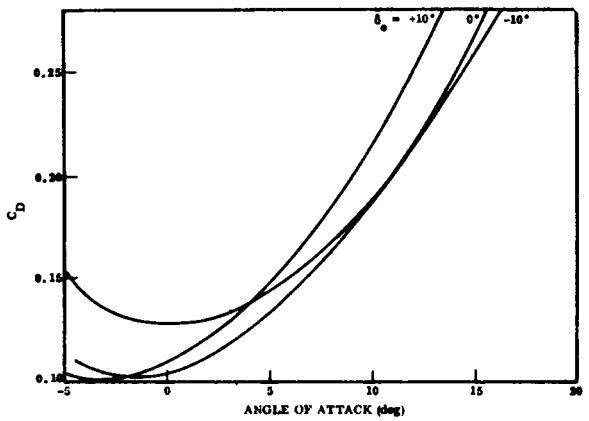

Figure 3-13. Subsonic Drag Coefficient (Γ= 60°)

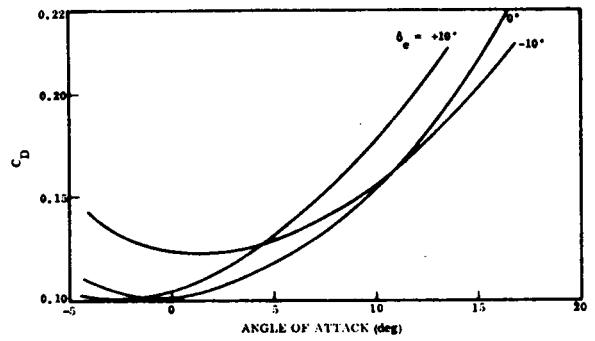

Figure 3-14. Subsonic Drag Coefficient (Γ= 90°)

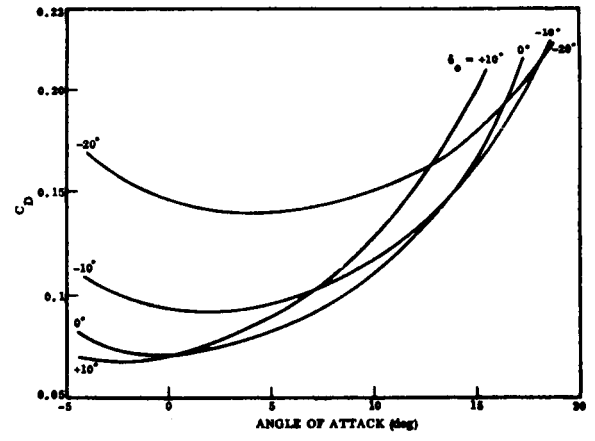

Figure 3-15. Subsonic Drag Coefficient (Γ= 110°)

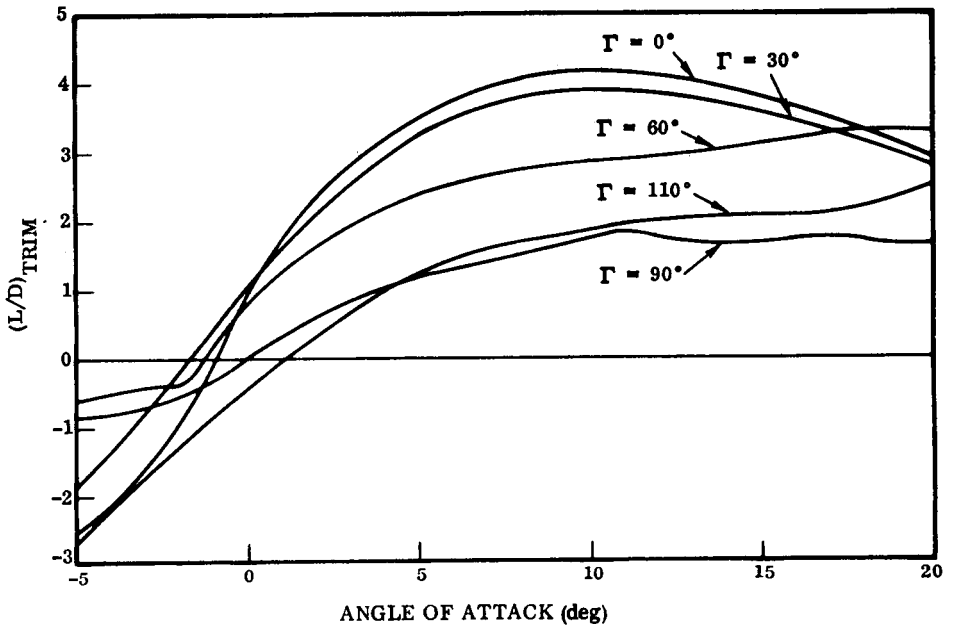

Figure 3-16. Subsonic Trim L/D

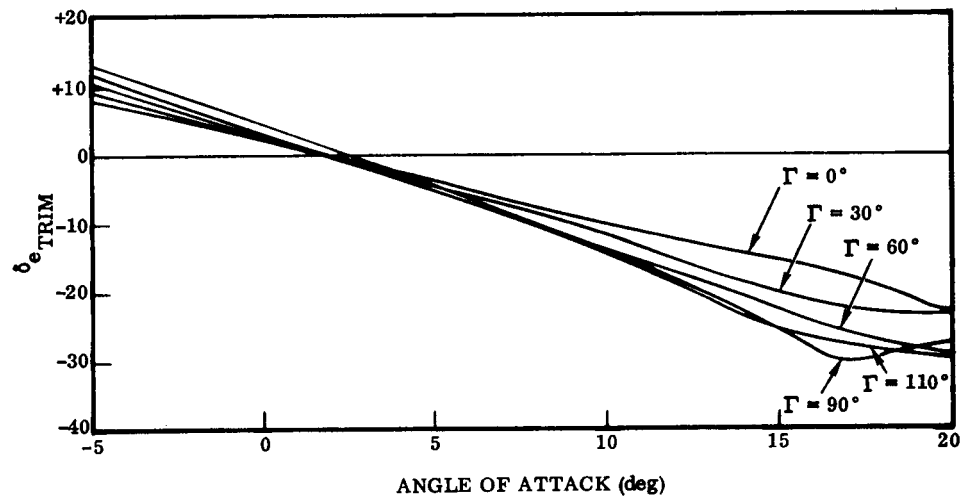

Figure 3-17. Trim Elevator

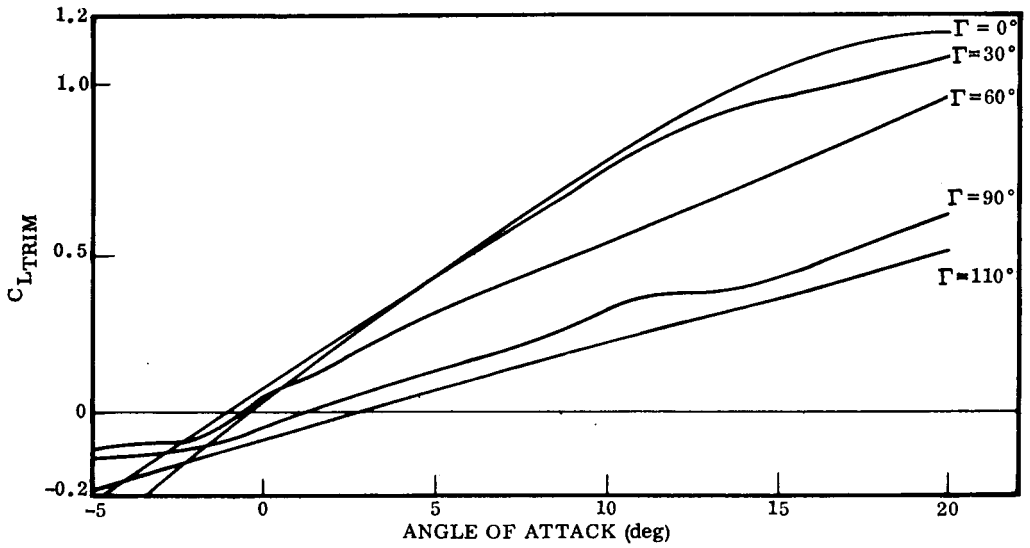

Figure 3-18. Trim Lift Coefficient

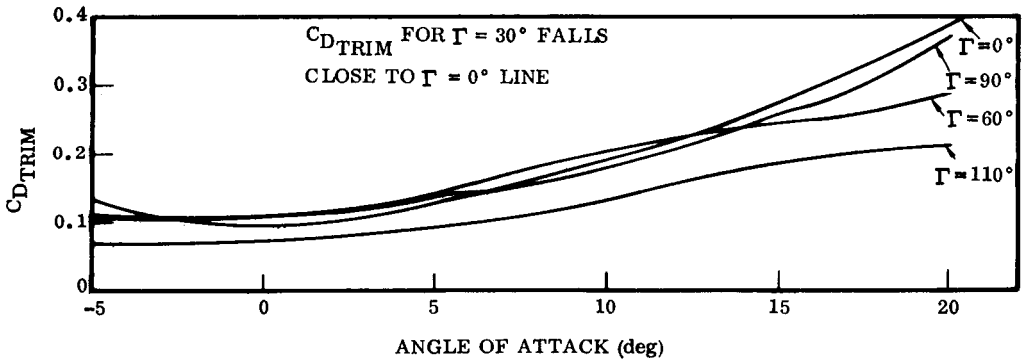

Figure 3-19. Trim Drag Coefficient

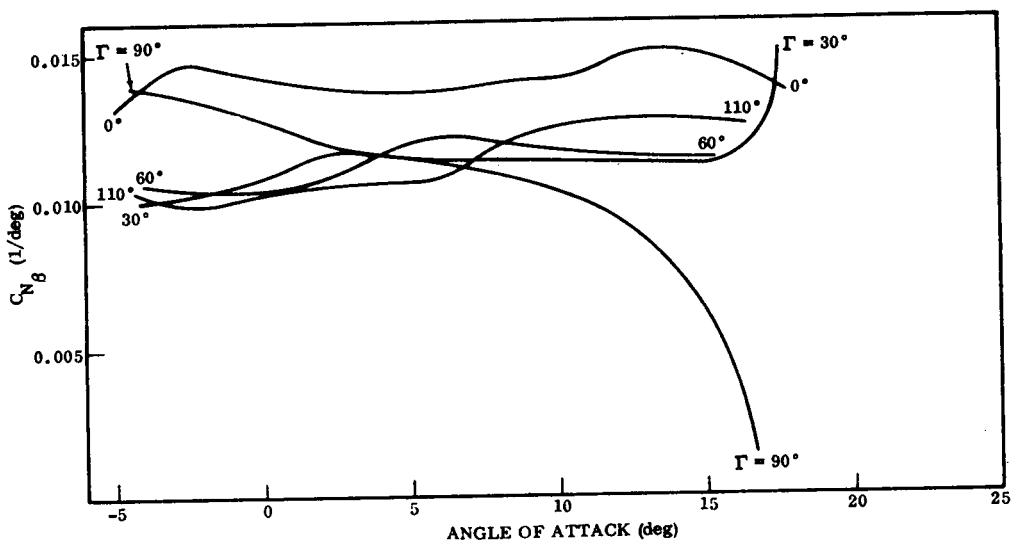

Figure 3-20. Subsonic Directional Stability Parameter

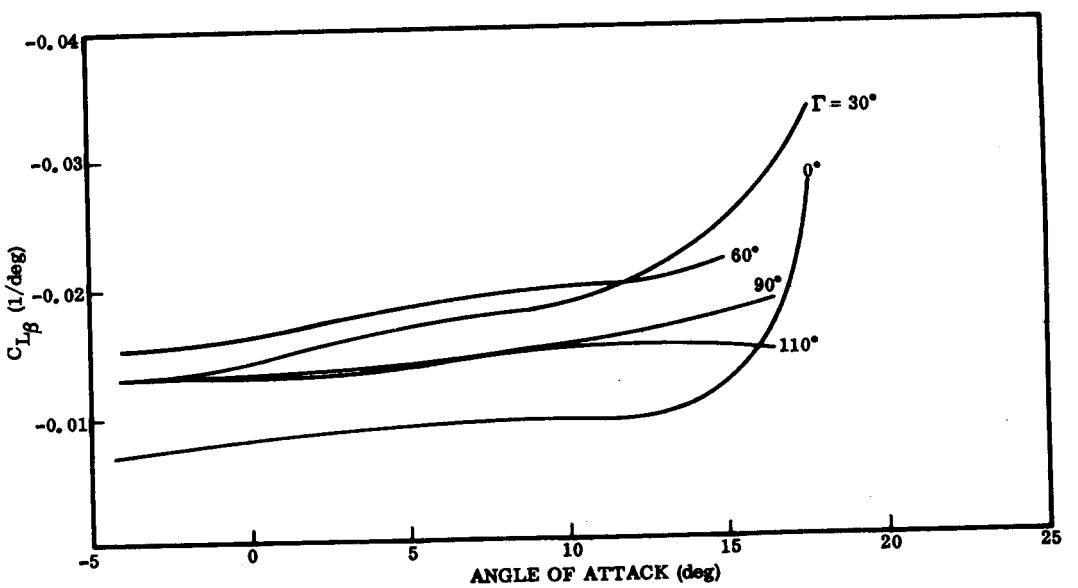

Figure 3-21. Subsonic Rolling Moment Derivative Due to Sideslip

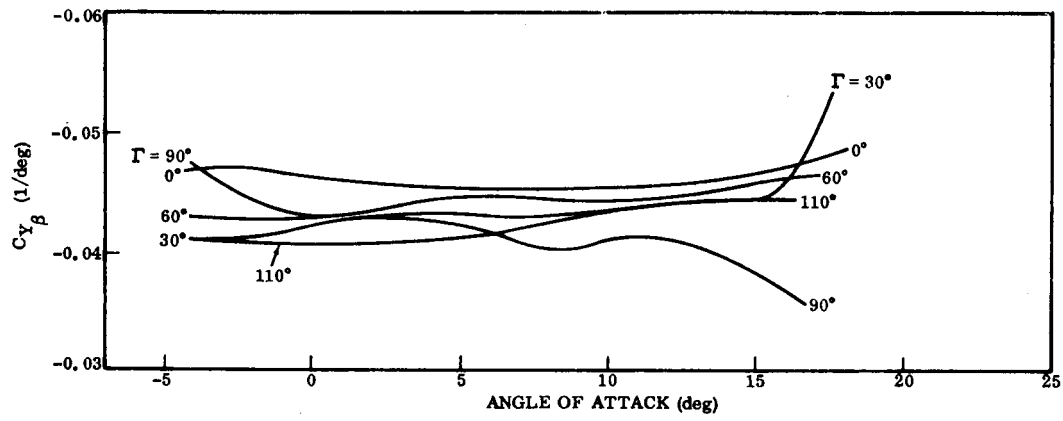

Figure 3-22. Subsonic Sideforce Stability Parameter

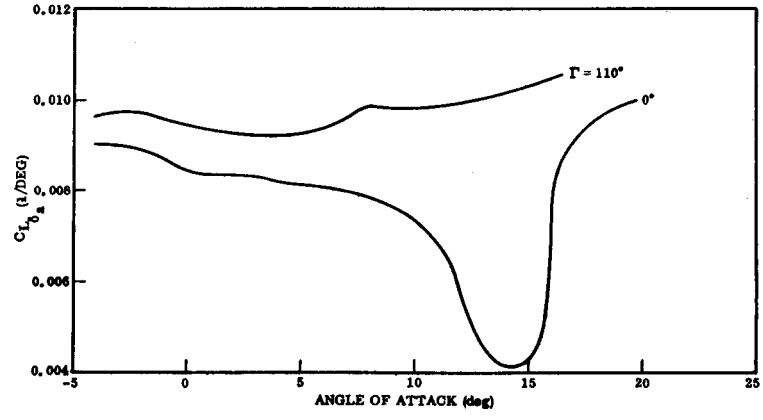

Figure 3-23. Subsonic Roll Moment Derivative Due to Aileron

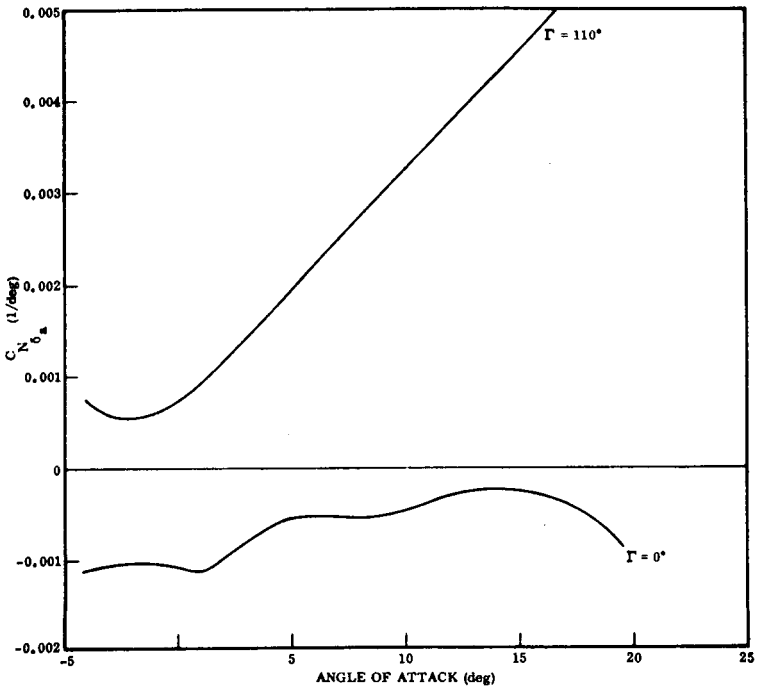

Figure 3-24. Subsonic Yaw Moment Derivative Due to Aileron

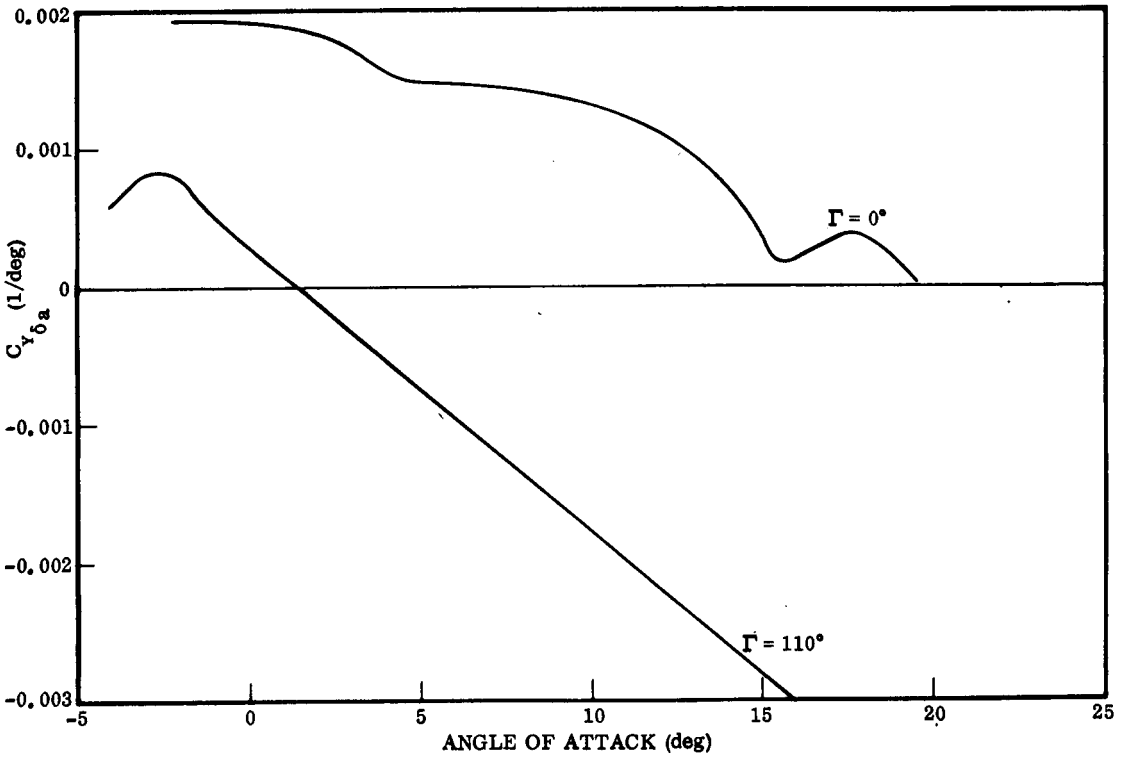

Figure 3-25. Subsonic Sideforce Derivative Due to Aileron

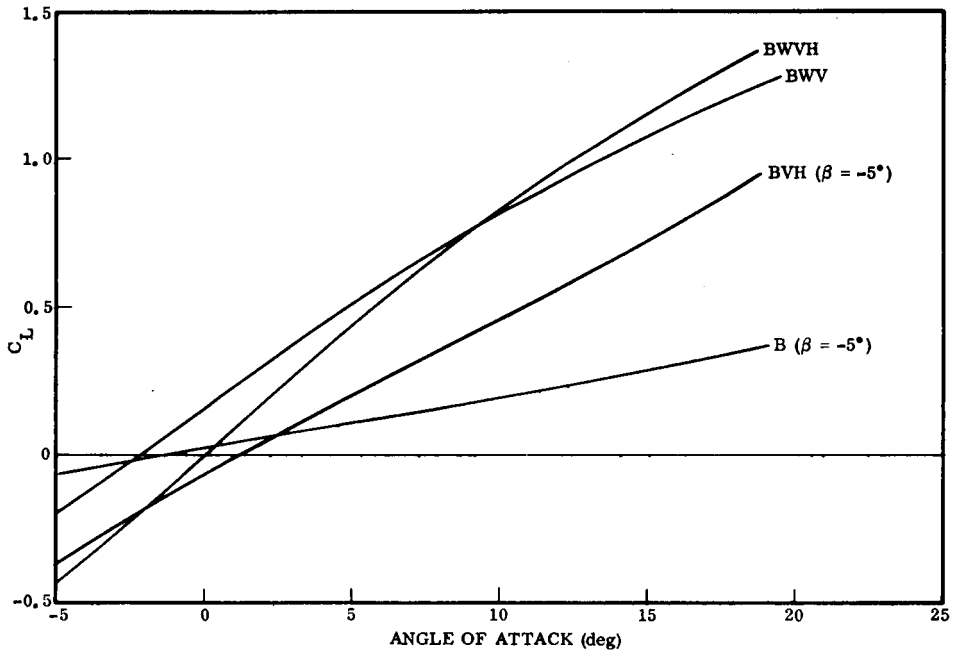

Figure 3-26. Subsonic Horizontal Tail On and Off Lift Coefficients

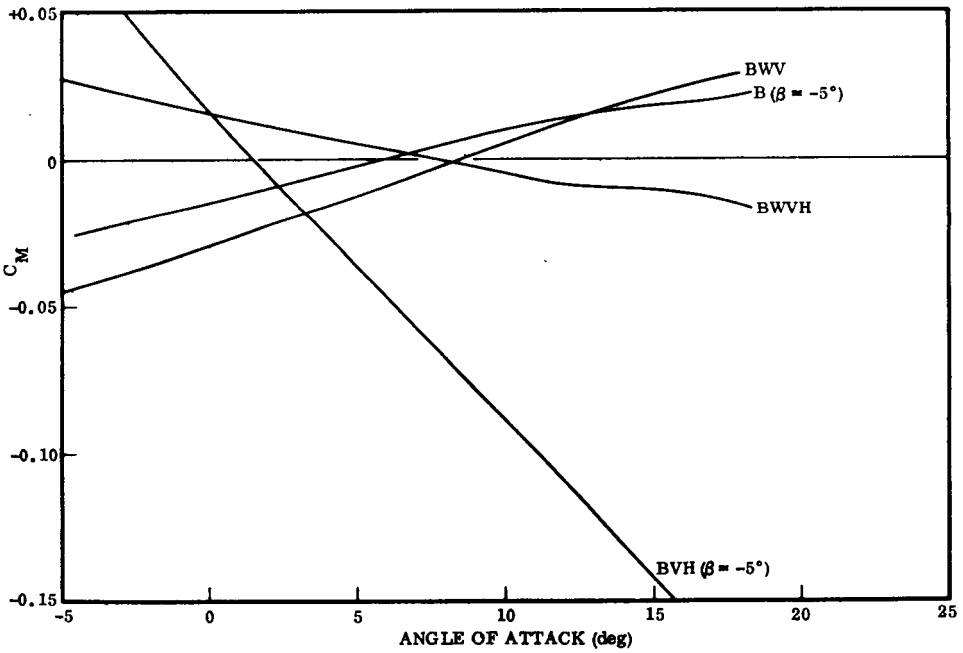

Figure 3-27. Subsonic Horizontal Tail On and Off Pitch Coefficients

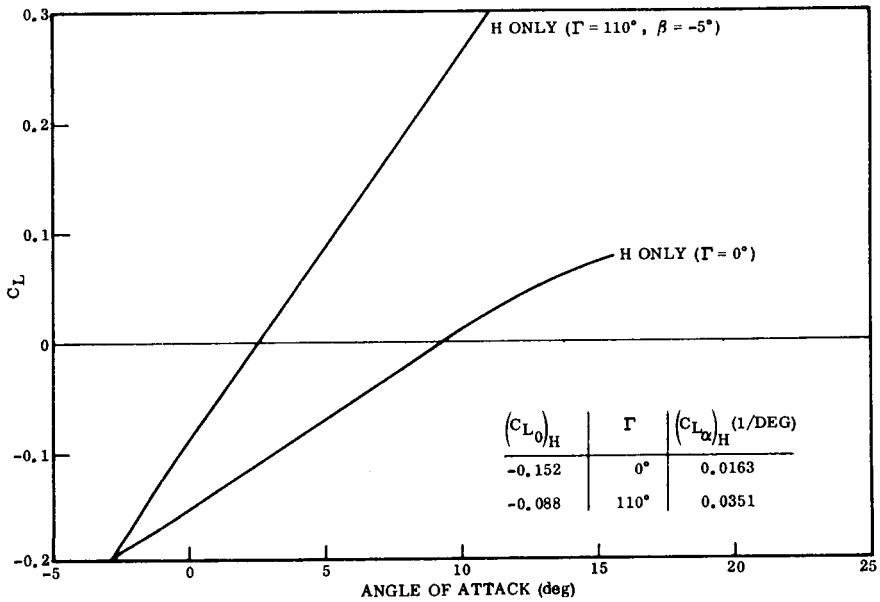

Figure 3-28. Subsonic Horizontal Tail Contribution to Lift Coefficient

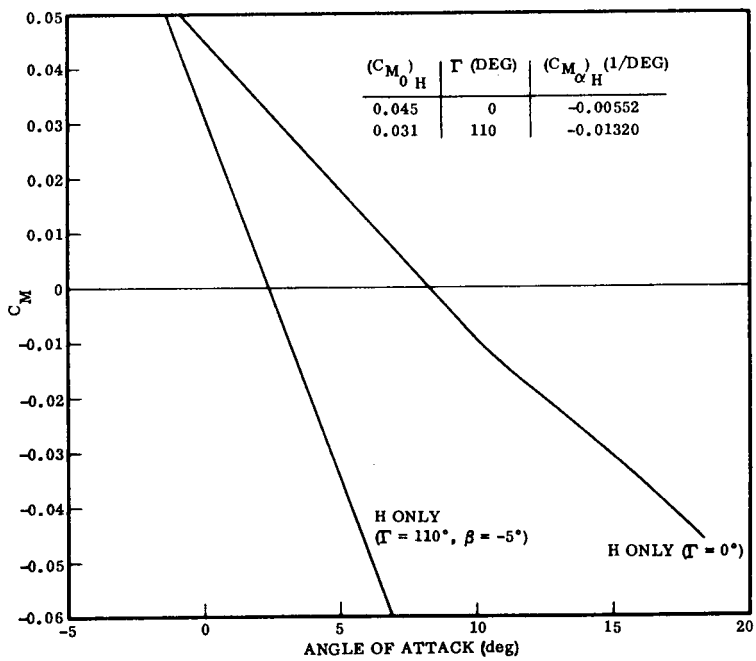

Figure 3-29. Subsonic Horizontal Tail Contribution to Pitch Moment Coefficient

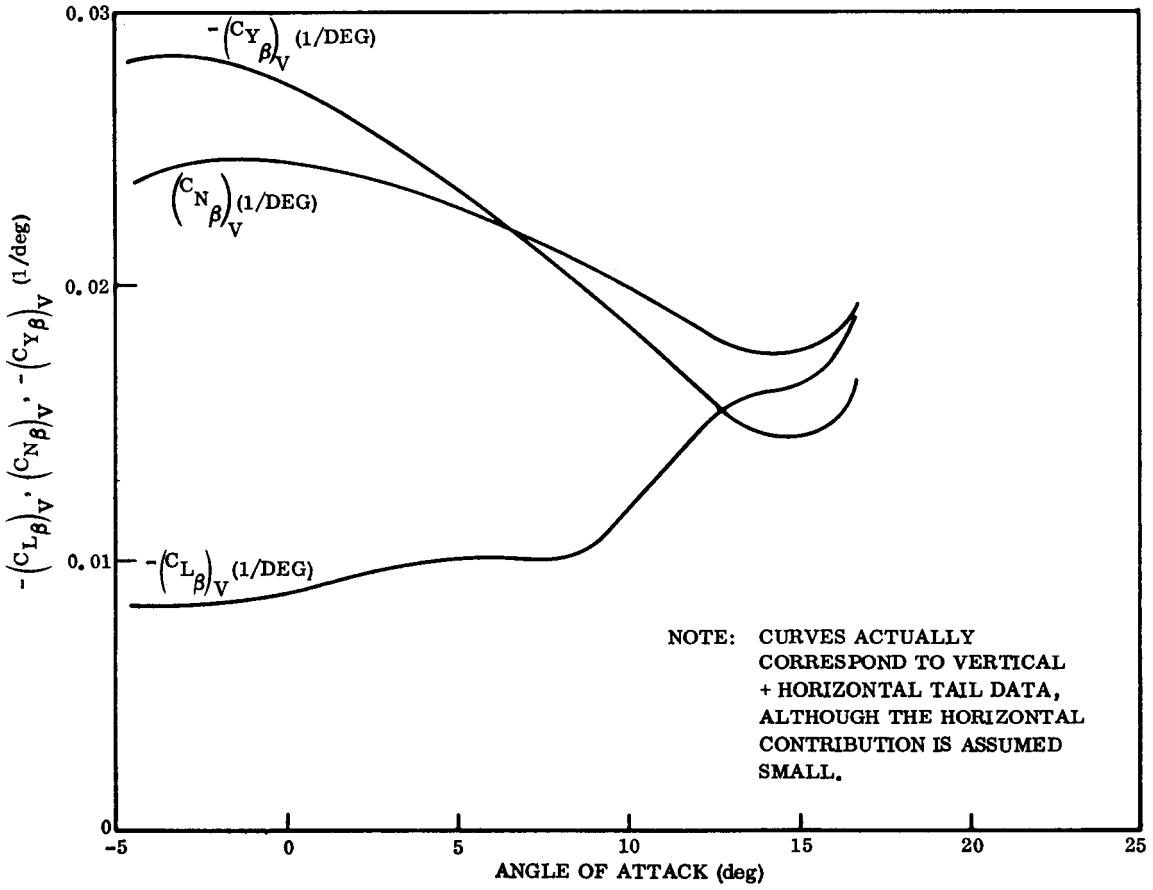

Figure 3-30. Subsonic Vertical Tail Contribution to Sideslip Derivatives

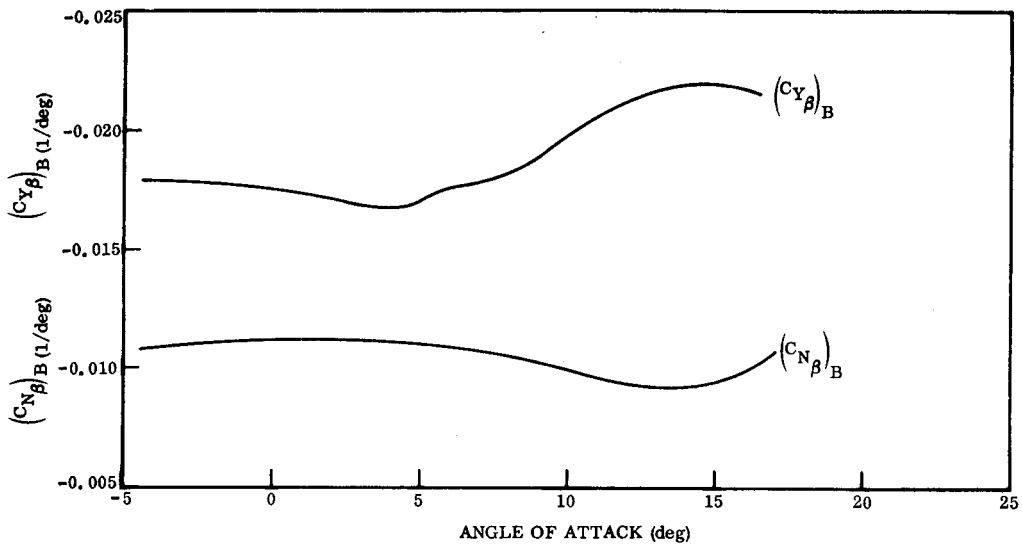

a.

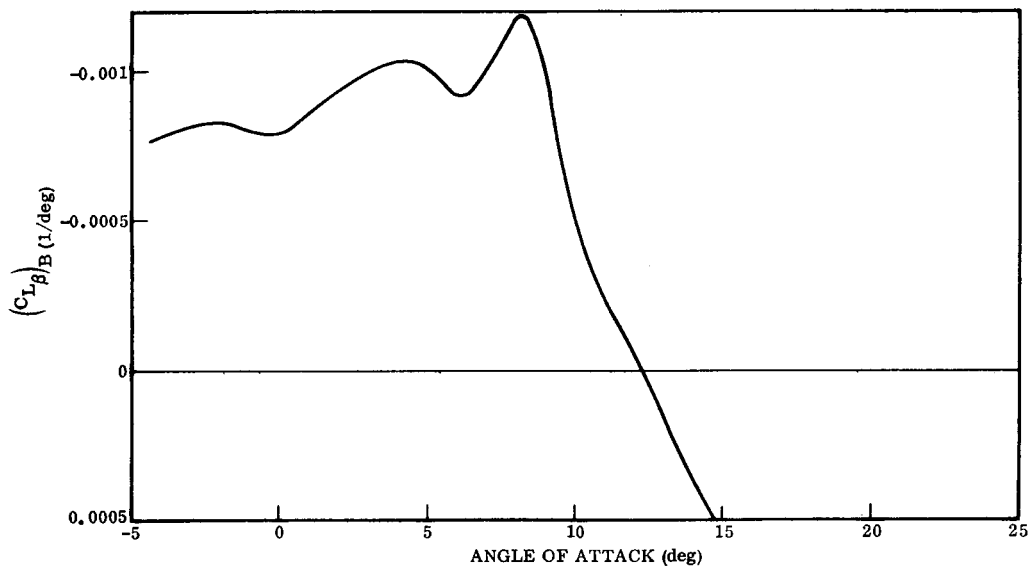

b.

Figure 3-31. Subsonic Body Alone Contribution to Sideslip Derivatives

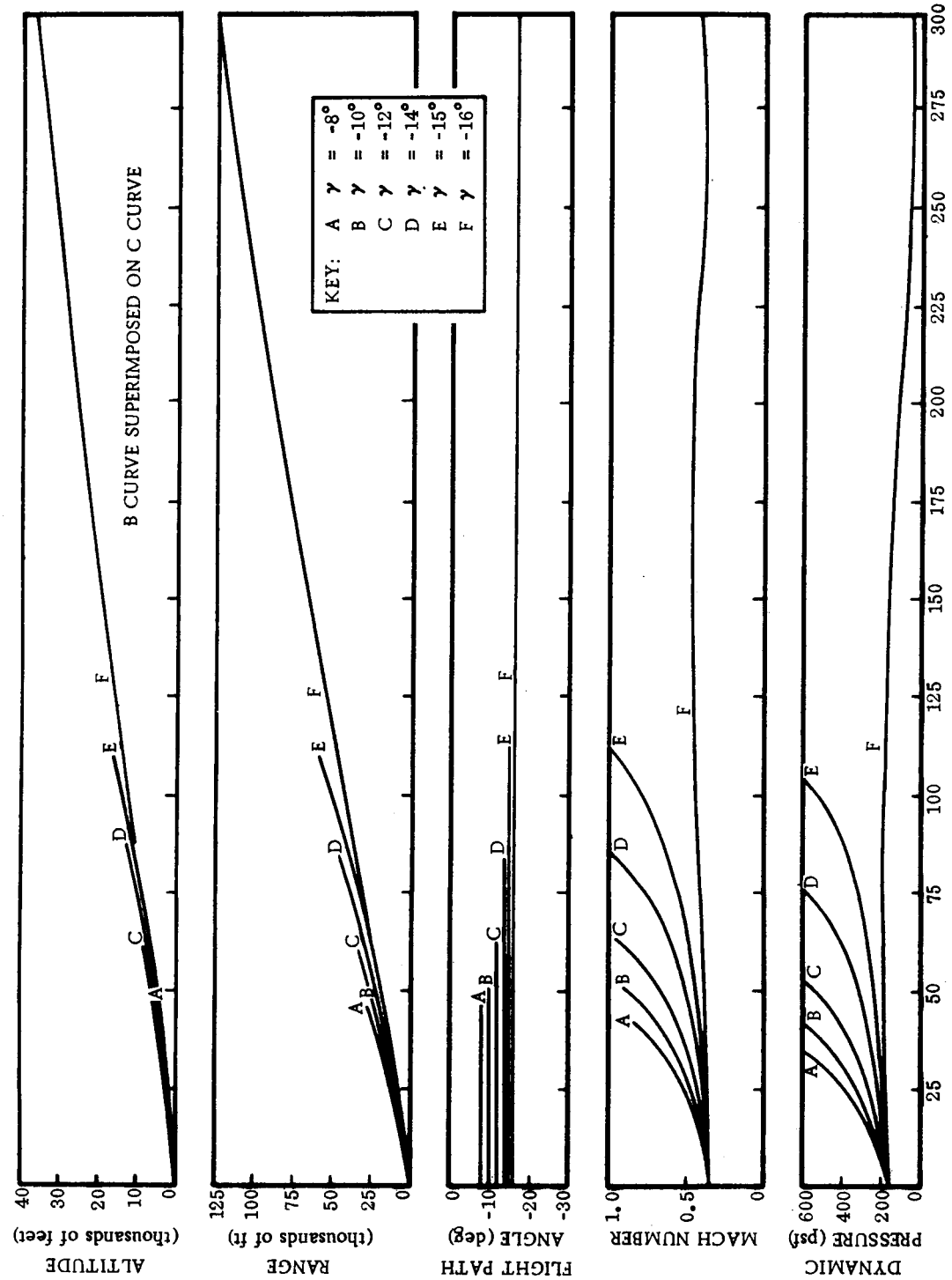

Figure 5-1. Constant Flight Path Trajectories

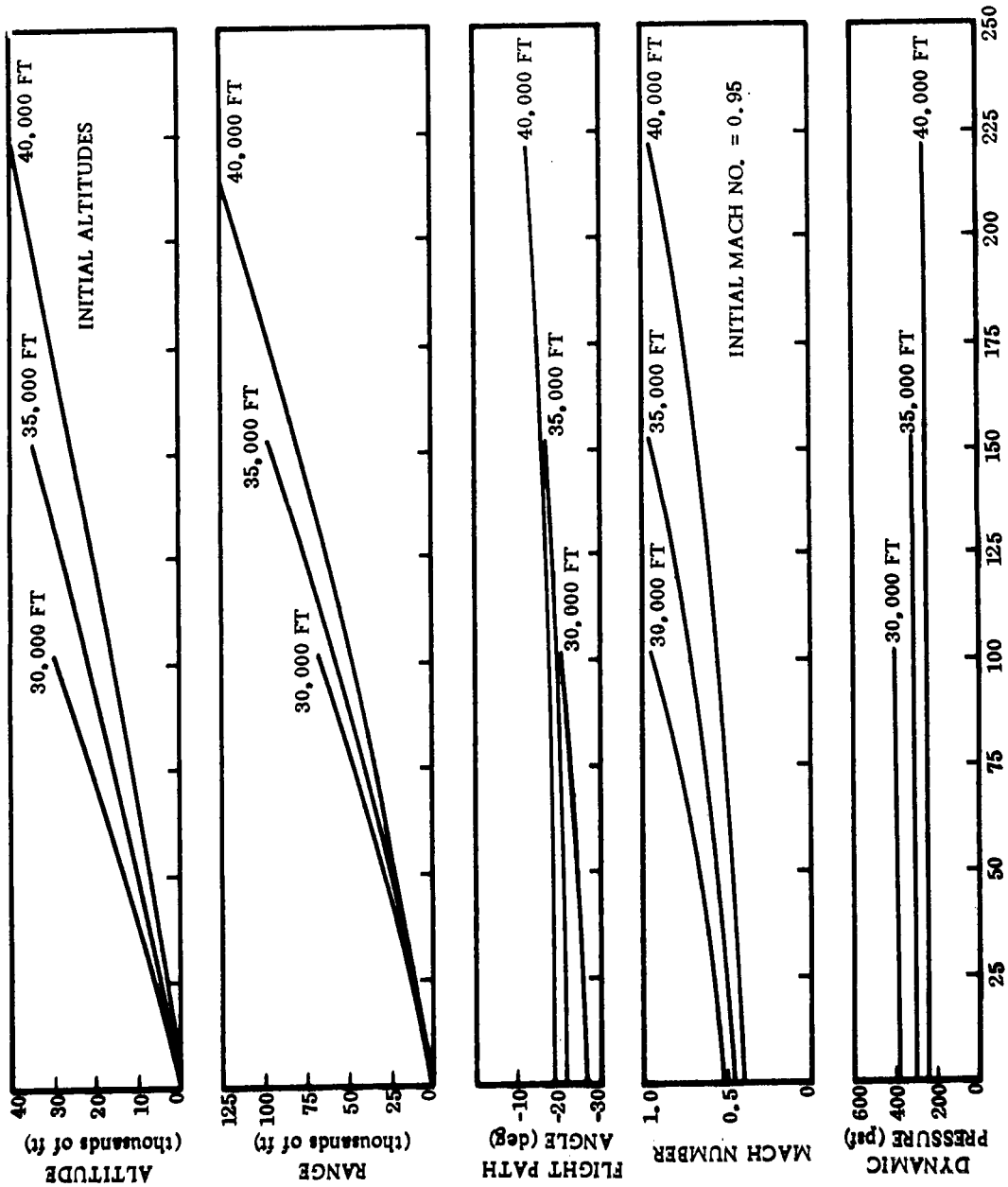

Figure 5-2. Constant Dynamic Pressure Flight Trajectories

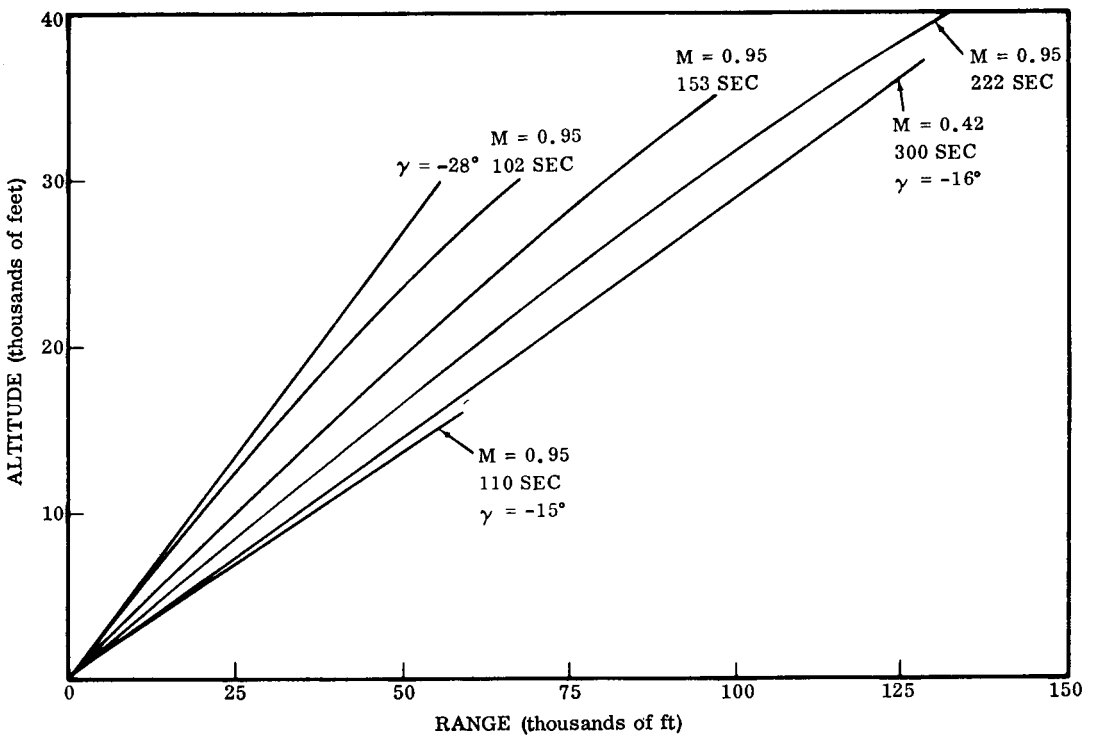

Figure 5-3. Altitude and Range Plot for Constant Dynamic Pressure and Constant Flight Path Angle Trajectories

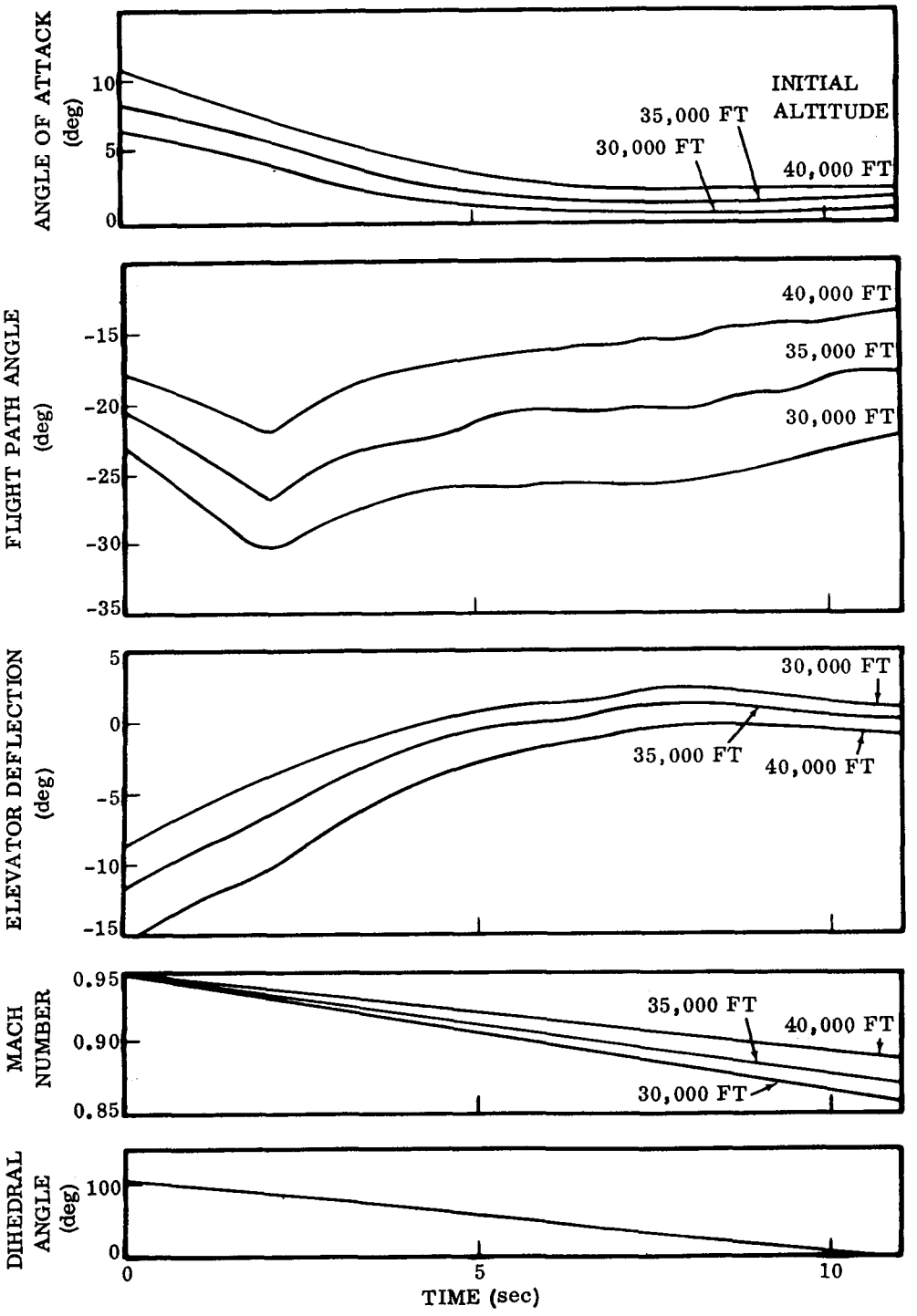

Figure 5-4. Constant Dynamic Pressure; Steady-State Wing Deployment Starting at Mach 0.95 and 30,000 Feet, 35,000 Feet, and 40,000 Feet

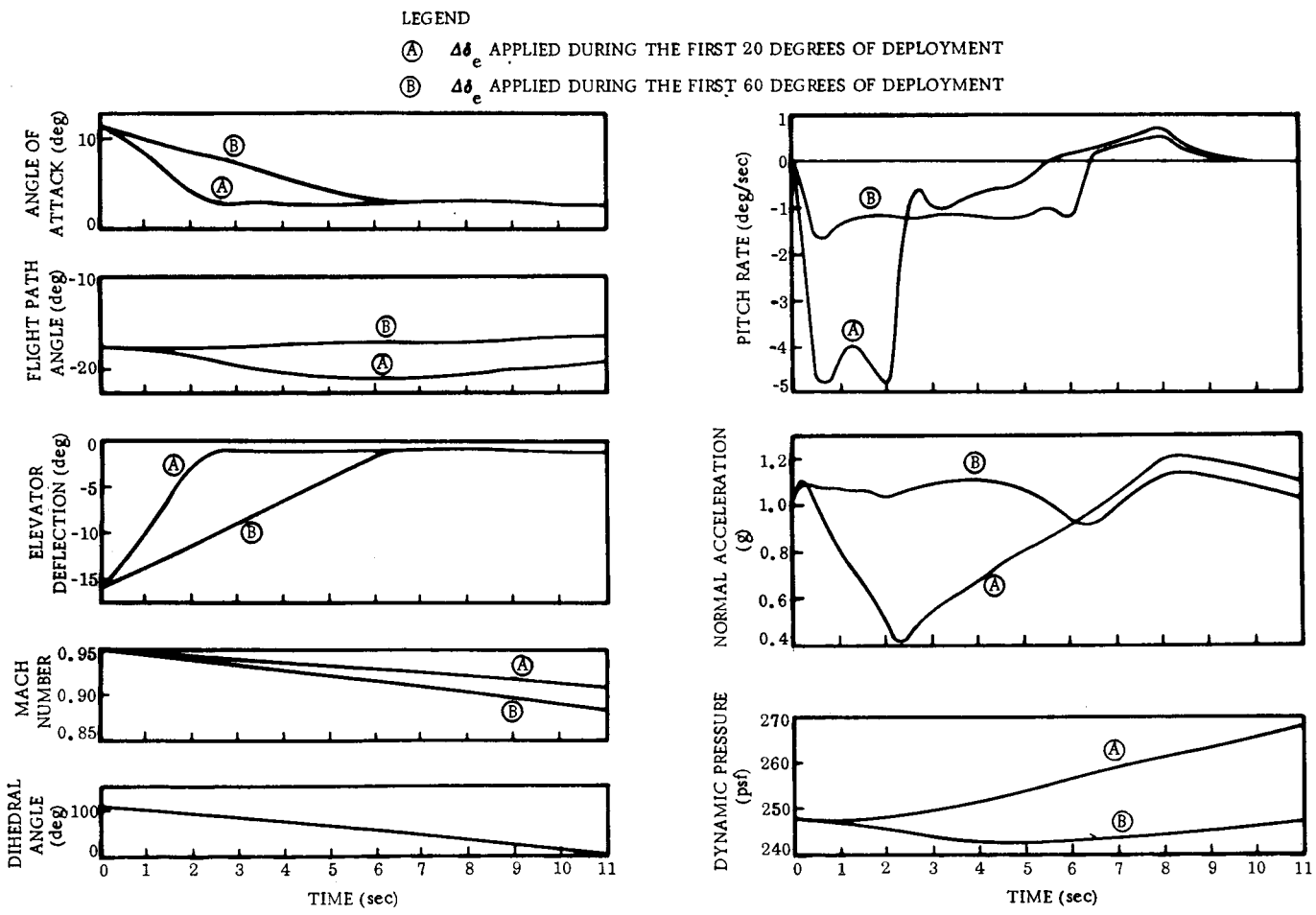

Figure 5-5. Wing Deployment Starting at M = 0.95 and H = 40,000 Feet with Programmed Elevator Interconnect

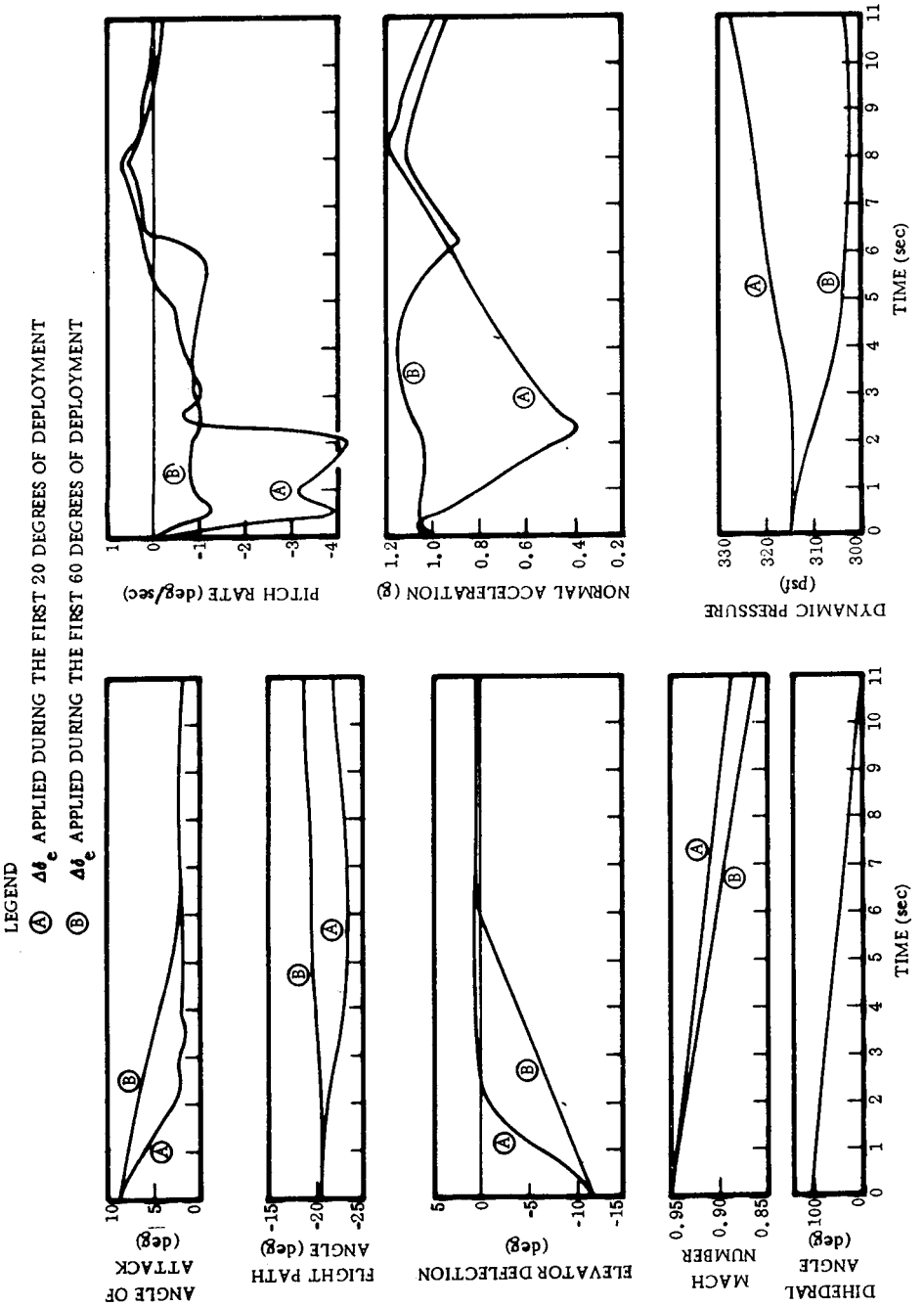

Figure 5-6. Wing Deployment at M = 0.95 and H = 35,000 Feet with Programmed Elevator Interconnect

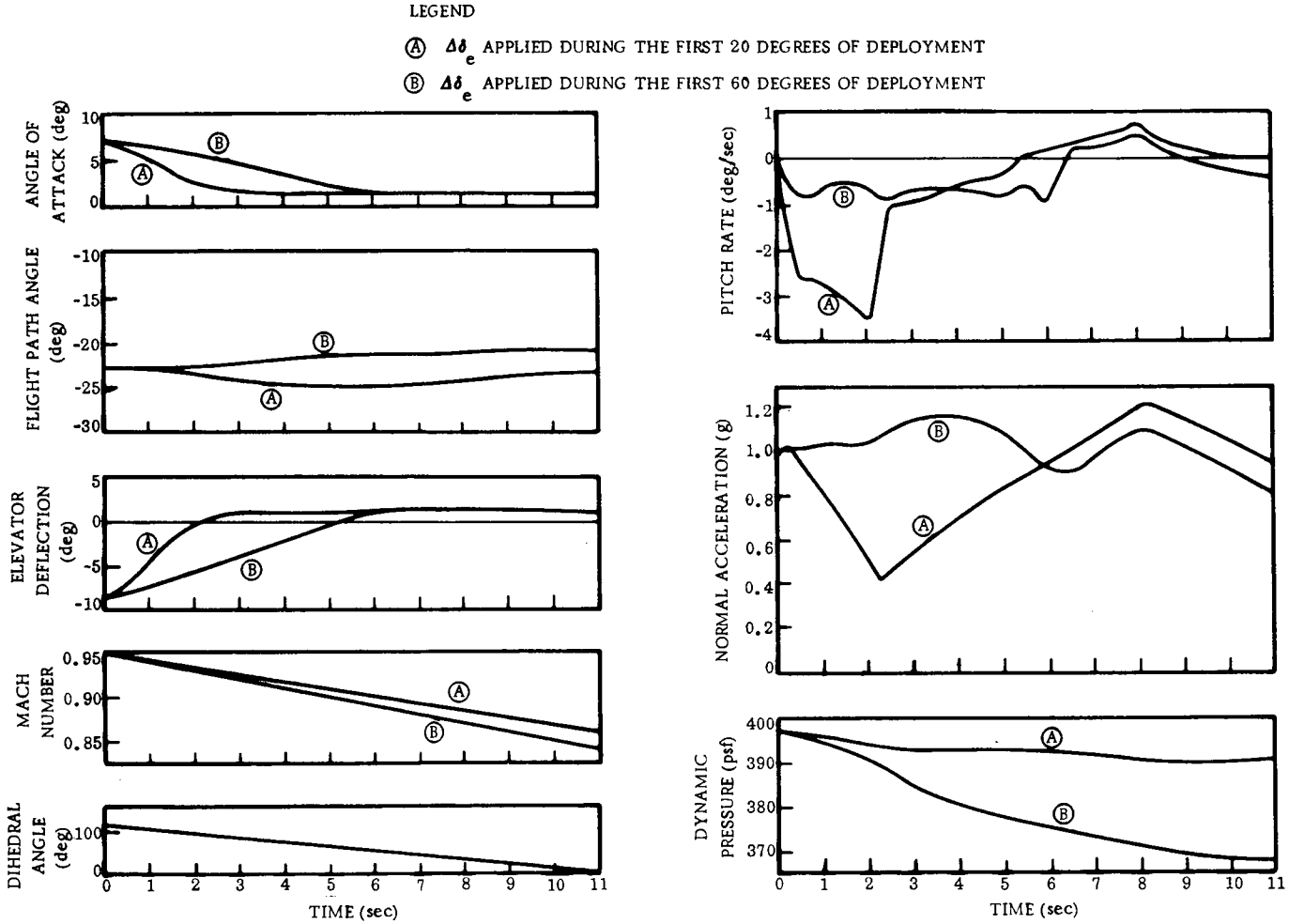

Figure 5-7. Wing Deployment at M = 0.95 and H = 30,000 Feet with Programmed Elevator Interconnect

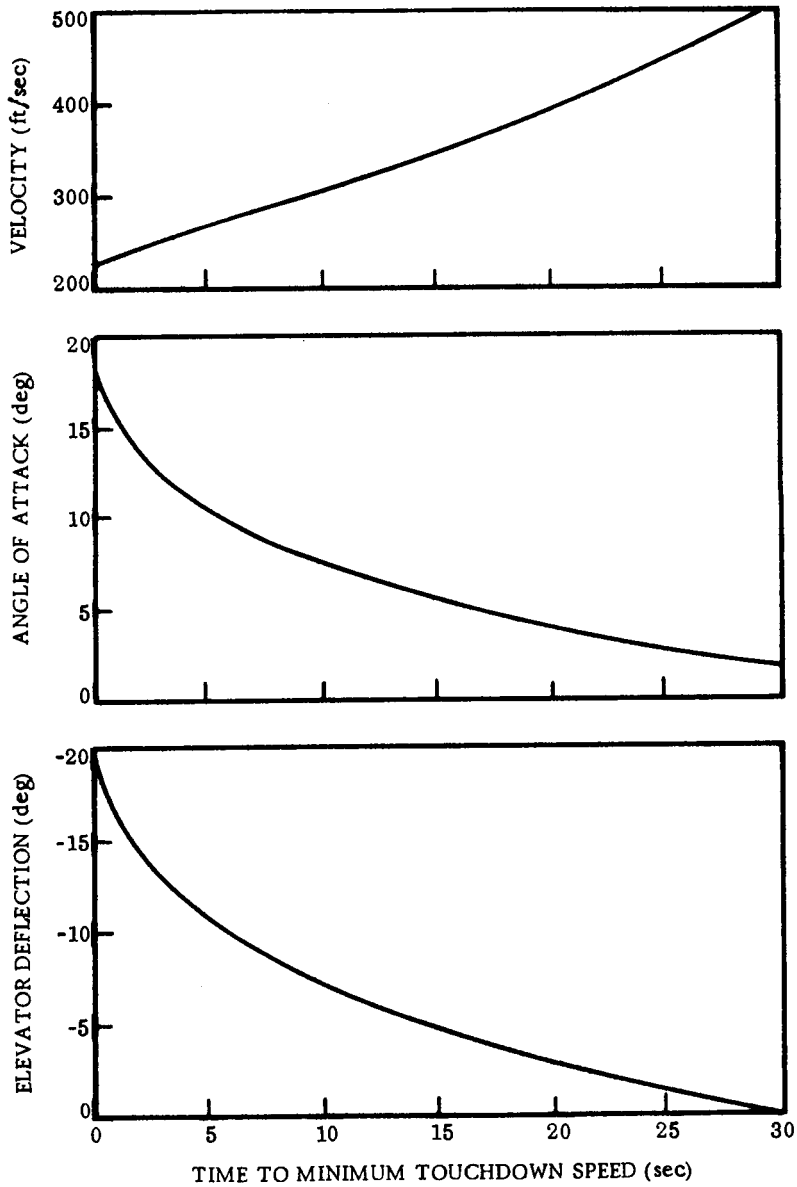

Figure 5-8. Landing Float Deceleration

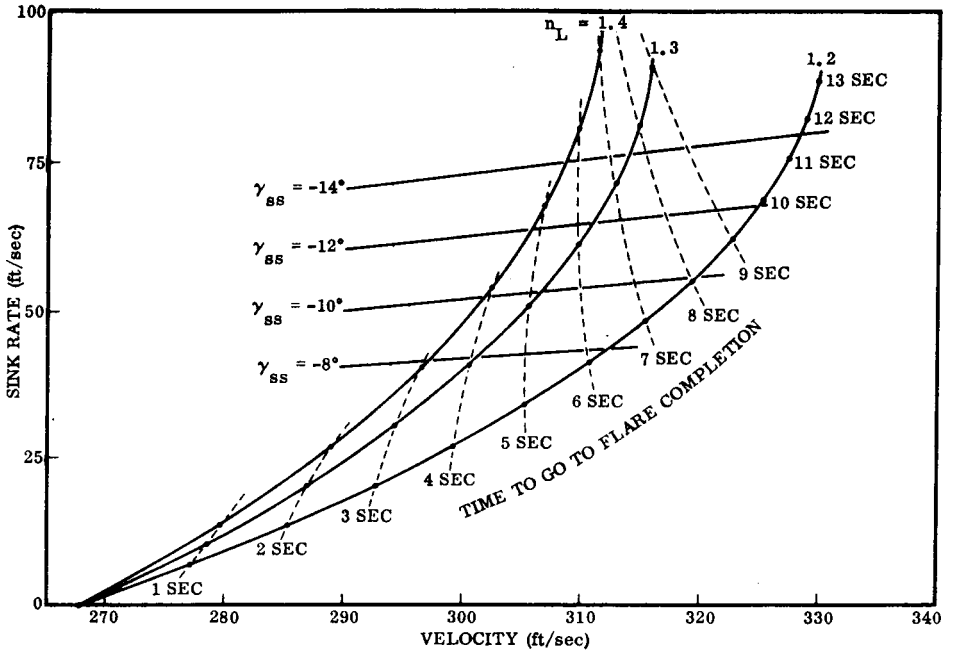

Figure 5-9. Flare and Steady-State Glide Trajectories with Time Cross Plotted (T_{FLOAT} = 5 sec)

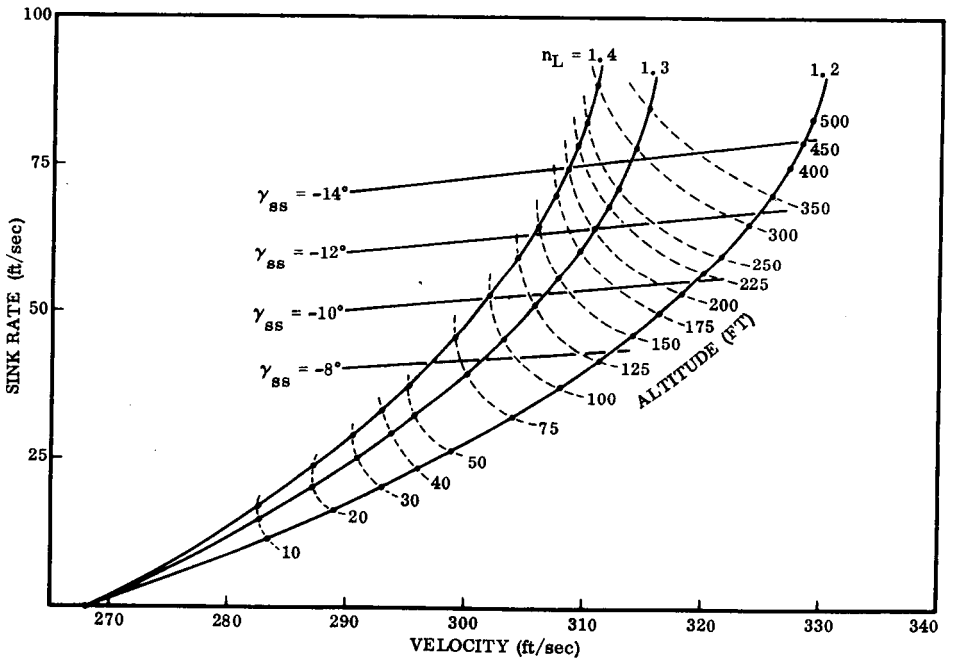

Figure 5-10. Flare and Steady-State Glide Trajectories with Altitude Cross Plotted (T_{FLOAT} = 5 sec)

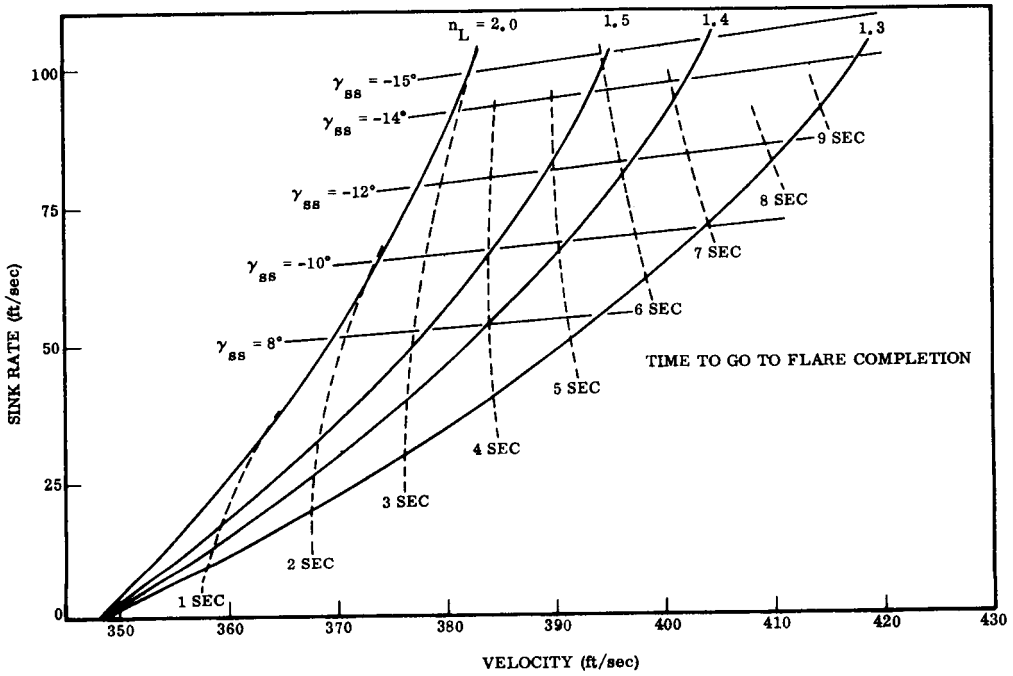

Figure 5-11. Flare and Steady-State Glide Trajectories with Time Cross Plotted (T_{FLOAT} = 15 sec)

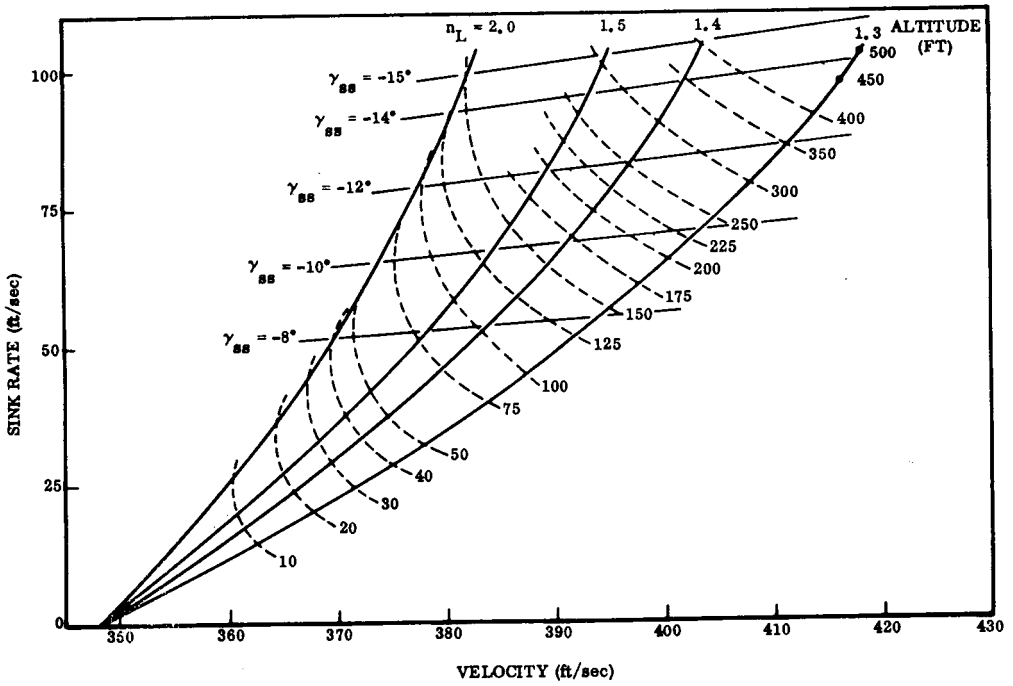

Figure 5-12. Flare and Steady-State Glide Trajectories with Altitude Cross Plotted (T_{FLOAT} = 15 sec)

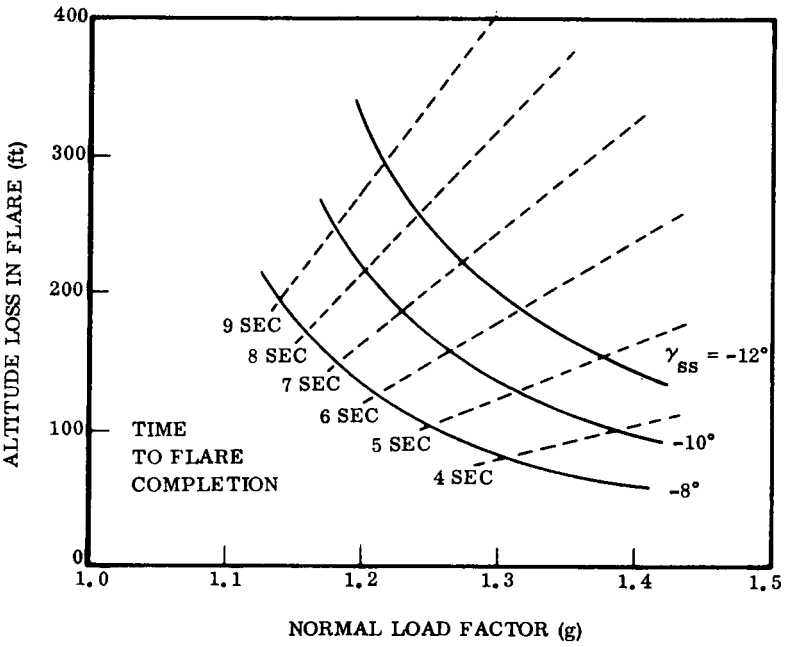

Figure 5-13. Altitude Loss During Flare (T_{FLOAT} = 5 sec)

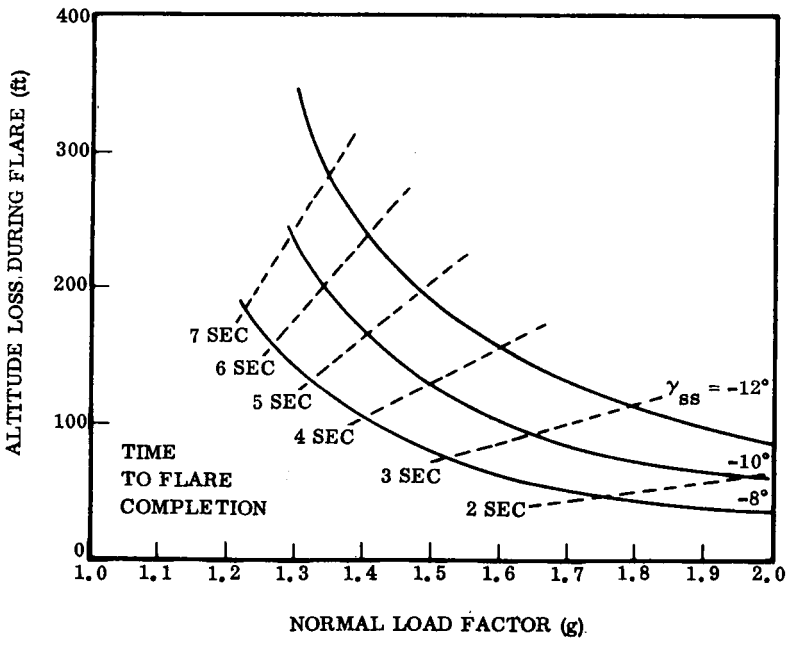

Figure 5-14. Altitude Loss During Flare (T_{FLOAT} = 15 sec)

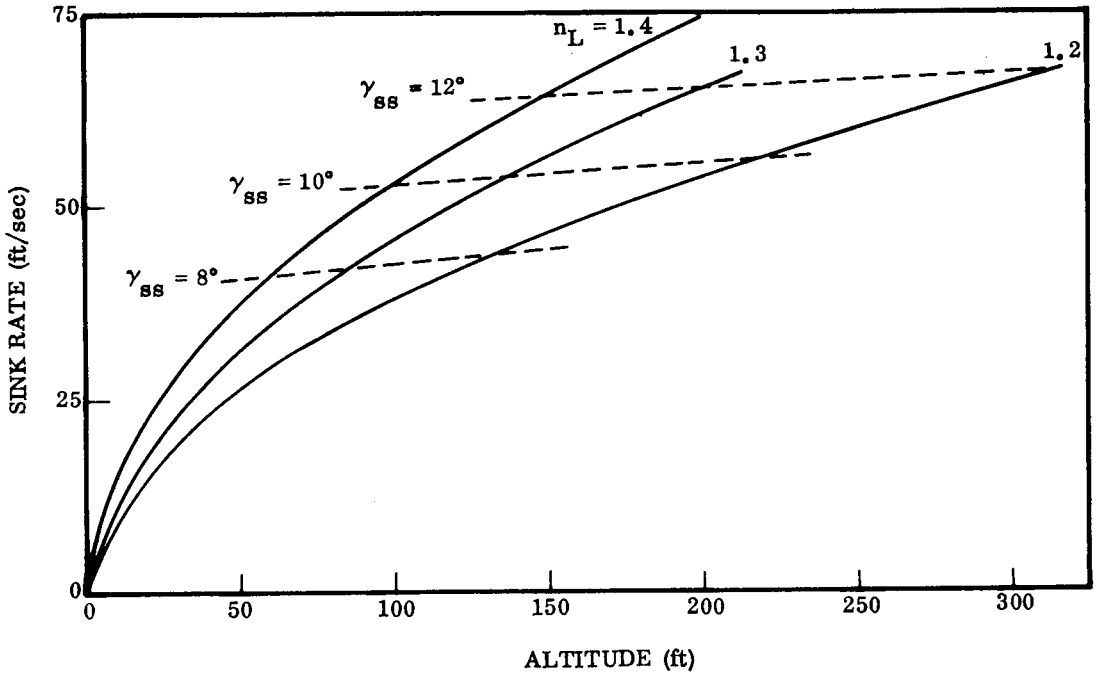

Figure 5-15. Altitude and Sink Rate During Flare (T_{FLOAT} = 5 sec)

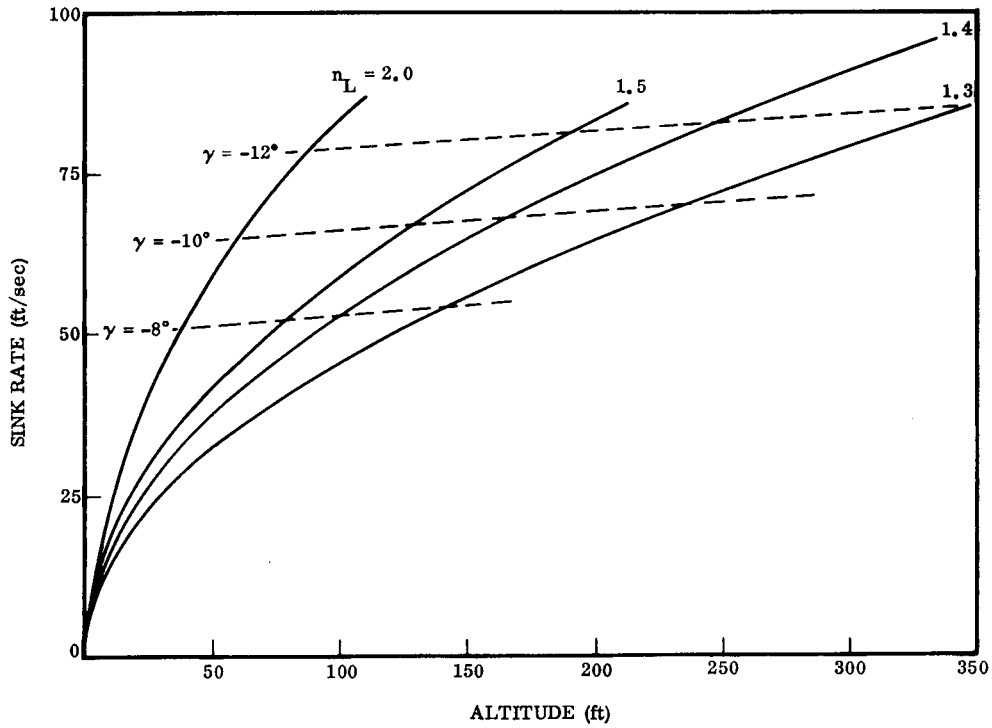

Figure 5-16. Altitude and Sink Rate During Flare (T_{FLOAT} = 15 sec)

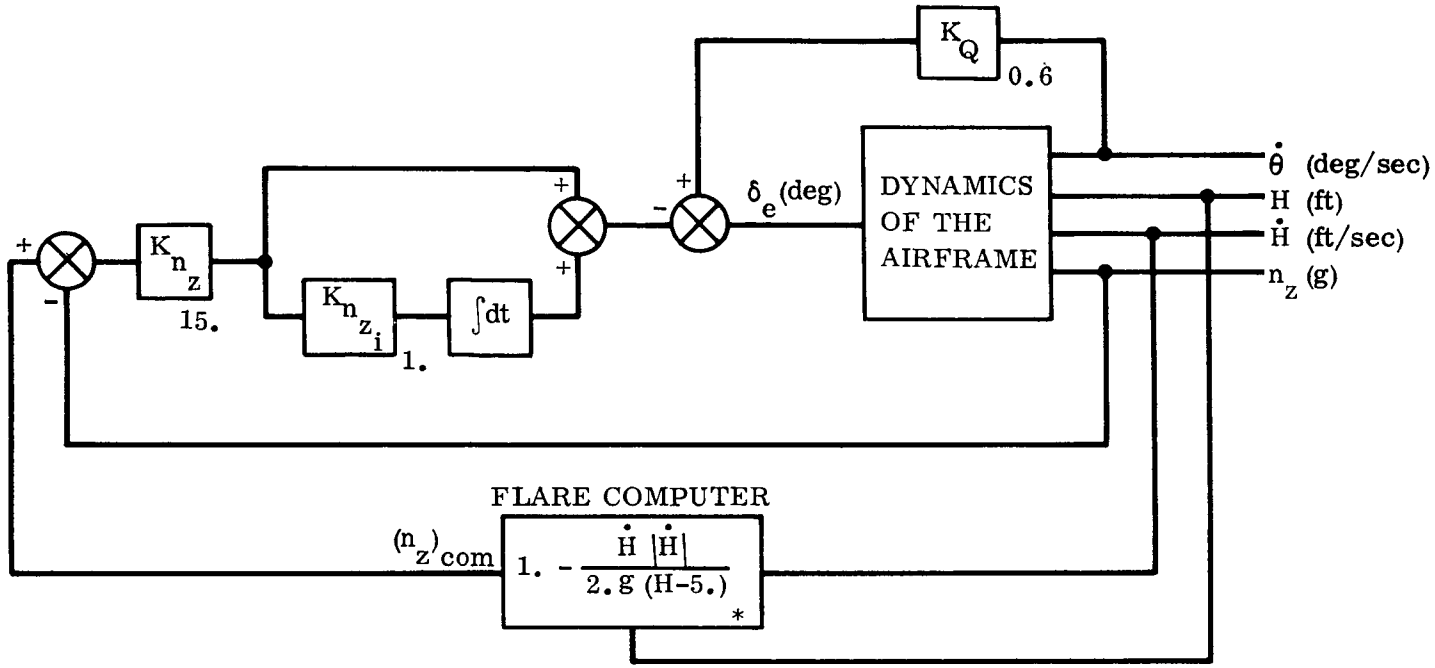

*H-5 is limited to being greater than or equal to 5 ft.

Figure 5-17. Flare Computer

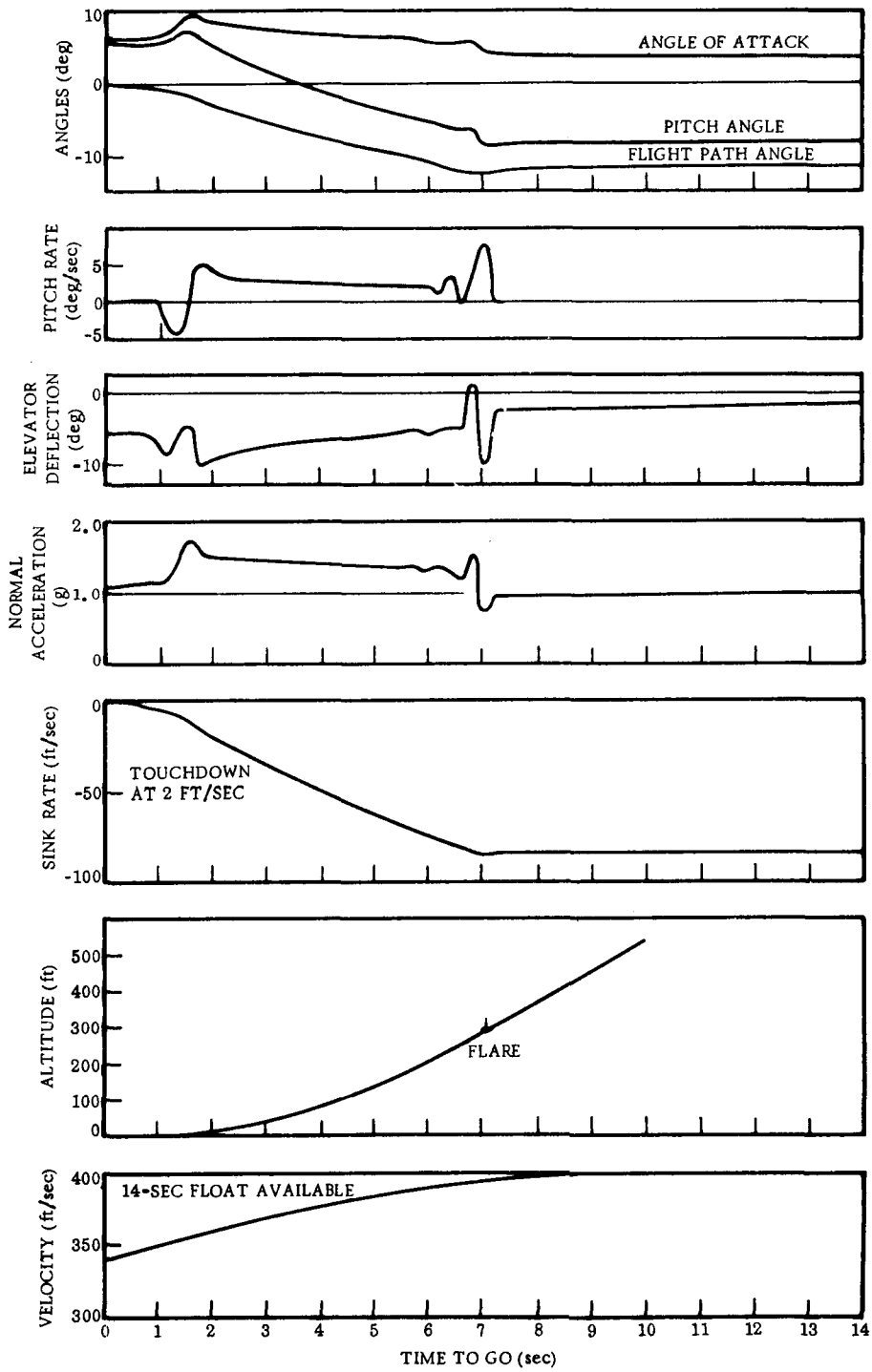

Figure 5-18. Landing Flare Initiated at 300 Feet

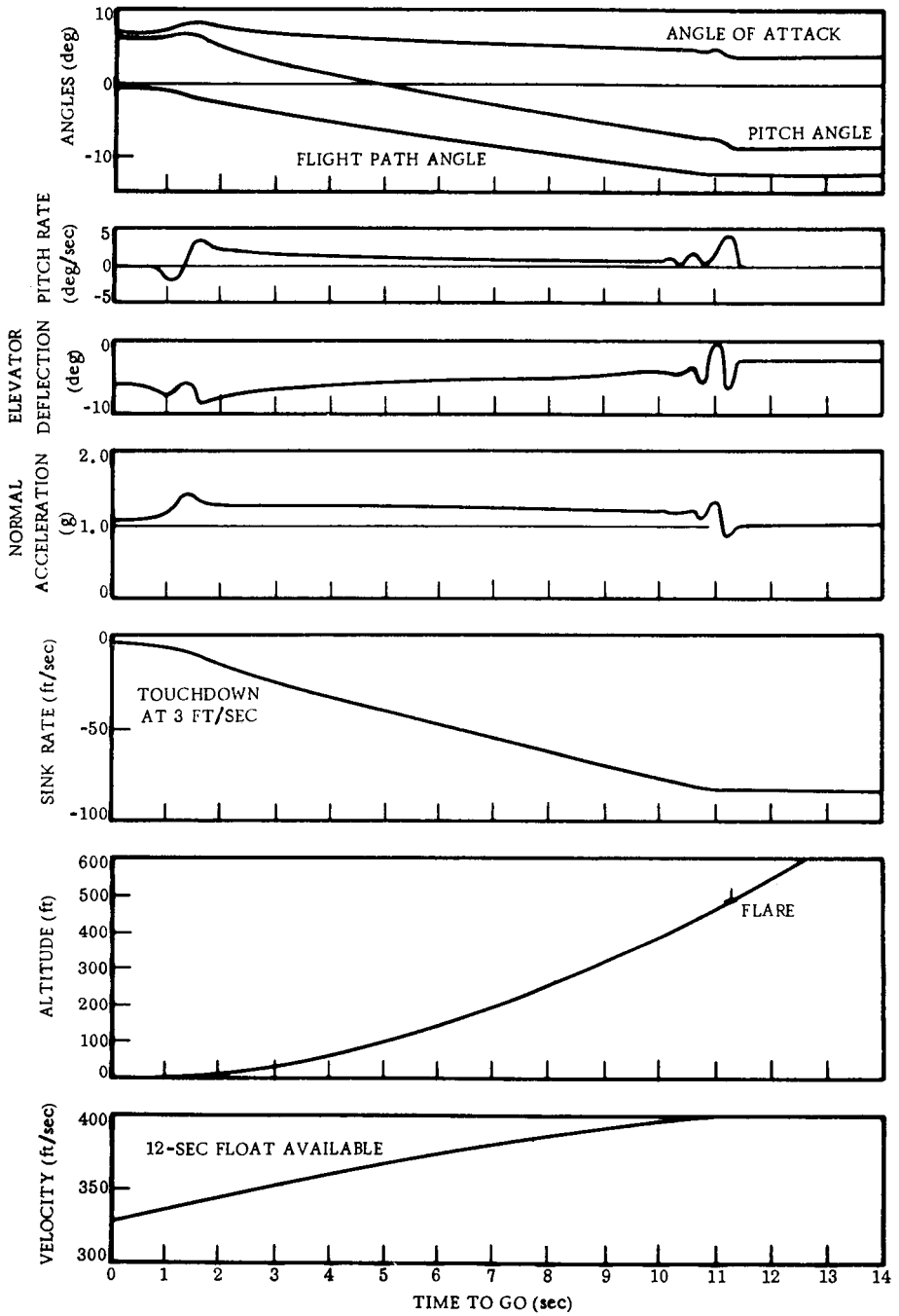

Figure 5-19. Landing Flare Initiated at 500 Feet

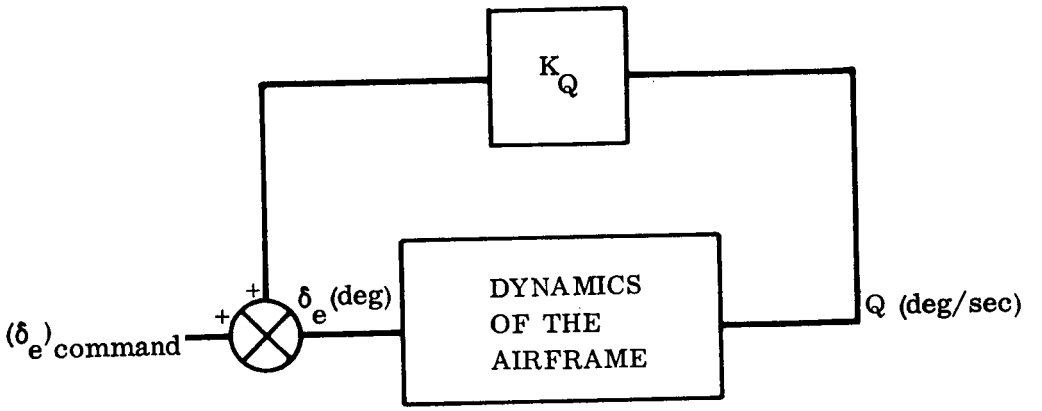

a. Pitch Stability Augmentation System

$$K_Q = 2.55\left(\frac{\bar{Q}}{1000}\right)^2 - 2.18\left(\frac{\bar{Q}}{1000}\right) + 0.68$$

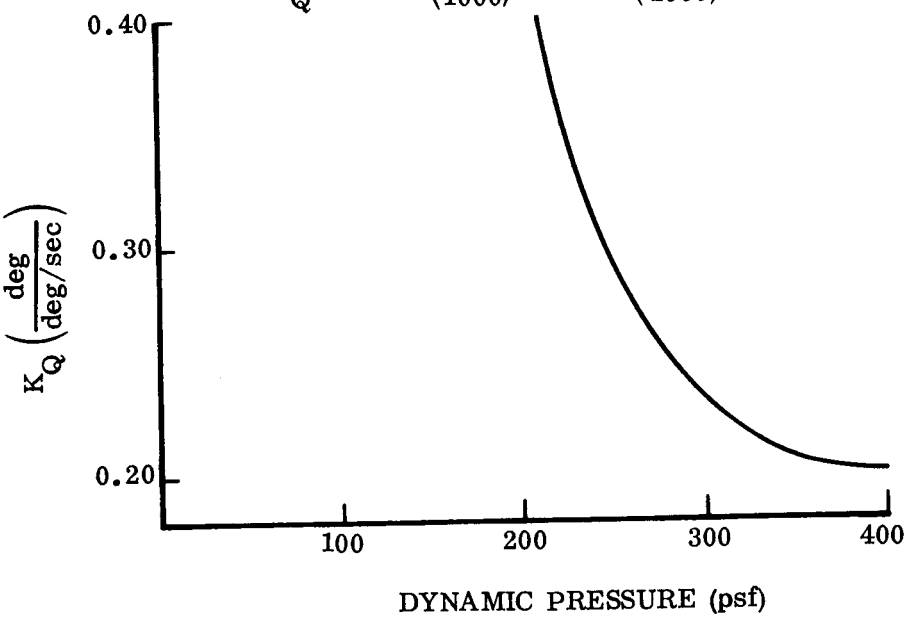

b. Gain Schedule

Figure 5-20. Pitch Stability Augmentation System

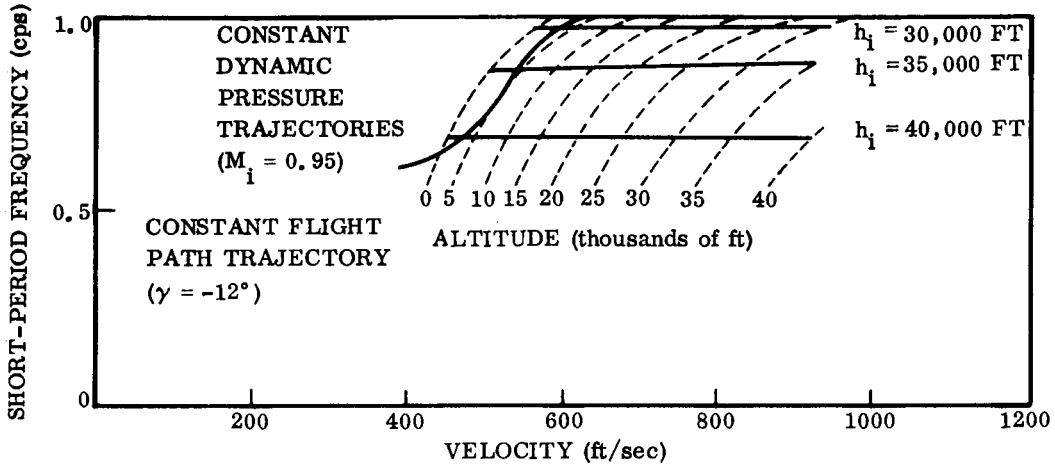

Figure 5-21. Longitudinal Short Period Frequency — Wing Deployed (Unaugmented)

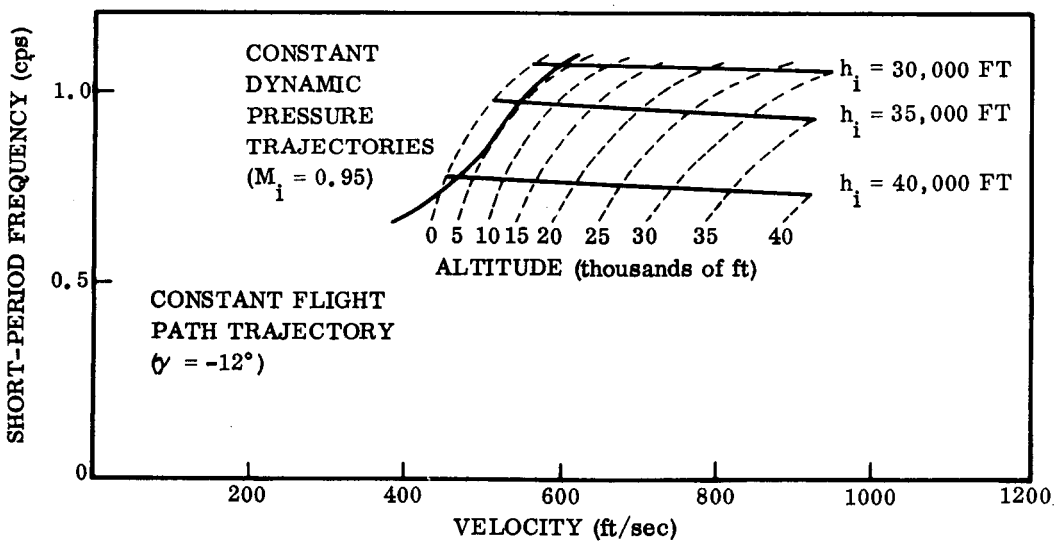

Figure 5-22. Longitudinal Short Period Frequency — Wing Deployed (Augmented)

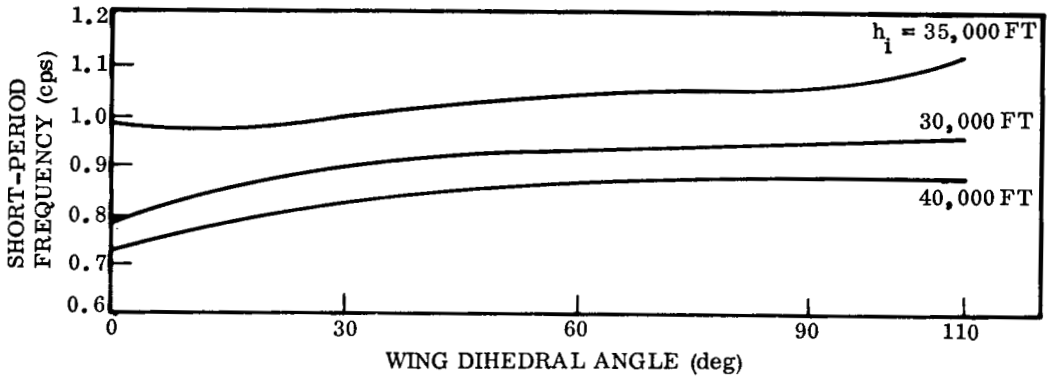

Figure 5-23. Short-Period Frequency — Wing Deployment Sequence (Unaugmented)

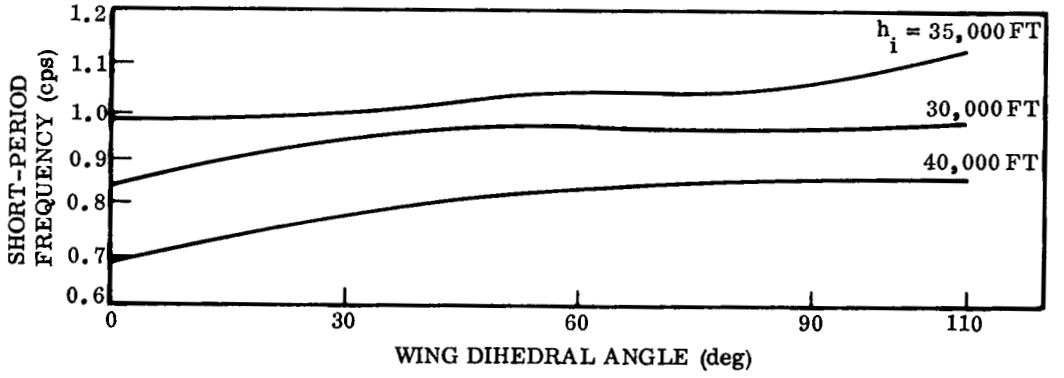

Figure 5-24. Short-Period Frequency — Wing Deployment Sequence (Augmented)

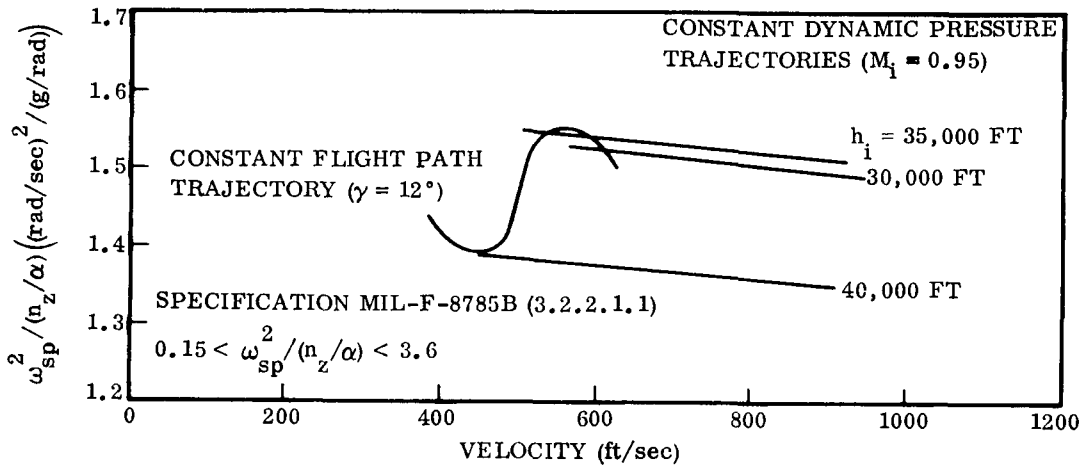

Figure 5-25. Short-Period Frequency Specification — Wings Deployed (Unaugmented)

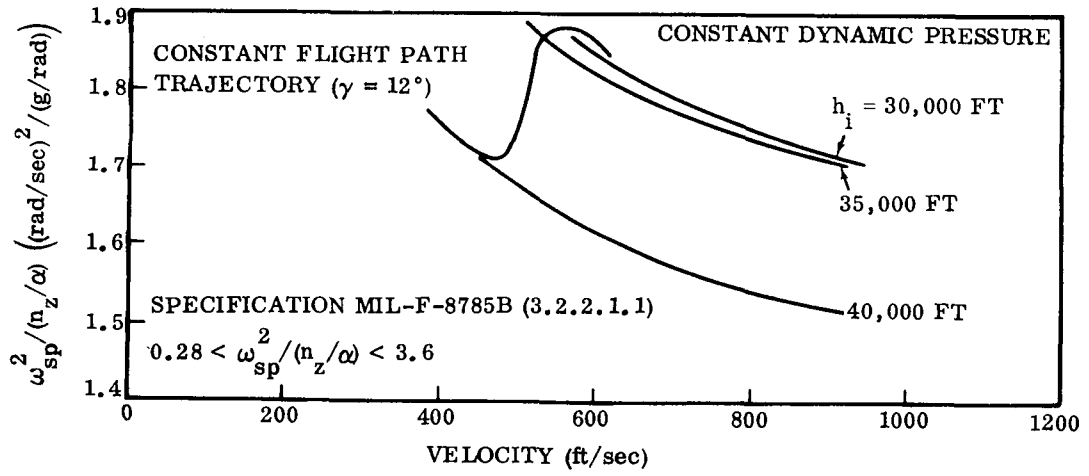

Figure 5-26. Short-Period Frequency Specification — Wings Deployed (Augmented)

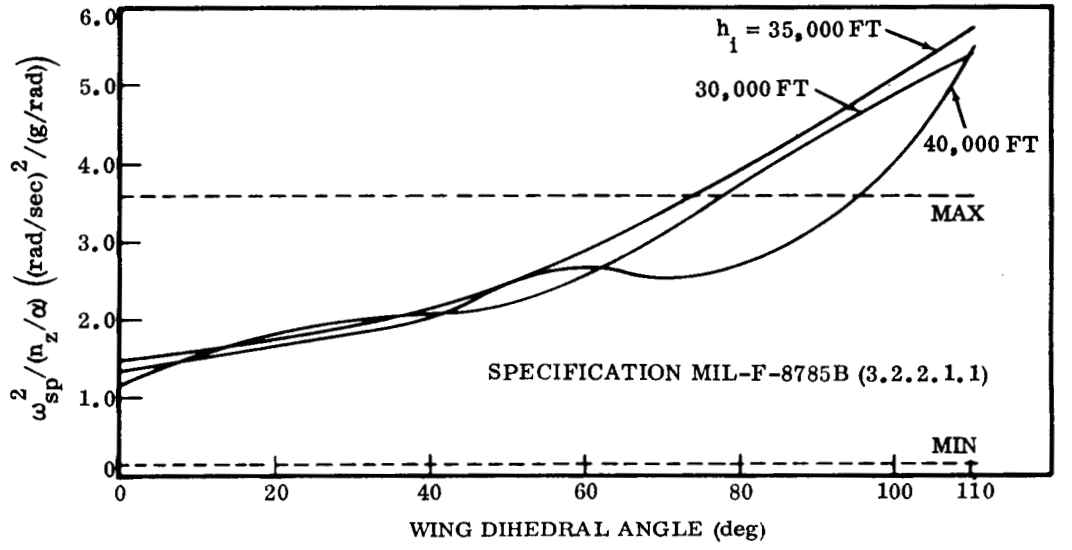

Figure 5-27. Short-Period Frequency Specification — Wing Deployment Sequence (Unaugmented)

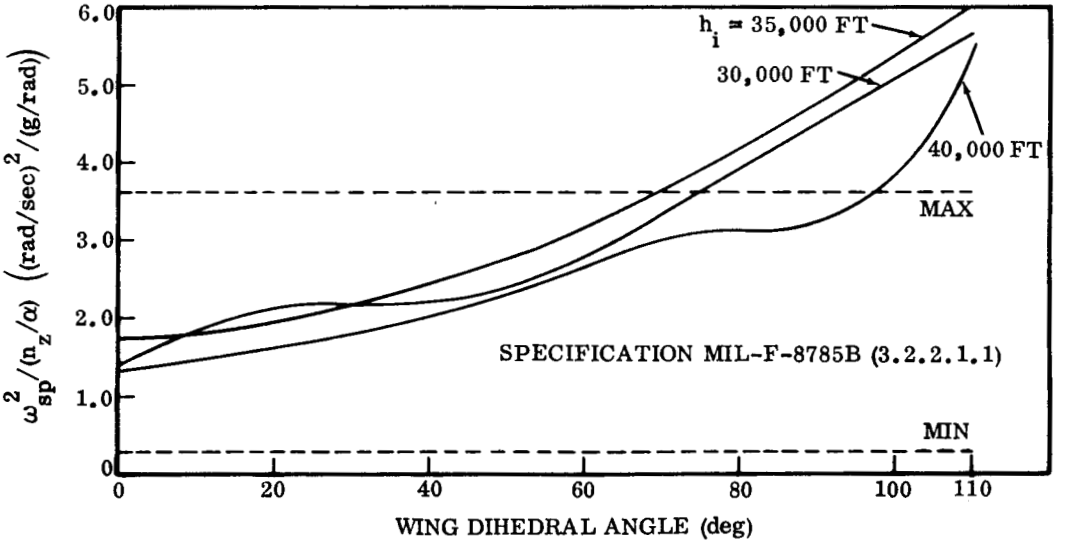

Figure 5-28. Short-Period Frequency Specification — Wing Deployment Sequence (Augmented)

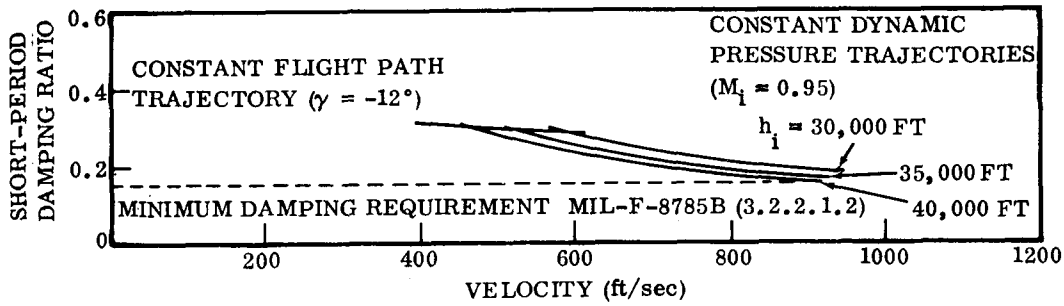

Figure 5-29. Longitudinal Short-Period Damping Ratio — Wing Deployed — No Augmentation

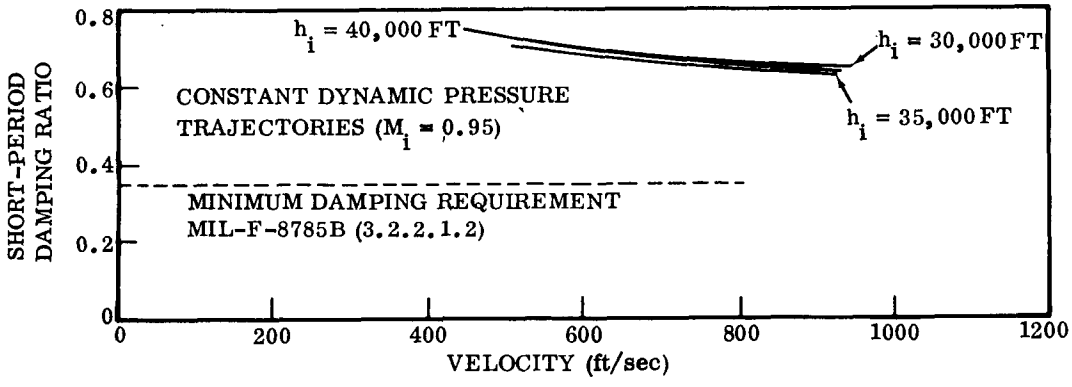

Figure 5-30. Longitudinal Short-Period Damping Ratio — Wing Deployed (Augmented)

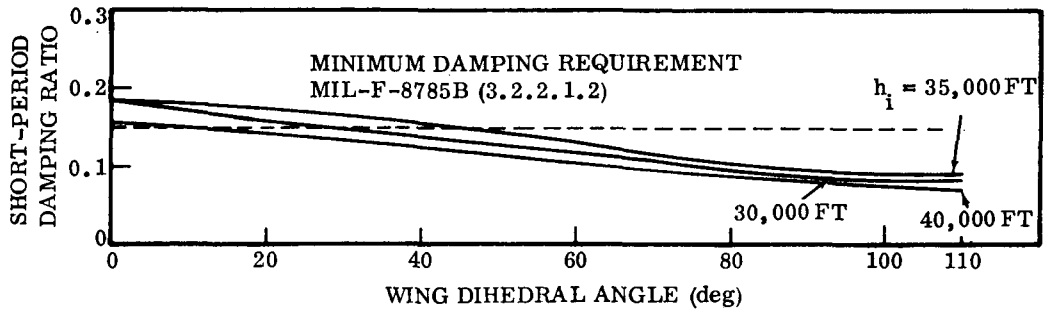

Figure 5-31. Short-Period Damping Ratio — Wing Deployment Sequence (Unaugmented)

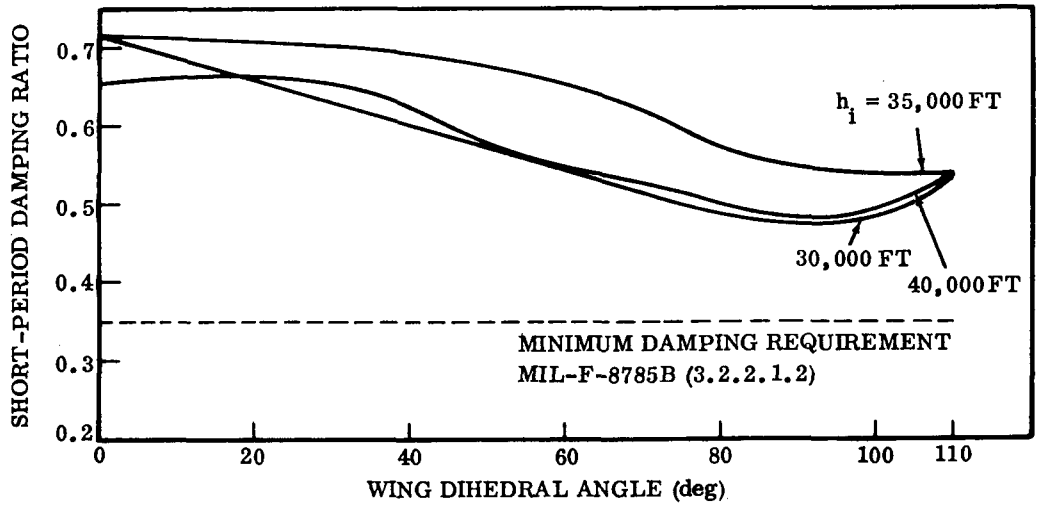

Figure 5-32. Short-Period Damping Ratio — Wing Deployment Sequence (Augmented)

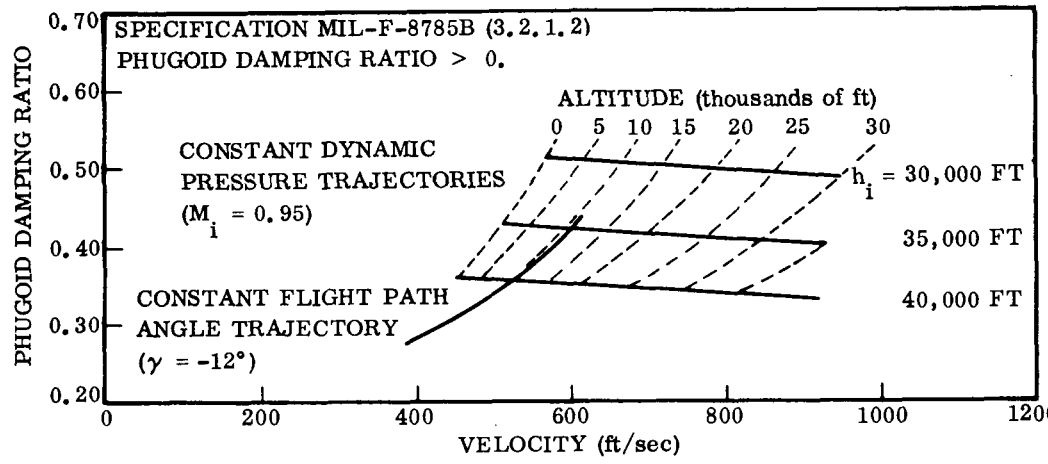

Figure 5-33. Phugoid Damping Ratio — Wings Deployed (Unaugmented)

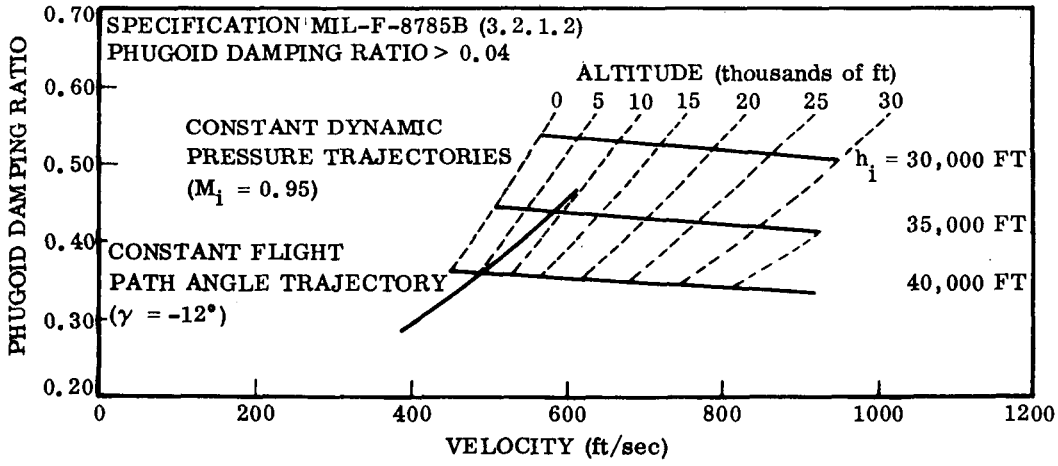

Figure 5-34. Phugoid Damping Ratio — Wings Deployed (Augmented)

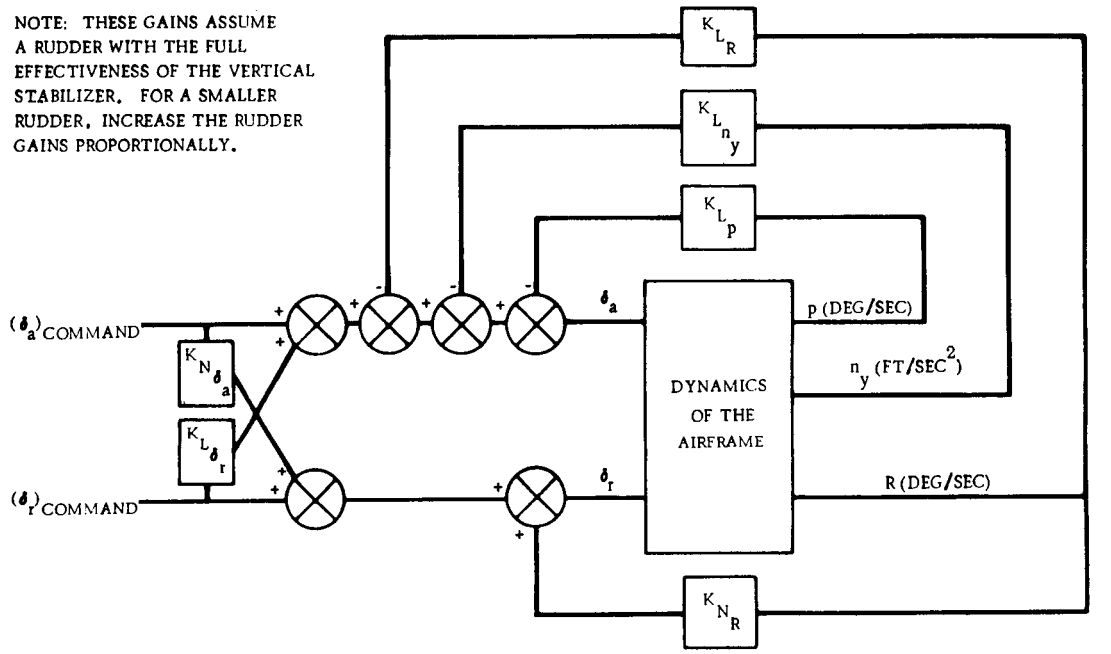

$K_{L_p} = 0.015 \frac{DEG}{DEG/SEC}$

$K_{L_{n_y}} = 0.17 \frac{DEG}{FT/SEC^2}$

$K_{L_R} = 0.05 \frac{DEG}{DEG/SEC}$

$K_{N_R} = 0.1 \frac{DEG}{DEG/SEC}$

$K_{N_{\delta_a}} = 0.1 \frac{DEG}{DEG}$

$K_{L_{\delta_r}} = 1 \frac{DEG}{DEG}$

Figure 5-35. Lateral Stability Augmentation System

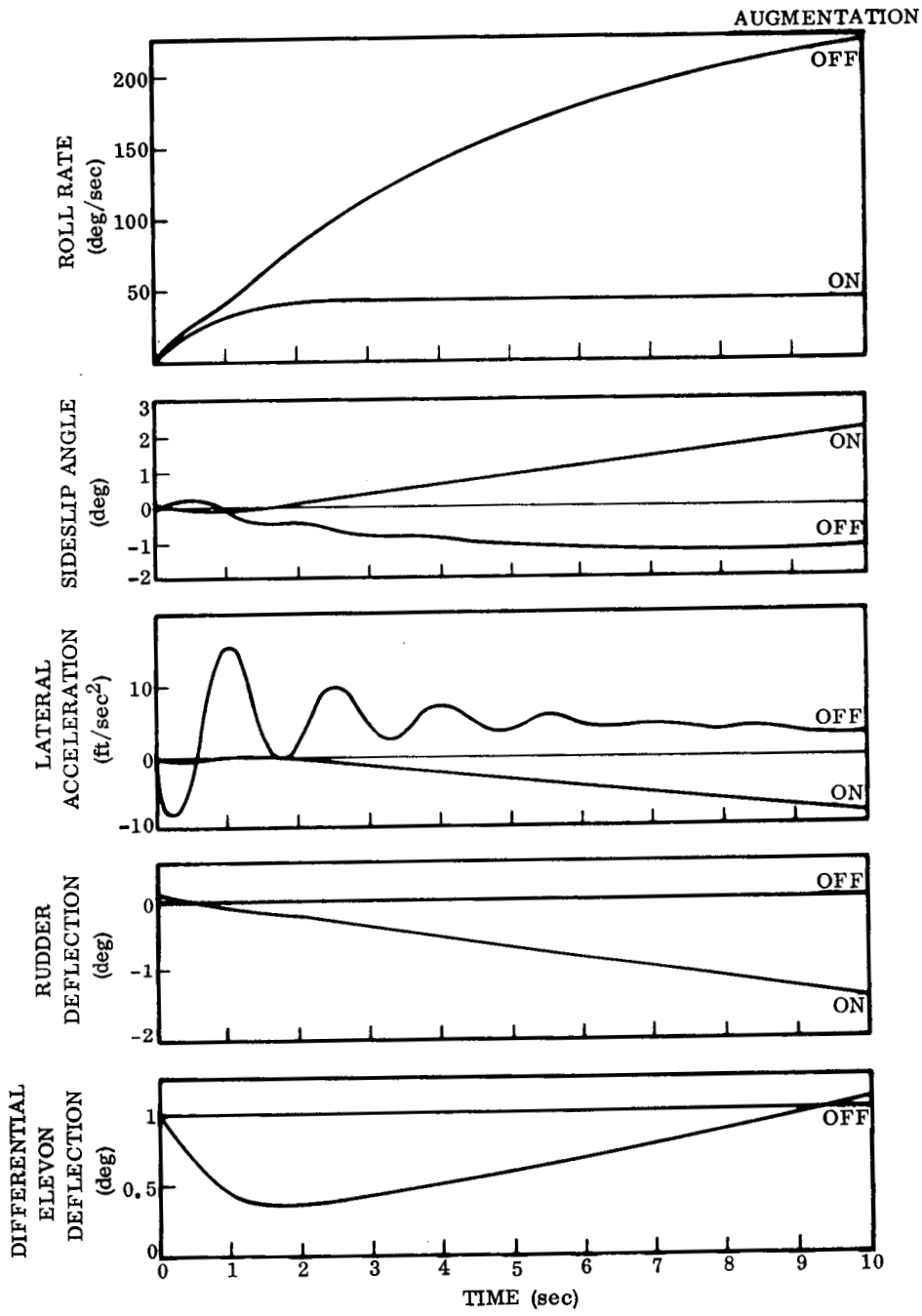

Figure 5-36. Roll Response at Mach 0.95 and 40,000 Feet

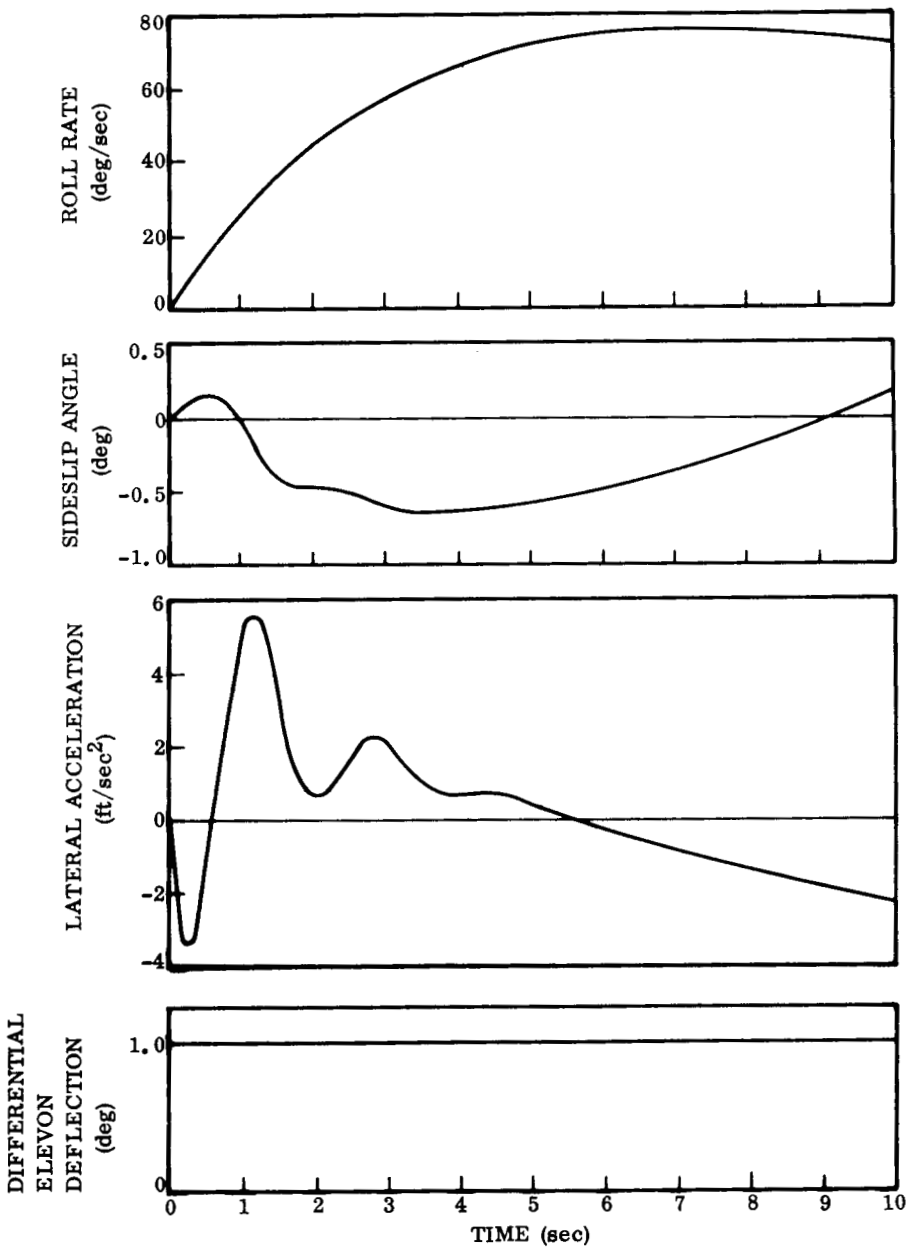

Figure 5-37. Roll Response at 200 Feet Altitude and 390 Ft/Sec (Unaugmented)

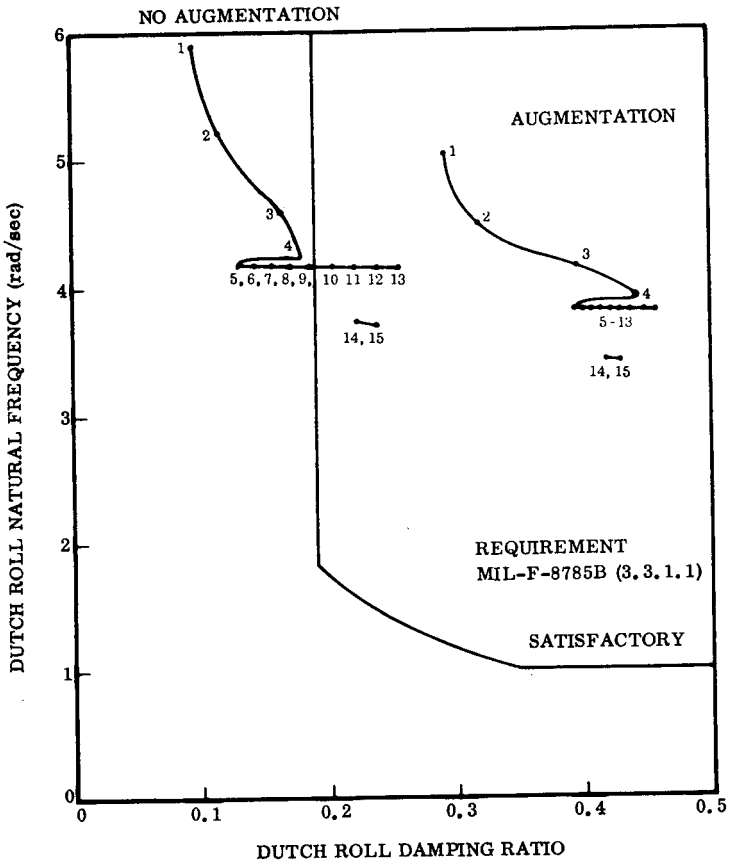

KEY

No.	Altitude (ft)	Velocity (ft/sec)	Dihedral (deg)
1	40,000	920 (M = 0.95)	110
2	40,000	920	90
3	40,000	920	60
4	40,000	920	30
5	40,000	920	0
6	35,000	816	0
7	30,000	742	0
8	25,000	677	0
9	20,000	619	0
10	15,000	569	0
11	10,000	525	0
12	5,000	485	0
13	0	450	0
14	5,000	421	0
15	200	389	0

Figure 5-38. Dutch Roll Characteristics

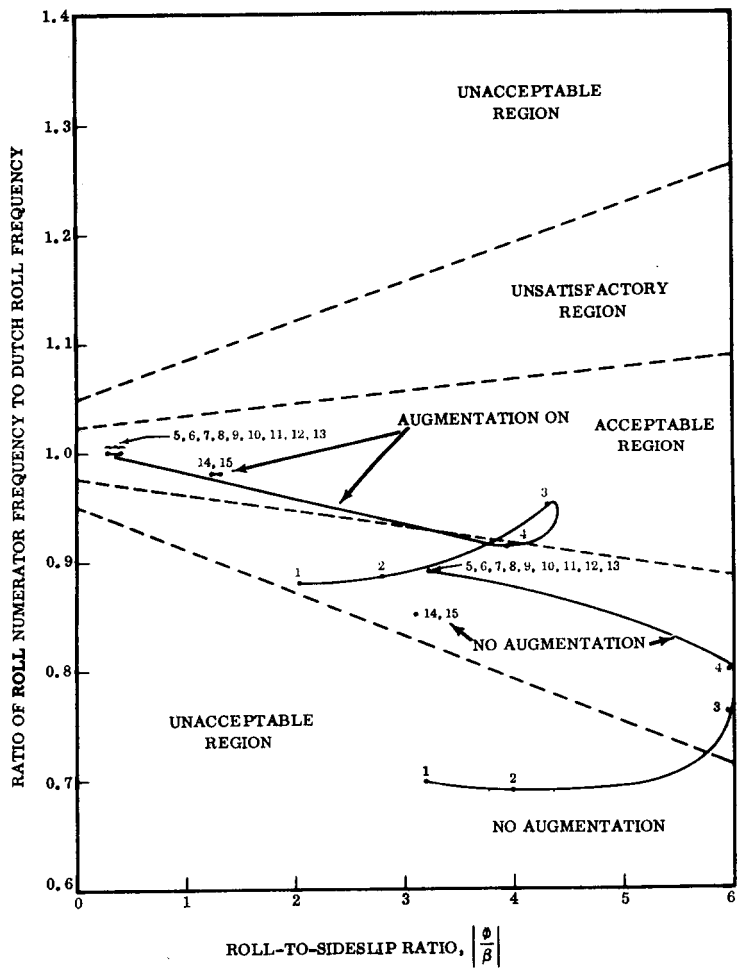

KEY

No.	Altitude (ft)	Velocity (ft/sec)	Dihedral (deg)
1	40,000	920 (M = 0.99)	110
2	40,000	920	90
3	40,000	920	60
4	40,000	920	30
5	40,000	920	0
6	35,000	816	0
7	30,000	742	0
8	25,000	677	0
9	20,000	619	0
10	15,000	525	0
11	10,000	525	0
12	5,000	485	0
13	0	450	0
14	5,000	421	0
15	200	389	0

Figure 5-39. Roll Oscillation Requirement

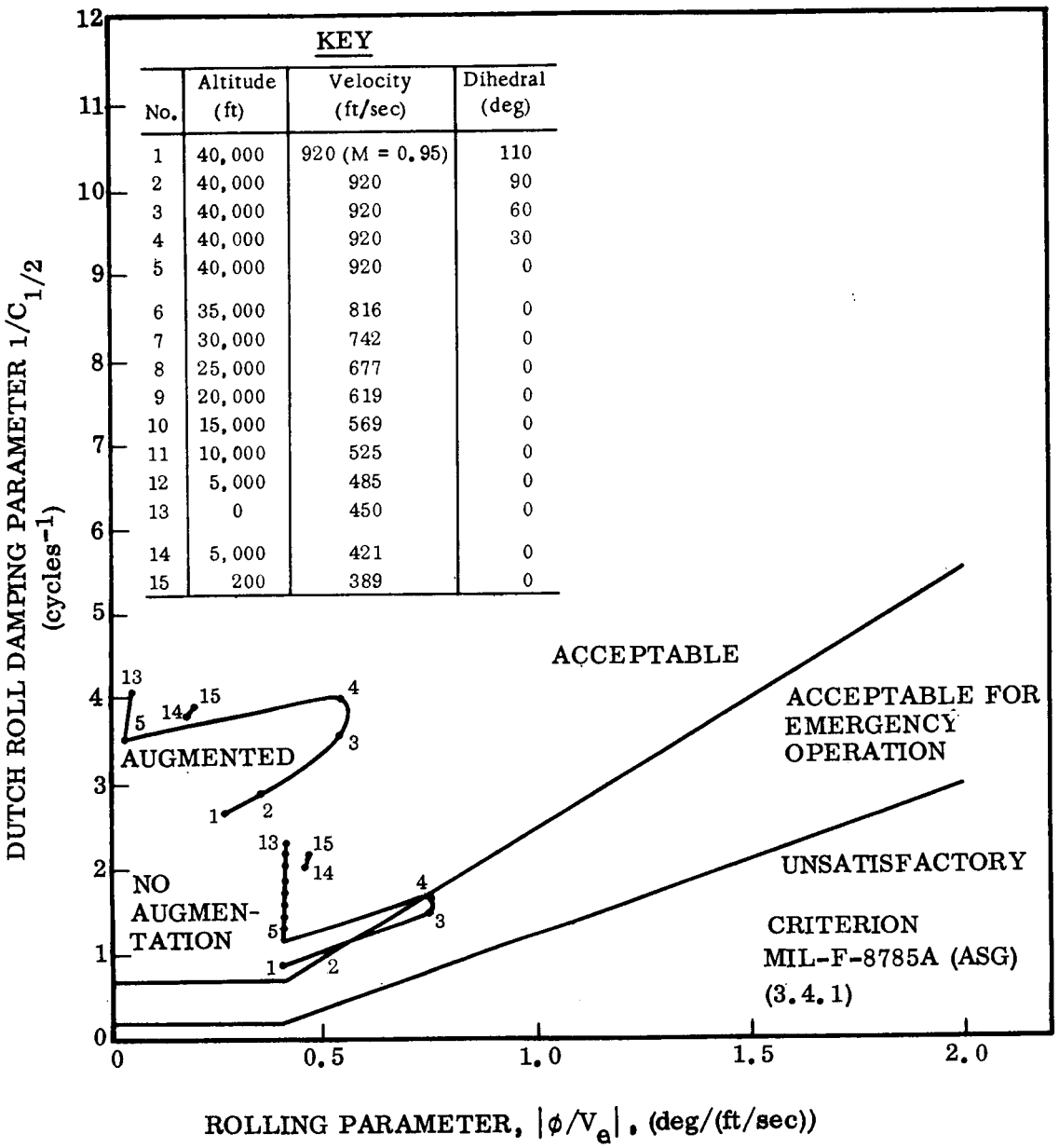

Figure 5-40. Dutch Roll Damping and Roll to Sideslip Velocity Parameters